Advances in Open Microfluidics from Fundamental Flow Dynamics to Environmental and Translational Science Applications

Jodie C. Tokihiro

A dissertation
submitted in partial fulfillment of the
requirements for the degree of

Doctor of Philosophy

University of Washington
2025

Reading Committee:
Ashleigh B. Theberge, Chair
Ayokunle O. Olanrewaju
Dan Fu

Program Authorized to Offer Degree:
Chemistry

University of Washington

Abstract

Advances in Open Microfluidics from Fundamental Flow Dynamics to Environmental and Translational Science Applications

Jodie C. Tokihiro

Chair of the Supervisory Committee:
Ashleigh B. Theberge
Department of Chemistry

This dissertation will demonstrate and discuss advances in open-channel microfluidics at the fundamental and translational levels. Chapter 1 outlines new fundamental open-microfluidic tools through via analytical models and comparisons with open channel fluid flow experiments. Chapter 2 will demonstrate enhanced capillary flow through the coupling of homothetic, bifurcating capillary trees and semi-circular paper pads at the extremities to maintain high fluid velocities throughout the channel over an extended period of time. Chapter 3 will discuss and demonstrate the need for a dynamic contact angle (DCA) at high fluid velocities through a survey of current theoretical approaches including multiple hydrodynamic models and the molecular kinetic theory with a comparison to in-lab flow experiments in U-shaped open microfluidic channels. Chapter 4 will present the implementation of trigger valves in open channel configurations allowing for the formation of lateral flow of multiple liquids in parallel for precise fluid addition. Chapter 5 will focus on the use of an open-channel droplet generator that can encapsulate human sperm samples for the use in cryopreservation steps in assisted reproductive technology (ART) workflows.

Table of Contents

List of Figures

Additional figures in appendices A-D

List of Figures (continued)

List of Tables

Additional tables in appendices A-D:

Acknowledgements

As I complete this chapter of my life, I have learned that completing a doctorate is not a solo journey and that I could write a separate thesis just for acknowledgements! Throughout my four years here at the University of Washington, I am so grateful to have been surrounded by supportive family members, wonderful friends, and extremely talented lab mates.

To the Theberge/BCME lab, thank you for making my grad school experience so fulfilling and amazing! I could not ask for a better research group to do my PhD in. I enjoyed getting to know everyone during experiments or trainings on the Datron and Kruss. It is an honor to be able to grow as a researcher and student alongside everyone. Thank you all for listening to my presentations, providing feedback on manuscripts, sharing your exciting scientific findings, and chatting about anything and everything. I want to also thank all of my co-authors in our lab and our collaborators. I could not have done it without you all!

To Ashleigh, thank you so much for being a great mentor and PI that leads with integrity, honesty, and transparency. You have taught me so much during these four years in your lab that has allowed me to grow as a researcher, mentor, collaborator, and peer. From learning how to manage projects to honing my writing as well as learning how to overcome various challenges inside and outside of the lab, I gained so many important skills that will help me in my career and beyond. I am most appreciative of your unwavering support, patience, encouragement, and understanding of me as I navigated so many new experiences in graduate school. I am glad to have been able to be a small piece of the whole BCME lab puzzle and I cannot wait to see what the future holds for you and the group.

To Jean, I am extremely honored to have been able to work with you these past four years. Thank you for teaching me about fundamental open microfluidics as well as inspiring me to work harder and keep pushing the boundaries of what we can do with open-channel microfluidics. I enjoyed brainstorming new project ideas, discussing science, and sharing pieces of Hawaii with you. Thank you again.

To Tristan, being one of your first mentees as an assistant professor has truly been a wonderful experience. Thank you for teaching me to follow my curiosity, have fun with experiments by trying new things on the fly, and find joy in all of the small things.

To my Seattle friends, thank you for making the big city of Seattle feel like a second home for this girl from Hawaii. Lauren, Filip, words cannot express how appreciative and happy I am to be able to call you both my true friends. Thank you for being some of my biggest supporters, keeping me sane and grounded, helping me talk out tough feelings, and teaching me to be my authentic self. The fourth-floor office holds a special place in my heart since it is where we have shared everything from laughs, snacks, and tears. You both have made my time in grad school so memorable and I do not know where I would be without you both there at my side through it all. I am so proud of how far we have come and the people we have become. I will cherish all of the memories we have made together and will make in the future. To Jamison, Amanda, and the rest of the fourth floor office, thank you for always being great friends and being down for a random coffee walk. To Wan-chen, Ingrid, Denise, Ariel, thank you all for being amazing friends, sharing your passion for science, and letting me bounce random (and sometimes crazy) ideas with. To my graduate and undergraduate mentees, TJ, Yunos, Albert, and David, thank you for always being willing to help on projects—no matter the size of the task— for being enthusiastic about science, and for your patience with me as a mentor. You all have made mentoring a breeze!

To my family and friends in Hilo, thank you for being great sources of support for me throughout these years. To my mom and dad, thank you for helping me get to where I am now and for teaching me all the skills and traits I need to be able to achieve my goals. Thank you for letting me chase my dreams in Seattle and for bringing back home whenever I needed a break. To my sisters, Jenn and Jayme, thank you both for always being one call away whenever things got rough and I needed someone to talk to. I am so grateful to have sisters like you both to laugh or vent with. To Joshua, thank you for always being my source of strength. You have taught me to see the bigger picture, to be honest with myself, and to always do what makes me happy. To my grandparents, Grandma Betty and Grandpa Hamamoto, thank you for always standing next to me in spirit. I did it!

Dedication

To my late Grandpa Hamamoto, who believed in Dr. Jodie.

Chapter 1 | Introduction

This dissertation will focus on new open microfluidic methods for device design and fluid modeling including the couple of capillary trees with paper pumps, a correction for dynamic contact angle integration, and the implementation of trigger valves in open microfluidic channels. A focus on the application of open channel droplet generation for purified sperm cryopreservation will also be presented. Portions of this chapter were excerpted or paraphrased from Chapters 2-4 of this dissertation.

1.1 Fundamentals of open-channel microfluidics

Microfluidics is defined as the manipulation, flow, processing, and analysis of fluids in channels characterized by a cross-section with at least one dimension on the millimeter scale or smaller. The field has become increasingly popular and interdisciplinary in the past several decades for its many benefits including: precise fluid control, high throughput, reduced sample requirements, wide variety of fabrication materials, and multiplexing abilities, making this an attractive technique for laboratories across resource levels.[1–5] As a result, microfluidics expanded rapidly throughout the past several decades resulting in several sub-fields including: open-channel (open capillary) microfluidics, digital microfluidics, and droplet-based microfluidics. In this dissertation, I will discuss open-channel microfluidics in the context of fundamental principles and its applications in chemistry, urology, and translational research.

Open-channel microfluidics is a subset of microfluidics that is characterized by at least one free boundary within the microfluidic channel, which is achieved through the removal of at least one channel surface such as the channel floor, ceiling, or wall.[6,7] Some examples of open channel cross-section shapes include: U-shaped channels, V-grooves, threads, or suspended rails. The growing popularity of open microfluidics is linked to several advantages including: accessibility, low cost, easy fabrication, and easy surface treatment.[8–10] Contrary to traditional, closed channel microfluidics, the free surface of an open channel enables users to interact with and manipulate the fluids within the channel.[11] Further, the operation of an open channel only requires normal laboratory pipettes, the device, and desired fluid—eliminating the need for complex, expensive, and sometimes bulky pumps and actuators. Another additional benefit of open microfluidics is the wide availability of fabrication techniques. Innovations in technology allow for tighter tolerances, finer machining control, higher resolution, and a broader range of usable materials. These fabrication methods include: 3D printing[12], computer numerical control (CNC) milling[13–15], soft lithography[16], or injection molding[17]. These innovations have made open microfluidics a popular platform for diverse applications such as organ-on-a-chip models, protein and metabolite detection assays, space science, and cancer research.[8,18–23]

In open channel capillary flows, fluid flow is governed by spontaneous capillary flow (SCF) (Equation 1). Berthier et al. developed the condition for which SCF will occur in open channels which only depends on the channel geometry and contact angle.[6,7,24]

$$\frac{P_f}{P_w} < \cos(\theta) \tag{1}$$

Upon fulfillment of the SCF equation, SCF will occur when the ratio of the free surface(s) (denoted as P_f) to wetted dimension(s) (denoted as P_w) of the capillary channel cross-sections (wetted referring to the liquid-solid interfaces) is less than the cosine of the contact angle (denoted by the Greek letter, θ) (**Figure 1.1**). A critical physical parameter in SCF and referenced throughout this dissertation is contact angle. The contact angle is the tangential angle of the base of a liquid drop with a solid surface and is governed by the equilibrium of the solid-vapor, solid-liquid, and liquid-vapor interfacial tensions. In the case of water on a particular surface or substrate, hydrophilicity and hydrophobicity can be determined through the contact angle. Generally, surfaces with a high affinity for water (thus, hydrophilic) will have a low contact angle (< 90°) with a droplet of water. Conversely, surfaces with a low affinity for water will have a high contact angle (> 90°). Note: this definition only concerns the static or sessile contact angle. Chapter 2 of this dissertation will discuss the occurrence of a dynamic contact angle.

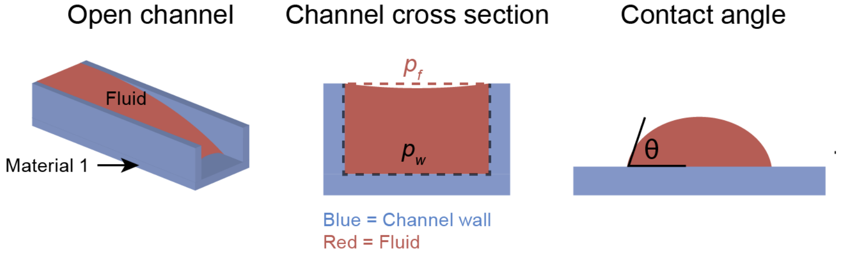

Figure 1.1. Critical parameters of the spontaneous capillary flow condition. Reproduced from Lee *et al.*[25]

1.2 Capillary flows in open-channel microfluidics

Throughout this thesis, we present a brief overview of capillary microfluidics with a special focus on pumping, circuitry, and dynamic contact angles in capillary systems. Capillary microfluidics has been an attractive option for a wide variety of applications as fluid flow solely relies on fluid properties and channel geometry and architecture to operate.

1.2.1 Capillary pumping

Movement of fluids through microfluidic channels are characterized by the type of force that is applied to pushes fluids through the channel. In general, there are two major categories of pumping types: active (mechanical) and passive (non-mechanical). Active pumping systems provide precise and continuous control of fluid through a channel, which requires a mechanical system to operate along with additional equipment such as tubing, syringe needles, or complex electronic systems. A classic example of an active pump is a syringe pump, which is utilizes a motor system to push a syringe plunger and dispense an accurate amount of fluid to a microfluidic channel. However, systems like a syringe pump or other mechanical-based pump (e.g., solenoid valves, micropumps) can be bulky or complex to operate. As a result, passive-driven pumping systems have been a popular alternative.

Many passive designs have been developed for capillary-driven flows in closed channels[26–29]; however, few have been proposed in the case of open channels. The electrowetting-based pumping device proposed by Satoh *et al.* is one of the first pumping designs in open geometries, but requires the addition of electric actuation.[30] The most current open-pumping systems rely on evaporation. Evaporation from a rectangular open channel has been documented by Kolliopoulos *et* al.[31] and Lynn *et al*.[32] and pumping has been set from a reservoir or fibrous pads by Zimmermann *et al*.[33] However, these methodologies are restricted to low boiling point liquids and entail long experiment durations. The search for efficient open channel pumping based solely on geometrical features is currently progressing. In Chapter 2, we will present a method that utilizes channel architecture and paper pads to extend capillary pumping in open channels.

1.2.2 Dynamic contact angle

Traditionally, fluid flow in capillary channels is modeled through the utilization of a static (constant) contact angle. The major theoretical model for predicting fluid flow in microfluidic channels is the Lucas-Washburn-Rideal (LWR) law, where fluid velocity (and thus, flow rate) decreases with the inverse of the square root of time.[34–36] Berthier et al. adapted this model for open systems, utilizing the generalized Cassie angle for the contact angle and an average friction length in place of the tube radius.[6,37] However, capillary flows at high velocities in the early stages of flow deviated from the predicted LWR law and relaxed to the expected static contact angle indicating presence of a dynamic contact angle. In closed channels, there are two general categories of dynamic contact angle models: a hydrodynamic (HD) model and a molecular kinetic theory model (MKT). The hydrodynamic (HD) approach corresponds to the case of viscous dissipation at the mesoscopic scale resulting in so-called viscous bending near the wall.[38–41] In the HD approach, the increase in the contact angle outside of the microscopic region (L_{mi}) is linked to the cubic root of the capillary number.[38] On the other hand, adsorption-desorption dynamics of liquid molecules on a solid surface near the TPCL (triple phase contact line) is the basis for the molecular kinetic theory (MKT). This approach was first proposed by Blake and Haynes[42] using

Eyring's activated-rate theory of stress-modified activated rate processes[43]. In Chapter 3 of this dissertation, the MKT model will be modified for open channels and we show comparison of this model with experimental results in open microfluidic channels.

1.2.3 Capillary circuitry

Capillary microfluidics enables the movement of fluids through small grooves with no peripheral equipment required—offering simplicity in device design and operation—but precise and autonomous fluid addition remains a challenge in open systems. Commonly, valves have been utilized to achieve this. Trigger valves (TGVs) are one of the main geometric features/control elements that make autonomous capillary-driven fluid addition possible.[44,45] TGVs are modified passive stop valves that release a confined liquid upon the capillary-driven flow of another or a similar liquid in an orthogonal channel to the stop valve. Stability of the TGVs lies in the offset of the valve and orthogonal channel floors, creating the so-called two-layer or "stair-step" TGVs, which help to retain fluid in the TGV channel.[46–48] In capillary-driven devices, the flow is regulated by surface energies and geometric features. Passive valves, which include TGVs, based on geometrical pinning are a common method for fine control of flow and on-chip programming. Geometrically, pinning occurs when capillary pressure is lost due to a sudden change in the channel architecture (such as an enlargement). Pinning of the fluid at the TGV "gate" is important to ensure that the fluid stops flowing until the depinning by a perpendicular flow by a miscible fluid. Retention of the liquid in the side channel until the main flow reaches the TGV relies on the liquid being pinned at the gate (or aperture), which refers to the edges of the side channel that intersects with the main channel. Pinning of a liquid on edges depends on the edge angle and on the liquid-solid contact angle.[49–52] If the constraints on the liquid (e.g., pressure) exceed the pinning angle threshold, pinning does not occur. Otherwise, pinning is stable, allowing us to leverage this phenomenon to create TGVs in open configurations.

1.3 Application of open-channel microfluidics for infertility and vitrification studies

1.3.1 Infertility

Infertility is defined by the inability to conceive a child within 12 months for female partners under the age of 35. This timeframe is shortened to 6 months for female partners above the age of 35 due to decreased egg quality with age.[53] The occurrence of infertility is widespread with approximately 1 in 6 couples affected worldwide with a male factor being identified in approximately 50% of these couples.[54–57] For those looking to conceive a child, assisted reproductive technologies (ART) are required, which include *in-vitro* fertilization (IVF), intracytoplasmic sperm injection (ICSI), and intrauterine injection (IUI). In these procedures, motile sperm is required for fertilization of oocytes and subsequently, successful conception. A critical step in fertility procedures is the cryopreservation (slow freezing) of sperm, which is collected and stored until required for ART. However, conventional cryopreservation processes currently used in laboratories result in a loss of approximately 30-50% of motile sperm after normal freeze-thaw processes.[58,59] This decrease is caused by several stress factors including temperature, oxidative, and osmotic stress. In turn, these stressors cause changes and damage to the sperm at the cellular and molecular level.[60,61] Thus, creating a need for improved freezing processes that enable higher recovery of motile sperm after normal freezing and thawing procedures.

1.3.2 Vitrification

Vitrification is the ultra-rapid freezing of hydrated, live cells through exposure of small volumes of sample to liquid nitrogen.[62] This form of cryopreservation is the gold standard method for storage of human oocytes in fertility laboratories, but can also be used for human spermatozoa. At a temperature of -196°C, vitrification quickly freezes aqueous samples in the absence of ice crystals, creating a glass-like state, and preserves sperm structure and function—a benefit that is conveyed through ultra-rapid freezing rates from 100°C to more than 10,000°C per minute provided by liquid nitrogen.[63–69] To achieve these high cooling rates, small volumes of sample are required. In standard vitrification workflows, sperm samples are portioned into sub-microliter to microliter volumes using a pipette, which can be time-consuming and challenging to achieve. Special vitrification devices have been published including the Cryoloop, Cryopiece, Cryotop, and a microstraw,[70–73] but may require specialized experience to operate that often requires visits to highly trained laboratories which are not readily accessible to patients in low-resource or rural regions. Therefore, there is a need for generating small volumes autonomously with minimal expertise required. Chapter 5 presents a novel method for partitioning sperm samples passively into submicroliter to microliter-sized droplets for vitrification using an open droplet-based microfluidic device.

1.4 Summary

The work presented in this dissertation advances each of the areas covered in this section. Chapter 2 demonstrates coupling of open capillary homothetic trees with semicircular paper pads to extend capillary flow. Chapter 3 compares various dynamic contact angle models to in-lab open channel experimental data. Chapter 4 implements trigger valves into open channels for precise, autonomous fluid addition. Lastly, Chapter 5 presents a method for aliquoting microliter-sized droplets of human sperm using an open-channel droplet generator in preparation for vitrification. Future directions of this thesis will explore trigger valve fluid pumping and flow rates and the observed effects on fluid layering as demonstrated in microfluidic devices such as ours. In addition, the open-channel droplet generation method will be coupled to a vitrification step and rapid thawing processes for implementation in fertility laboratories across resource levels.

1.5 References

1. Whitesides, G. M. The Origins and the Future of Microfluidics. *Nature* **2006**, *442* (7101), 368–373. https://doi.org/10.1038/nature05058.

2. Beebe, D. J.; Mensing, G. A.; Walker, G. M. Physics and Applications of Microfluidics in Biology. *Annu. Rev. Biomed. Eng.* **2002**, *4* (Volume 4, 2002), 261–286. https://doi.org/10.1146/annurev.bioeng.4.112601.125916.
3. Sackmann, E. K.; Fulton, A. L.; Beebe, D. J. The Present and Future Role of Microfluidics in Biomedical Research. *Nature* **2014**, *507* (7491), 181–189. https://doi.org/10.1038/nature13118.
4. Araz, M. K.; Tentori, A. M.; Herr, A. E. Microfluidic Multiplexing in Bioanalyses. *J. Lab. Autom.* **2013**, *18* (5), 350–366. https://doi.org/10.1177/2211068213491408.
5. Yang, Y.; Chen, Y.; Tang, H.; Zong, N.; Jiang, X. Microfluidics for Biomedical Analysis. *Small Methods* **2020**, *4* (4), 1900451. https://doi.org/10.1002/smtd.201900451.
6. Berthier, J.; Brakke, K. A.; Berthier, E. *Open Microfluidics*; Scrivener Publishing ; Wiley: Beverly, Massachusetts : Hoboken, New Jersey, 2016.
7. Berthier, J.; Theberge, A. B.; Berthier, E. *Open-Channel Microfluidics: Fundamentals and Applications*; IOP concise physics; Morgan & Claypool Publishers: San Rafael, Calif, 2019.
8. Oliveira, N. M.; Vilabril, S.; Oliveira, M. B.; Reis, R. L.; Mano, J. F. Recent Advances on Open Fluidic Systems for Biomedical Applications: A Review. *Mater. Sci. Eng. C Mater. Biol. Appl.* **2019**, *97*, 851–863. https://doi.org/10.1016/j.msec.2018.12.040.
9. Delamarche, E.; Kaigala, G. V. *Open-Space Microfluidics: Concepts, Implementations, Applications*; Wiley-VCH: Weinheim, 2018.
10. Dudukovic, N. A.; Fong, E. J.; Gemeda, H. B.; DeOtte, J. R.; Cerón, M. R.; Moran, B. D.; Davis, J. T.; Baker, S. E.; Duoss, E. B. Cellular Fluidics. *Nature* **2021**, *595* (7865), 58–65. https://doi.org/10.1038/s41586-021-03603-2.
11. Zeng, Y.; Khor, J. W.; Neel, T. L. van; Tu, W. chen; Berthier, J.; Thongpang, S.; Berthier, E.; Theberge, A. B. Miniaturizing Chemistry and Biology Using Droplets in Open Systems. *Nat. Rev. Chem. 2023 76* **2023**, *7* (6), 439–455. https://doi.org/10.1038/s41570-023-00483-0.
12. Lee, U. N.; Day, J. H.; Haack, A. J.; Bretherton, R. C.; Lu, W.; DeForest, C. A.; Theberge, A. B.; Berthier, E. Layer-by-Layer Fabrication of 3D Hydrogel Structures Using Open Microfluidics. *Lab. Chip* **2020**, *20* (3), 525–536. https://doi.org/10.1039/c9lc00621d.
13. Tokihiro, J. C.; Robertson, I. H.; Gregucci, D.; Shin, A.; Michelini, E.; Nicholson, T. M.; Olanrewaju, A. O.; Theberge, A. B.; Berthier, J.; Berthier, E. The Dynamics of Capillary Flow in an Open-Channel System Featuring Trigger Valves. *Sci. Rep.* **2024**, *14* (1). https://doi.org/10.1038/s41598-024-82329-3.
14. Guckenberger, D. J.; De Groot, T. E.; Wan, A. M. D.; Beebe, D. J.; Young, E. W. K. Micromilling: A Method for Ultra-Rapid Prototyping of Plastic Microfluidic Devices. *Lab. Chip* **2015**, *15* (11), 2364–2378. https://doi.org/10.1039/c5lc00234f.
15. Yu, J.; Berthier, E.; Craig, A.; De Groot, T. E.; Sparks, S.; Ingram, P. N.; Jarrard, D. F.; Huang, W.; Beebe, D. J.; Theberge, A. B. Reconfigurable Open Microfluidics for Studying the Spatiotemporal Dynamics of Paracrine Signalling. *Nat. Biomed. Eng.* **2019**, *3* (10), 830–841. https://doi.org/10.1038/s41551-019-0421-4.
16. Casavant, B. P.; Berthier, E.; Theberge, A. B.; Berthier, J.; Montanez-Sauri, S. I.; Bischel, L. L.; Brakke, K.; Hedman, C. J.; Bushman, W.; Keller, N. P.; Beebe, D. J. Suspended Microfluidics. *Proc. Natl. Acad. Sci.* **2013**, *110* (25), 10111–10116. https://doi.org/10.1073/pnas.1302566110.
17. Day, J. H.; Nicholson, T. M.; Su, X.; Van Neel, T. L.; Clinton, I.; Kothandapani, A.; Lee, J.; Greenberg, M. H.; Amory, J. K.; Walsh, T. J.; Muller, C. H.; Franco, O. E.; Jefcoate, C. R.; Crawford, S. E.; Jorgensen, J. S.; Theberge, A. B. Injection Molded Open Microfluidic Well Plate Inserts for User-Friendly Coculture and Microscopy. *Lab. Chip* **2020**, *20* (1), 107–119. https://doi.org/10.1039/c9lc00706g.

18. Li, Q.; Niu, K.; Wang, D.; Xuan, L.; Wang, X. Low-Cost Rapid Prototyping and Assembly of an Open Microfluidic Device for a 3D Vascularized Organ-on-a-Chip. *Lab. Chip* **2022**, *22* (14), 2682–2694. https://doi.org/10.1039/d1lc00767j.
19. Berthier, E.; Dostie, A. M.; Lee, U. N.; Berthier, J.; Theberge, A. B. Open Microfluidic Capillary Systems. *Anal. Chem.* **2019**, *91* (14), 8739–8750. https://doi.org/10.1021/acs.analchem.9b01429.
20. Lee, B.; Kim, S.; Ko, J.; Lee, S.-R.; Kim, Y.; Park, S.; Kim, J.; Hyung, S.; Kim, H.-Y.; Jeon, N. L. 3D Micromesh-Based Hybrid Bioprinting: Multidimensional Liquid Patterning for 3D Microtissue Engineering. *NPG Asia Mater.* **2022**, *14* (1). https://doi.org/10.1038/s41427-022-00355-x.
21. Weislogel, M. M.; Graf, J. C.; Wollman, A. P.; Turner, C. C.; Cardin, K. J. T.; Torres, L. J.; Goodman, J. E.; Buchli, J. C. How Advances in Low-g Plumbing Enable Space Exploration. *Npj Microgravity* **2022**, *8* (1). https://doi.org/10.1038/s41526-022-00201-y.
22. Nijhuis, J.; Schmidt, S.; Tran, N. N.; Hessel, V. Microfluidics and Macrofluidics in Space: ISS-Proven Fluidic Transport and Handling Concepts. *Front. Space Technol.* **2022**, *2*. https://doi.org/10.3389/frspt.2021.779696.
23. Rane, A.; Tate, S.; Sumey, J. L.; Zhong, Q.; Zong, H.; Purow, B.; Caliari, S. R.; Swami, N. S. Open-Top Patterned Hydrogel-Laden 3D Glioma Cell Cultures for Creation of Dynamic Chemotactic Gradients to Direct Cell Migration. *ACS Biomater. Sci. Eng.* **2024**, *10* (5), 3470–3477. https://doi.org/10.1021/acsbiomaterials.4c00041.
24. Berthier, J.; Brakke, K. A.; Berthier, E. A General Condition for Spontaneous Capillary Flow in Uniform Cross-Section Microchannels. *Microfluid. Nanofluidics* **2014**, *16* (4), 779–785. https://doi.org/10.1007/s10404-013-1270-1.
25. Lee, U. N. Open Microfluidic Technologies for Fundamental and Applied Studies of Human Health and the Environment. Ph.D., University of Washington, United States -- Washington, 2022. https://www.proquest.com/docview/2696290359/abstract/BDA40D8707B94AD4PQ/1 (accessed 2025-08-14).
26. Juncker, D.; Schmid, H.; Drechsler, U.; Wolf, H.; Wolf, M.; Michel, B.; De Rooij, N.; Delamarche, E. Autonomous Microfluidic Capillary System. *Anal. Chem.* **2002**, *74* (24), 6139–6144. https://doi.org/10.1021/ac0261449.
27. Cesaro-Tadic, S.; Dernick, G.; Juncker, D.; Buurman, G.; Kropshofer, H.; Michel, B.; Fattinger, C.; Delamarche, E. High-Sensitivity Miniaturized Immunoassays for Tumor Necrosis Factor Alpha Using Microfluidic Systems. *Lab. Chip* **2004**, *4* (6), 563–569. https://doi.org/10.1039/b408964b.
28. Zimmermann, M.; Schmid, H.; Hunziker, P.; Delamarche, E. Capillary Pumps for Autonomous Capillary Systems. *Lab Chip* **2007**, *7* (1), 119–125. https://doi.org/10.1039/b609813d.
29. Vestad, T.; Marr, D. W. M.; Oakey, J. Flow Control for Capillary-Pumped Microfluidic Systems. *J. Micromechanics Microengineering* **2004**, *14* (11), 1503–1506. https://doi.org/10.1088/0960-1317/14/11/010.
30. Satoh, W.; Hosono, H.; Suzuki, H. On-Chip Microfluidic Transport and Mixing Using Electrowetting and Incorporation of Sensing Functions. *Anal. Chem.* **2005**, *77* (21), 6857–6863. https://doi.org/10.1021/ac050821s.
31. Kolliopoulos, P.; Jochem, K. S.; Francis, L. F.; Kumar, S. Capillary Flow of Evaporating Liquid Solutions in Open Rectangular Microchannels. *J. Fluid Mech.* **2022**, *938*. https://doi.org/10.1017/jfm.2022.140.
32. Lynn, N. S.; Dandy, D. S. Passive Microfluidic Pumping Using Coupled Capillary/Evaporation Effects. *Lab. Chip* **2009**, *9* (23), 3422. https://doi.org/10.1039/b912213c.

33. Zimmermann, M.; Bentley, S.; Schmid, H.; Hunziker, P.; Delamarche, E. Continuous Flow in Open Microfluidics Using Controlled Evaporation. *Lab. Chip* **2005**, *5* (12), 1355. https://doi.org/10.1039/b510044e.
34. Lucas, R. Ueber das Zeitgesetz des kapillaren Aufstiegs von Flüssigkeiten. *Kolloid-Z.* **1918**, *23* (1), 15–22. https://doi.org/10.1007/bf01461107.
35. Washburn, E. W. The Dynamics of Capillary Flow. *Phys. Rev.* **1921**, *17* (3), 273–283. https://doi.org/10.1103/physrev.17.273.
36. Rideal, E. K. On the Flow of Liquids under Capillary Pressure. *Lond. Edinb. Dublin Philos. Mag. J. Sci.* **1922**, *44* (264), 1152–1159. https://doi.org/10.1080/14786441008634082.
37. Berthier, J.; Gosselin, D.; Berthier, E. A Generalization of the Lucas–Washburn–Rideal Law to Composite Microchannels of Arbitrary Cross Section. *Microfluid. Nanofluidics* **2015**, *19* (3), 497–507. https://doi.org/10.1007/s10404-014-1519-3.
38. Cox, R. G. The Dynamics of the Spreading of Liquids on a Solid Surface. Part 1. Viscous Flow. *J. Fluid Mech.* **1986**, *168*, 169–194. https://doi.org/10.1017/s0022112086000332.
39. Voinov, O. V. Hydrodynamics of Wetting. *Fluid Dyn.* **1977**, *11* (5), 714–721. https://doi.org/10.1007/bf01012963.
40. Dussan V, E. B. On the Difference between a Bounding Surface and a Material Surface. *J. Fluid Mech.* **1976**, *75* (4), 609–623. https://doi.org/10.1017/s0022112076000414.
41. Ramé, E.; Garoff, S. Microscopic and Macroscopic Dynamic Interface Shapes and the Interpretation of Dynamic Contact Angles. *J. Colloid Interface Sci.* **1996**, *177* (1), 234–244. https://doi.org/10.1006/jcis.1996.0026.
42. Blake, T. D.; Haynes, J. M. Kinetics of Liquid/Liquid Displacement. *J. Colloid Interface Sci.* **1969**, *30* (3), 421–423. https://doi.org/10.1016/0021-9797(69)90411-1.
43. Eyring, H. The Activated Complex in Chemical Reactions. *J. Chem. Phys.* **1935**, *3* (2), 107–115. https://doi.org/10.1063/1.1749604.
44. Olanrewaju, A. O.; Ng, A.; DeCorwin-Martin, P.; Robillard, A.; Juncker, D. Microfluidic Capillaric Circuit for Rapid and Facile Bacteria Detection. *Anal. Chem.* **2017**, *89* (12), 6846–6853. https://doi.org/10.1021/acs.analchem.7b01315.
45. Safavieh, R.; Juncker, D. Capillarics: Pre-Programmed, Self-Powered Microfluidic Circuits Built from Capillary Elements. *Lab. Chip* **2013**, *13* (21), 4180. https://doi.org/10.1039/c3lc50691f.
46. Zimmermann, M.; Hunziker, P.; Delamarche, E. Valves for Autonomous Capillary Systems. *Microfluid. Nanofluidics* **2008**, *5* (3), 395–402. https://doi.org/10.1007/s10404-007-0256-2.
47. Zhang, L.; Jones, B.; Majeed, B.; Nishiyama, Y.; Okumura, Y.; Stakenborg, T. Study on Stair-Step Liquid Triggered Capillary Valve for Microfluidic Systems. *J. Micromechanics Microengineering* **2018**, *28* (6), 065005. https://doi.org/10.1088/1361-6439/aab40c.
48. Mohammed, M. I.; Abraham, E.; Desmulliez, M. P. Y. Rapid Laser Prototyping of Valves for Microfluidic Autonomous Systems. *J. Micromechanics Microengineering* **2013**, *23* (3), 035034. https://doi.org/10.1088/0960-1317/23/3/035034.
49. Buguin, A.; Talini, L.; Silberzan, P. Ratchet-like Topological Structures for the Control of Microdrops. *Appl. Phys. A* **2002**, *75* (2), 207–212. https://doi.org/10.1007/s003390201322.
50. Ondarçuhu, T. Total or Partial Pinning of a Droplet on a Surface with a Chemical Discontinuity. *J. Phys. II* **1995**, *5* (2), 227–241. https://doi.org/10.1051/jp2:1995125.
51. Bico, J.; Marzolin, C.; Quéré, D. Pearl Drops. *Europhys. Lett. EPL* **1999**, *47* (2), 220–226. https://doi.org/10.1209/epl/i1999-00548-y.
52. Berthier, J.; Brakke, K. A. *The Physics of Microdroplets*; John Wiley & Sons, Inc ; Scrivener Publishing LLC: Hoboken, New Jersey : Salem, Massachusetts, 2012.
53. McLaren, J. F. Infertility Evaluation. *Obstet. Gynecol. Clin. North Am.* **2012**, *39* (4), 453–463. https://doi.org/10.1016/j.ogc.2012.09.001.

54. Carson, S. A.; Kallen, A. N. Diagnosis and Management of Infertility: A Review. *JAMA* **2021**, *326* (1), 65–76. https://doi.org/10.1001/jama.2021.4788.
55. Agarwal, A.; Mulgund, A.; Hamada, A.; Chyatte, M. R. A Unique View on Male Infertility around the Globe. *Reprod. Biol. Endocrinol. RBE* **2015**, *13*, 37. https://doi.org/10.1186/s12958-015-0032-1.
56. Agarwal, A.; Baskaran, S.; Parekh, N.; Cho, C.-L.; Henkel, R.; Vij, S.; Arafa, M.; Selvam, M. K. P.; Shah, R. Male Infertility. *The Lancet* **2021**, *397* (10271), 319–333. https://doi.org/10.1016/S0140-6736(20)32667-2.
57. Dohle, G. R.; Colpi, G. M.; Hargreave, T. B.; Papp, G. K.; Jungwirth, A.; Weidner, W.; EAU Working Group on Male Infertility. EAU Guidelines on Male Infertility. *Eur. Urol.* **2005**, *48* (5), 703–711. https://doi.org/10.1016/j.eururo.2005.06.002.
58. Kramer, R. Y.; Garner, D. L.; Bruns, E. S.; Ericsson, S. A.; Prins, G. S. Comparison of Motility and Flow Cytometric Assessments of Seminal Quality in Fresh, 24-Hour Extended and Cryopreserved Human Spermatozoa. *J. Androl.* **1993**, *14* (5), 374–384.
59. Donnelly, E. T.; Steele, E. K.; McClure, N.; Lewis, S. E. Assessment of DNA Integrity and Morphology of Ejaculated Spermatozoa from Fertile and Infertile Men before and after Cryopreservation. *Hum. Reprod. Oxf. Engl.* **2001**, *16* (6), 1191–1199. https://doi.org/10.1093/humrep/16.6.1191.
60. Mazur, P. Freezing of Living Cells: Mechanisms and Implications. *Am. J. Physiol.-Cell Physiol.* **1984**, *247* (3), C125–C142. https://doi.org/10.1152/ajpcell.1984.247.3.C125.
61. James, P. S.; Wolfe, C. A.; Mackie, A.; Ladha, S.; Prentice, A.; Jones, R. Lipid Dynamics in the Plasma Membrane of Fresh and Cryopreserved Human Spermatozoa. *Hum. Reprod.* **1999**, *14* (7), 1827–1832. https://doi.org/10.1093/humrep/14.7.1827.
62. Tao, Y.; Sanger, E.; Saewu, A.; Leveille, M.-C. Human Sperm Vitrification: The State of the Art. *Reprod. Biol. Endocrinol.* **2020**, *18* (1), 17. https://doi.org/10.1186/s12958-020-00580-5.
63. Palasz, A. T.; Mapletoft, R. J. Cryopreservation of Mammalian Embryos and Oocytes: Recent Advances. *Biotechnol. Adv.* **1996**, *14* (2), 127–149. https://doi.org/10.1016/0734-9750(96)00005-5.
64. Martino, A.; Songsasen, N.; Leibo, S. P. Development into Blastocysts of Bovine Oocytes Cryopreserved by Ultra-Rapid Cooling. *Biol. Reprod.* **1996**, *54* (5), 1059–1069. https://doi.org/10.1095/biolreprod54.5.1059.
65. Vajta, G.; Holm, P.; Kuwayama, M.; Booth, P. J.; Jacobsen, H.; Greve, T.; Callesen, H. Open Pulled Straw (OPS) Vitrification: A New Way to Reduce Cryoinjuries of Bovine Ova and Embryos. *Mol. Reprod. Dev.* **1998**, *51* (1), 53–58. https://doi.org/10.1002/(SICI)1098-2795(199809)51:1%253C53::AID-MRD6%253E3.0.CO;2-V.
66. Lane, M.; Bavister, B. D.; Lyons, E. A.; Forest, K. T. Containerless Vitrification of Mammalian Oocytes and Embryos. *Nat. Biotechnol.* **1999**, *17* (12), 1234–1236. https://doi.org/10.1038/70795.
67. Lane, M.; Gardner, D. K. Vitrification of Mouse Oocytes Using a Nylon Loop. *Mol. Reprod. Dev.* **2001**, *58* (3), 342–347. https://doi.org/10.1002/1098-2795(200103)58:3%253C342::AID-MRD13%253E3.0.CO;2-X.
68. Dinnyés, A.; Dai, Y.; Jiang, S.; Yang, X. High Developmental Rates of Vitrified Bovine Oocytes Following Parthenogenetic Activation, In Vitro Fertilization, and Somatic Cell Nuclear Transfer1. *Biol. Reprod.* **2000**, *63* (2), 513–518. https://doi.org/10.1095/biolreprod63.2.513.
69. Kuwayama, M.; Kato, O. Successful Vitrification of Human Oocytes. *Fertil. Steril.* **2000**, *74* (3), S49. https://doi.org/10.1016/S0015-0282(00)00850-5.
70. Schuster, T. G.; Keller, L. M.; Dunn, R. L.; Ohl, D. A.; Smith, G. D. Ultra-Rapid Freezing of Very Low Numbers of Sperm Using Cryoloops. *Hum. Reprod. Oxf. Engl.* **2003**, *18* (4), 788–795. https://doi.org/10.1093/humrep/deg162.

71. Sun, J.; Chen, W.; Zhou, L.; Hu, J.; Li, Z.; Zhang, Z.; Wu, Y. Successful Delivery Derived from Cryopreserved Rare Human Spermatozoa with Novel Cryopiece. *Andrology* **2017**, *5* (4), 832–837. https://doi.org/10.1111/andr.12380.
72. Chen, Y.; Li, L.; Qian, Y.; Xu, C.; Zhu, Y.; Huang, H.; Jin, F.; Ye, Y. Small-Volume Vitrification for Human Spermatozoa in the Absence of Cryoprotectants by Using Cryotop. *Andrologia* **2015**, *47* (6), 694–699. https://doi.org/10.1111/and.12320.
73. Huang, C.; Gan, R.-X.; Zhang, H.; Zhou, W.-J.; Huang, Z.-H.; Jiang, S.-H.; Ji, X.-R.; Gong, F.; Fan, L.-Q.; Zhu, W.-B. Novel Micro-Straw for Freezing Small Quantities of Human Spermatozoa. *Fertil. Steril.* **2020**, *114* (2), 301–310. https://doi.org/10.1016/j.fertnstert.2020.03.032.

Chapter 2 | Enhanced capillary pumping using open-channel capillary trees with integrated paper pads

Reproduced in part from ***Tokihiro, J.C.;**** *Tu, W.C.;* Berthier, J.;* Lee, J. J.; Dostie, A.; Khor, J.W.; Eakman, M.; Theberge, A.B.;# Berthier, E.# Enhanced capillary pumping using open channel capillary trees with integrated paper pads. Physics of Fluids,* ***2023****, 35, 082120.*
**Equal contribution*
#Co-corresponding authors

Please refer to journal site for supplementary materials referenced in this chapter: doi.org/10.1063/5.0157801

JCT: Data curation (equal); Formal analysis (equal); Investigation (equal); Methodology (equal); Project administration (equal); Validation (equal); Visualization (equal); Writing – original draft (equal); Writing – review & editing (equal). WCT: Data curation (equal); Formal analysis (equal); Investigation (equal); Methodology (equal); Project administration (equal); Validation (equal); Visualization (equal); Writing – original draft (equal); Writing – review & editing (equal). JCB: Conceptualization (equal); Data curation (equal); Formal analysis (equal); Methodology (equal); Supervision (equal); Validation (equal); Writing – original draft (equal); Writing – review & editing (equal). JJL: Data curation (equal); Formal analysis (equal); Investigation (equal); Methodology (equal); Software (equal); Writing – original draft (equal). AMD: Data curation (equal); Investigation (equal); Writing – original draft (equal). JWK: Conceptualization (equal); Formal analysis (equal); Writing – review & editing (equal). ME: Investigation (equal); Writing – review & editing (equal). ABT: Conceptualization (equal); Formal analysis (equal); Funding acquisition (equal); Project administration (equal); Supervision (equal); Writing – review & editing (equal). EB: Conceptualization (equal); Formal analysis (equal); Funding acquisition (equal); Supervision (equal); Writing – review & editing (equal).

Abstract: The search for efficient capillary pumping has led to two main directions for investigation: first, assembly of capillary channels to provide high capillary pressures, and second, imbibition in absorbing fibers or paper pads. In the case of open microfluidics (i.e., channels where the top boundary of the fluid is in contact with air instead of a solid wall), the coupling between capillary channels and paper pads unites the two approaches and provides enhanced capillary pumping. In this work, we investigate the coupling of capillary trees—networks of channels mimicking the

branches of a tree—with paper pads placed at the extremities of the channels, mimicking the small capillary networks of leaves. It is shown that high velocities and flow rates (7 mm/s or 13.1 μL/s) for more than 30 seconds using 50% (v/v) isopropyl alcohol, which has a 3-fold increase in viscosity in comparison to water; 6.5 mm/s or 12.1 μL/s for more than 55 seconds with pentanol, which has an 3.75-fold increase in viscosity in comparison to water; >3.5 mm/s or 6.5 μL/s for more than 150 seconds with nonanol, which has an 11-fold increase in viscosity in comparison to water) can be reached in the root channel, enabling higher sustained flow rates than that of capillary trees alone.

2.1 Introduction

Simple and autonomous microfluidic systems can be designed by use of capillary forces. In such systems, bulky active pumps[1,2] are not needed. However, a major drawback in a capillarity-based system is the decrease of the flow velocity—and the flow rate—with time. According to the Lucas-Washburn-Rideal (LWR) law, the decrease of the velocity is proportional to the inverse of the square root of time.[3–5] To overcome this drawback, different capillary pump designs have been developed.

Many passive designs have been developed for capillary-driven flows in closed channels[6-9]; however, few have been proposed in the case of open channels. The electrowetting-based pumping device proposed by Satoh *et al.* is one of the first pumping designs in open geometries, but requires the addition of electric actuation.[10] The most current open-pumping systems rely on evaporation. Evaporation from a rectangular open channel has been documented by Kolliopoulos *et al.*[11] and Lynn *et al.*[12] and pumping has been set from a reservoir or fibrous pads by Zimmermann *et al.*[13] However, these methodologies are restricted to low boiling point liquids and entail long experiment durations. The search for efficient open channel pumping based solely on geometrical features is currently progressing. Srinivasan has proposed a geometrical diffuser for zero gravity pumping in space vanes[14] and Guo *et al.* have developed an interesting system combining capillarity in closed channels and additional pumping from paper pads has been documented.[15]

In this work, the pumping mechanism involves the use of networks of small open channels where the capillary pressure is high, or there are matrices of fibers (often paper pads) with a high wicking power. These capillary pumps are placed behind the “region of interest” where the biological or chemical processes are performed and can be used in multiple applications including separation methods or sample processing.

Capillary trees for capillary pumping in closed (confined) channels have been developed in the past.[16] Examples include triple tree line capillary pumps used for performing immunoassays,[17] microstructures for simple and advanced capillary pumping,[18] and multilayers of microfluidic paper to generate the capillary flow.[19, 20] On the other hand, it was shown that microporous and fibrous structures, such as paper pads or porous membranes, provide efficient pumping properties due to their high wicking power.[21-23]

In the capillary-driven microfluidics field, open systems are of special interest.[24–26] These systems remove at least one "wall" of the microfluidic channel (often the top wall), providing easy access to the flowing liquid in the channels. We have previously found that a capillary tree can be used to maintain a high value of velocity in the root channel—the channel of interest for a given application—in open microfluidic devices.[27]

In this work, we show that these open capillary tree channels can easily be connected to paper pads (mimicking the small capillary networks of leaves) to further extend capillary pumping in the root channel which is an innovation from our previous work[28]. Extending periods of high flow velocity is an important problem in open capillary microfluidics. Here, we have chosen to use an open channel instead of a closed capillary tree due to fabrication limitations such as difficulty in adjusting a cover plate over the trees with minimal to no leakage of the flowing solvent. Along with our previous work, this work expands the toolbox for open-channel microfluidics, which is implemented in a broad range of fields of studies such as diagnostics, biomedical science, pharmaceutical science, space science, and integrated analysis systems. The removal of the top wall of the channel enables direct access to the flowing fluid for the addition, removal, or manipulation of the channel contents. Thus, together with this work and prior work,[28] we demonstrate a method for sustaining periods of high fluid velocity through the coupling of paper pads (current work) and bifurcating capillary trees (prior work).

In itself, an "infinite" capillary tree with decreasing channels has been shown to be favorable for pumping, but practically, it is impossible to design and fabricate such a device. In addition, paper alone is limited by the high friction of the liquid in the microporous media. Hence, the additive structure constituted by the paper pads replaces the downscaling of the trees and enhances the global pumping effect, first coming from the capillary tree and then from the fibrous paper "leaves". The paper pads are placed in milled receptacles at the end of the branched channels. We used a geometric design of capillary trees where the root channel is successively divided in a cascade of daughter channels and the cross sections of the daughter channels are progressively decreased at a ratio of 0.85. With this design, a high flow rate in the root channel can be achieved and sustained with such designs using bifurcations and paper pads (**Figure 2.1**). The multiplication of the tree branches avoids the velocity decrease in the root channel predicted by the LWR law in the case of a constant cross-section channel. The flow rate decreases in the branches after each bifurcation, but the flow rate in the root channel is twice that of the first branches and four times that in the second branches, and so on. On the other hand, the multiplication of the pads in parallel palliates the friction effect in each pad on the flow rate in the root channel.

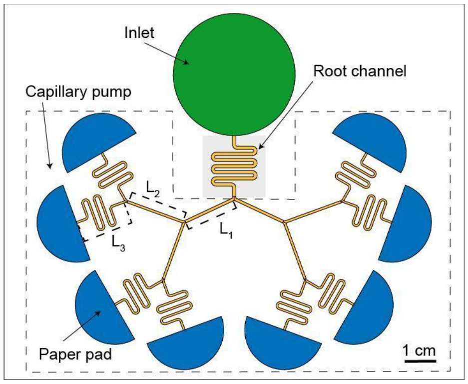

Figure 2.1. Diagram of an open channel microfluidic device utilizing a capillary tree channel and paper pads.

A closed form model for the flow dynamics is derived here, coupling the formulation of the capillary tree flow with the paper pads. In this manuscript, it will be shown that high capillary velocities are obtained even in the case of highly viscous fluids, pentanol, and nonanol. While there are publications where paper pads are used to drive flow[15,23], to the best of our knowledge, this is the first study to couple paper pads to bifurcating trees, specifically in open channel systems. We show here that by combining homothetic capillary tree channels with paper pads in an open microfluidic device, such designs maintain a high liquid velocity (7 mm/s or 13.1 µL/s) for more than 30 seconds using 50% (v/v) isopropyl alcohol, which has a 3-fold increase in viscosity in comparison to water; 6.5 mm/s or 12.1 µL/s for more than 55 seconds with pentanol, which has an 3.75-fold increase in viscosity in comparison to water; >3.5 mm/s or 6.5 µL/s for more than 150 seconds a fluid that has a viscosity that is 11 times higher than water in the root channel for more than one minute.

2.2 Results and Discussion

2.2.1 Theory

In the first phase, the flow advances in the capillary tree, dividing itself at each bifurcation. The device is designed so that the tree is symmetrical, thus all fluidic channels have the same length. This motion has already been analyzed in our prior work.[27] We describe here a theoretical approach for open capillary channel bifurcating trees coupled to paper pads. The nomenclature and associated definitions used in this section can be found in **Table 2.1**.

TABLE 2.1. Nomenclature for theoretical approach.

Symbol	Definition	[Unit]
Latin, lower case		
p	perimeter	[mm]
p_n	perimeter of root channel	[mm]
p_n	perimeter of branch n	[mm]
t	time	[s]
t_n	time at extremity of branch n	[s]
t_0	time at exit of the root channel	[s]
z	travel distance	[mm]
z_0	travel distance (root channel)	[mm]
z_n	travel distance in branch n	[mm]
z_p	travel distance in the paper pad	[mm]
Latin, upper case		
A_n	characteristic treelength (n branches)	[mm]
C	coefficient of the LWR law	[mm^2/s]
K	permeability (paper pad)	[mm^2]
L	length of a branch	[mm]
L_0	length of root channel	[mm]
P	pressure	[Pa]
P_j	pressure at node j	[Pa]
P_{cap}	capillary pressure	[Pa]
S	cross-sectional area	[mm^2]
S_0	cross-sectional area (root channel)	[mm^2]
S_{p0}	cross-sectional area (paper pad entrance)	[mm^2]
V	velocity	[mm/s]
V_0	velocity (root channel)	[mm/s]
V_n	velocity (branch n)	[mm/s]
Greek, lower case		
α	homothetic factor	[non-dimensional]
β	geometrical angle of the circular pad	[rd]
γ	liquid-air surface tension	[mN/m]
ϕ	porosity (paper pad)	[non-dimensional]
λ	friction length	[mm]
μ	liquid viscosity	[mPa.s]
τ	time (for paper pads)	[s]
θ	Young angle	[rd]
$\theta*$	generalized Cassie angle	[rd]
Greek, upper case		
∇	gradient operator	[1/mm]
Σ_n	characteristic number for the tree	[non-dimensional]

Let us recall that the marching distance in the open root channel (the channel before the beginning of the bifurcations) is given by

$$z_0 = \sqrt{\frac{2\,\lambda\,\gamma\,cos\theta_0^*}{\mu}}\,\sqrt{t} \tag{1}$$

where λ is the average wall friction length,[29] γ is the surface tension, μ is the viscosity, t is the time, θ^* is the generalized Cassie angle,[30] and index, 0, refers to the root channel, so that θ_0^* is the generalized Cassie angle in the root channel. Using the pressure at each node (bifurcation) plus the homothetic relation for the channel perimeters, and cross sections and the mass conservation equation, one finds the expression of z_n for the marching distance in the channels after the n^{th} bifurcations:

$$z_n = A_n\left[-1 + \sqrt{1 + \frac{\alpha^n C}{A_n^2}\,(t - t_{n-1})}\right] \tag{2}$$

where $C = \frac{2\,\lambda\,\gamma\,cos\theta^*}{\mu}$, α is the homothetic ratio, t_{n-1} is the time at which the liquid enters the nth channel, and A_n is a geometrical factor which depends on the channel lengths L_0 to L_{n-1} and α. The algebra leading to this expression is lengthy and fully developed in the **Appendix Section A1**. Note that (2) differs from the LWR expression where $z \sim t^{1/2}$.

Figure 2.2 shows the flow of fluid in a device that combines a capillary tree and paper pads. When the flow reaches the paper pads, the wicking of the pads is governed by Darcy's law.[31,32]

$$V_p = -\frac{K}{\mu\phi}\,\nabla P = \frac{K}{\mu\phi}\,\frac{P_{cap}-P_j}{z_p}, \tag{3}$$

where P_{cap} is the capillary pressure of the paper, P_j is the pressure at the channel-paper pad junction, K is the permeability of the pad, and φ is its porosity. The index, p, refers to the paper, and the triplet (P_{cap}, K, φ) characterizes the paper strip.[33,34] The capillary pressure of the paper pad must be larger—in absolute value—than the pressure, P_j, at the last nodes so that the liquid continues to flow in the pads (V_p >0). This condition is easily satisfied even if the capillary pressure in the tree increases after each bifurcation: $P_{cap,n} = p_n\,\gamma cos\theta_n^*/S_n = \alpha^{-n}p_0\,\gamma cos\theta_0^*/S_0 = \alpha^{-n}P_{cap,0}$. If we remark that $\alpha^{-n}P_{cap,0}{\sim}50$ Pa, and that the capillary pressure in most paper pads is of the order of 3000 Pa at least (**Table A3**), more than 25 bifurcations will still produce a capillary pressure inferior to that of the pad—considering α = 0.85. The derivation of the flow motion in the pads (coupled to the tree) is detailed in the **Appendix Section A2**. Note that three assumptions are used in the model. First, that the paper pads are homogeneous (i.e., there is no region of higher or lower porosity). Hence, saturation is neglected, and the sharp front assumption is used.[35–37] This observation is confirmed by experiments.[23,35]

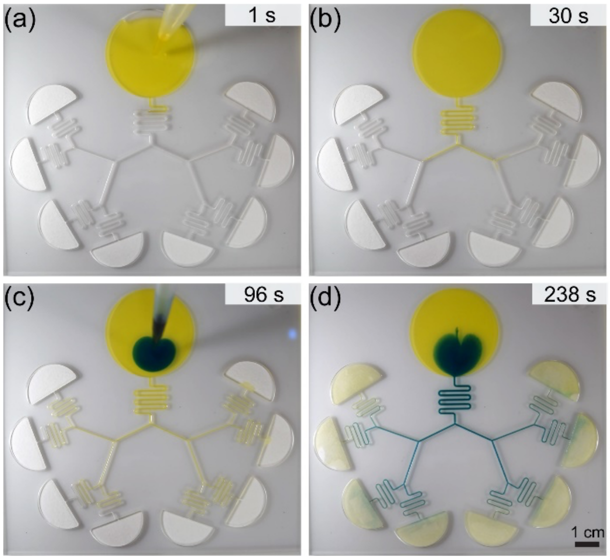

Figure 2.2. Still images of an open channel device filled with yellow and blue nonanol solutions. (**a**) Yellow liquid is pipetted in the inlet of the open channel. (**b**) Progression of the yellow liquid in the root channel and capillary tree. (**c**) Blue liquid is pipetted in the inlet after the yellow liquid reaches the paper pad. (**d**) Progression of blue liquid in the open channel. Scale bar is 1 cm.

Second, it is assumed that the dilatation of the paper fibers from the liquid is negligible, therefore, the porosity, *φ,* is constant everywhere in the pad. Third, the cellulose fibers do not absorb the wicking liquid, thus the mass conservation of the flowing liquid is independent of time.

Equation (3) can be solved using the expression of the pressure, P_j, found in the first phase (flow in the tree) and assuming a circular or flat contact line in the conical (angle β) or rectangular pads ($\beta = 0$). The travel distance in the paper is then

$$z_p = \frac{a_n}{\left(1+\frac{a_n}{\delta}\right)} \frac{S_{p,0}}{S_0} \left(-1 + \sqrt{1 + \left(\frac{S_0}{S_{p,0}}\right)^2 \frac{b\left(1+\frac{a_n}{\delta}\right)\tau}{\mathrm{a}_n^2}} \right) \tag{4}$$

where $a_n = 2^n \Sigma_n K \frac{p_0 L_0}{\lambda\ S_0}$, $\delta = \frac{S_0}{2\,\beta\,h_p}$, and $b = \frac{2K}{\mu\phi} P_{cap}$. Here, p_0 corresponds to the total perimeter of the cross section of the root channel, S_0 is the cross-section surface area, h_p is the thickness of the paper pad, β is the paper pad cone angle, τ is the time counted from the moment when the liquid reaches the pads, and $\Sigma_n = \left[1 + \frac{L_1}{2\alpha^4 L_0} + \cdots + \frac{L_n}{(2\,\alpha^4)^n L_0}\right]$. Note that if β is zero, then δ is infinite, resulting in $\frac{a_n}{\delta}$ to cancel out in equation (4). The two first parameters, a_n and δ, have the dimension of length, while the unit for b is mm^2/s and Σ_n is dimensionless. The ratio, $\frac{S_0}{S_{p,0}}$, is the ratio between the cross-sectional area of the root channel and that of the paper pad (at the junction with the tree). Using the mass conservation equation, the velocity in the root channel when the liquid wicks the paper is given by

$$V_{root} = 2^n V_p \phi \frac{S_p}{S_0} = \phi \left(\frac{S_{p,0}}{S_0}\ \frac{z_p}{\delta}\right) \frac{S_0}{S_{p,0}} \frac{b}{2a\ \Sigma_n \sqrt{1+\left(\frac{S_0}{S_{p,0}}\right)^2 \frac{b\left(1+\frac{a_n}{\delta}\right)\tau}{\mathrm{a}_n^2}}}\ . \tag{5}$$

where z_p is given by (4).

2.2.2 Comparison with experiments

The travel distance produced by equation (S13) (**Appendix Section A2**) has been checked against the experiments using colored solutions of 50% (v/v) isopropyl alcohol, pentanol, nonanol (**Figure 2.3**) flowing in the homothetic tree of ratio α = 0.85. A representative trial for each fluid is shown in **Figure 2.3**. Raw data for the travel distance for each fluid is presented in **Figure A2**. The travel distances in the tree, as measured by the progression of the fluid front, are well matched by the theory. The theory assumes a perfect flow with a circular fluid front in the semi-circular paper pad and perfect synchronization between the pads; however, in our experiments, the fluid front deviates from the theory due to a not-perfectly circular liquid front in the paper pad, imperfect synchronization between the flows in the different branches, and occasional leaking in the space below the pads. Nonetheless, this does not preclude the data. Note that a velocity jump is predicted by the model at the tree/pad junction due to the sudden change of capillary pressure. However, this velocity jump is not high due to the friction along the whole capillary tree. For this reason and because of the connection between channel and pads, this jump is hardly seen in the experiments.

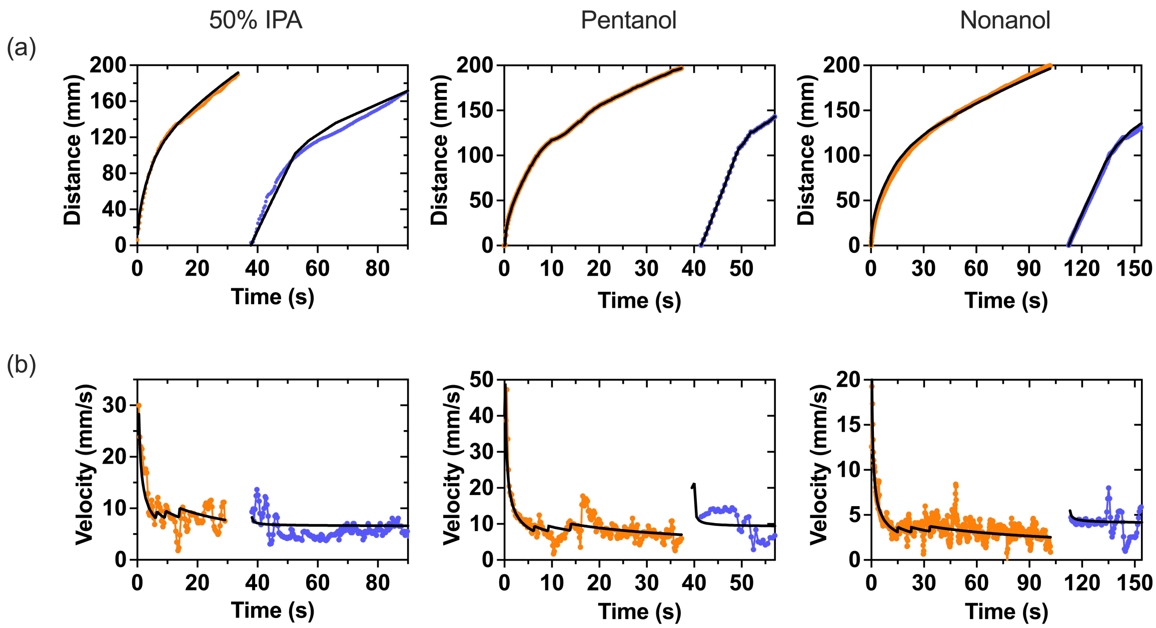

Figure 2.3. Travel distance and velocity over time for 50% (v/v) isopropyl alcohol (IPA) solution, pentanol, nonanol solutions in an open channel capillary tree with paper pads. (**a**) Experimentally determined travel distances in the bifurcating capillary tree vs. time for the first phase of the flow (orange dots) and the second phase of the flow (blue dots) after the flow has reached the pads and blue colored solution has been added to the inlet. Travel distance was determined by measuring the distance of the fluid front in the device in the recorded videos. The black lines are the theoretical results. (**b**) Velocities in the root channel vs. time when the tip of the flow is in the capillary tree (orange dots) and in the paper pads (blue dots). Velocities were determined using equation (5).

In the case of 50% (v/v) isopropyl alcohol, the coefficient, $\sqrt{\left(\frac{\gamma}{\mu}\right) 2\lambda\ cos\theta^*}$, was found to be approximately 40 mm/s$^{1/2}$ (Table A1). In the paper pads, a good fit was found for a capillary pressure of 3000 Pa. Root channel velocities on the order of 7 mm/s were obtained for 60 seconds (**Figure 2.3**) for 50% (v/v) isopropyl alcohol. The contact of the liquid with the pads occurs at 35 seconds for both 50% (v/v) isopropyl alcohol and pentanol, and 95 seconds for nonanol (**Figure 2.3**). Raw velocity data plots are presented in **Figure A3**.

For the case of pentanol, which is a fluid with an “intermediary” viscosity of 3.75 mPa.s. the pentanol also has a good fit for the travel distances in the capillary tree is obtained for the value $\sqrt{\left(\frac{\gamma}{\mu}\right) 2\lambda \cos\theta^*}$ = 40 mm/s$^{1/2}$. Root channel velocities on the order of 6.5 mm/s were obtained for at least 55 seconds (**Figure 2.3**).

The case of nonanol is of great interest due to its high viscosity of 0.011 Pa.s. A very good fit for the travel distances in the capillary tree is obtained for the value $\sqrt{\left(\frac{\gamma}{\mu}\right) 2\lambda \cos\theta^*}$ = 23.7 mm/s$^{1/2}$, and a capillary pressure P_{cap} = 5500 Pa in the paper pad. Root channel velocities on the order of 3.5 mm/s were obtained for 150 seconds (**Figure 2.3**).

The fluctuations that were observed in the velocity measurements (**Figure 2.3**) are due to the discretization, dz/dt. The velocity is the derivative of the travel distance and derivation amplifies the fluctuations. The only physical variation is at the junction between the channel and the paper due to abrupt capillary pressure change.

2.2.3 *Discussion*

Efficient capillary pumping has been the subject of many investigations. In this problem, three parameters must be considered: (1) the maximum velocity of the flow, (2) the maximum flow rate, and (3) the duration of the pumping. Prior research has focused on obtaining the highest possible velocities, but typically only for a short time and a moderate volumetric flow rate. For example, Reches et al. [38] has obtained interesting velocities of 2 cm/s for water in treated threads of wool, but along a length of 2 cm, corresponding to a duration time of 1 second. In Table II, a review of the literature for various methods of capillary pumping is summarized. The table indicates that it is difficult to obtain high velocities (larger than 1 mm/s) for a long duration (larger than 30 seconds) in capillary-based systems.

TABLE 2.2. Literature review of capillary pumping.

Reference Liquid	Velocity [mm/s]	Flow rate [μL/s]	Duration [s]	Channel Characteristics
Water[a]	n/a	0.13	15	Large array of PCB pillars spaced 50 to 300 μm
Water[b]	15	n/a	20	Multilayer paper pads (Whatman #1) 100 to 200 μm
Water[c]	n/a	0.07	n/a	Large array of pillars spaced 50 μm–- SI chips
Water[d]	0.3	n/a	1000	Paper pads width 1 to 3 cm (rectangular or circular sectors) Millipore nitrocellulose
Water[e]	10	n/a	10	Multilayer paper pads paper 175 μm, gap 36 μm (Whatman #1)
Glycerol solutions[f]	0.4	n/a	<10	3D printed channels Width 300 μm acrylonitrile-butadiene-styrene
Parylene/ Water[g]	0.4	n/a	< 10	Channels 10 μm parylene
Water (Wool, Threads)[h]	20	n/a	1	Fiber threads length 1 cm cotton, wool, polyester
<u>This study</u>				Milled capillary trees
Nonanol	>3.5	6.5	>150	Width 1 mm to 300 μm
50% IPA	7	13.1	>60	PMMA
Pentanol	6.5	12.1	>55	

[a] Reference 39.
[b] Reference 19.
[c] Reference 40.
[d] Reference 21.
[e] Reference 41.
[f] Reference 42.
[g] Reference 43.
[h] Reference 38.

In our study, it is assumed that the capillary tree is “symmetrical”, i.e., all branches at the same level of ramification are identical. The channels are relatively larger in size due to computer numerical control milling constrictions; however, this theory is applicable to smaller dimensions up to 300 μm in width when employing other types of fabrication methods. High velocities are obtained with our device where the dimensions are at the upper side of the microscale limits. If we remark that the root channel velocity is approximately proportional to the square root of the friction length and that the friction length decreases proportionally with the channel dimension, a homothetical reduction of the channel dimension of a factor, n, will result in the reduction of the velocity of a factor $\sqrt{n}$. For example, if the channel cross-section is decreased by 4 (200 µm width), the velocity will be reduced by a factor of 2. Still, high velocities are obtained with the device for microscale channels. The progression of the liquid is the same for each path and is obtained by using the extended LWR law that states that the dynamics of the flow results from the balance between the capillary force on the advancing meniscus and the wall friction along the path.[3–5,23,24] Intrinsically, capillary-driven flow velocities decrease as capillary length decreases. Here, our device enables longer capillary lengths in the root channel due to the multiplication of daughter branches while maintaining high flow velocities, allowing for applications in diagnostics and bioanalytical chemistry.[24] Note that the approach proposed here is also applicable to closed systems by using the friction length of the closed channels instead of open capillary channels.[24,25] In the microporous paper pads, the wicking liquid velocity is given by Darcy's law[31,32] and determined by three parameters: permeability, porosity, and capillary pressure.[33,34]

To validate the closed form model derived in this work, experiments were performed using nonanol, isopropyl alcohol, and pentanol solutions in open microfluidic channels. We chose these liquids because they wet native PMMA without surface treatment (θ = 13 - 47°, Table A1). Further, evaporation of these liquids is slow compared to the time scale of the capillary flow. Hence, evaporation is not taken into account for this study.[3,44–46] High capillary velocities are obtained even in the case of highly viscous nonanol, which has a viscosity eleven times that of water (**Table A1**). In the case of the less viscous isopropyl alcohol aqueous solution, velocities higher than 1 cm/s were obtained.

The device presented here is of interest for its ability to combine velocity, flow rate, and duration. This innovation builds on our previous work[28] to further enable extended periods of high velocity flow in open microfluidic channels, which is desired for capillary microfluidics research and device development for fields such as chemical, biomedical, biological, space science, and materials research. In the future, the device can be optimized to achieve higher velocity. A longer length of the last branch of the capillary tree can enable a higher velocity in the root channel. The choice of the paper matrix is of great importance, especially the two parameters K/φ (Leverett parameter) and capillary pressure (P_{cap}). Longer pads would allow longer duration of the high velocity flow. Additionally, the device can be micromilled using different materials, such as polystyrene, which enables wider application.[47] Devices can be oxygen plasma treated to allow flow of aqueous solutions (cell culture media, biological fluids, etc.).[26, 47]

2.3 Conclusion

In this work, the dynamics of the capillary flow circulating in a capillary tree with paper pads placed at the extremities of the capillary tree branches have been investigated. A model for the dynamics of the flow in the capillary tree has been coupled to a model for the flow in the paper pads. This coupling has been validated against experiments performed with milled open PMMA channels and paper pads. It is first shown that capillary trees with homothetically decreasing cross-sectional areas (in a ratio of 0.85) maintain the flow velocity in the root channel. Moreover, the presence of paper pads at the extremities of the branches prolongs the duration of the high flow rate pumping. The present analysis demonstrates the possibility of obtaining high velocities and flow rates (7 mm/s or 13.1 μL/s) for more than 30 seconds for 50% (v/v) isopropyl alcohol, 6.5 mm/s or 12.1 μL/s for more than 55 seconds with pentanol, and flow rates of >3.5 mm/s or 6.5 μL/s for more than 150 seconds for nonanol. These flow rates are nearly constant (save for periodic jumps due to experimental fluctuations) if conical-shaped paper pads are used as suggested in the literature.[48, 49] For volatile fluids, the employment of evaporation could extend the duration of these high flow rates. Further, we envision many areas of future application including using our method to push the limits of viscous fluid flow in open channels as we can enable the sustained passive flow of complex biological fluids such as saliva or blood. This device also has the potential to be applied to biological experiments such as *in vitro* cell culture or analytical methods involving biological fluids. Further, the method presented here can be adapted for diverse applications of open microfluidics including chemical synthesis, chemical analysis, thermics, material science, or space science, allowing for diverse applications at the frontiers of science.

2.4 Materials and Methods

2.4.1 Fabrication of capillary tree channels

The device consists of winding serpentine-shaped channels (the root channel), a large inlet in which the liquid is introduced using a pipette, three levels of branches, and semicircle paper pads at the extremity of the last set of channel branches (**Figure 2.1**). The dimensions of the channels are listed in **Table A2**; an engineering drawing is included in **Figure A1**; and the computer-aided design files are included in the electronic Supplementary Material. The widths and depths of the channels are homothetically reduced by a factor of 0.85 after each bifurcation. The turns in the winding channels do not affect the capillary flow in the absence of capillary filaments,[29] as the rounded bottom avoids the formation of filaments observed in channels of rectangular cross section.[50] The average wall friction length of the root channel is estimated to be $\lambda\sim$ 259 µm from our preceding work.[27,28] It was shown that the average friction length produces the value of the average wall friction, τ,by the formula, $\tau = \mu V/\lambda$[21], where μ is the liquid viscosity.

The device was designed using a computer aided design (CAD) software (Solidworks 2017, Waltham, MA) and the design files were converted to G-code using a computer aided manufacturing (CAM) software (Fusion 360). Channels were milled in poly(methyl methacrylate) (PMMA) sheets (3.175 mm thick, #8560K239; McMaster-Carr, Santa Fe Springs, CA). To create round bottom channels, endmills with a cutter diameter of 1/32” (TR-2-0312-BN) and 1/64” (TR-2-0150-BN) were used (Performance Micro Tool, Janesville, WI). The devices were fabricated via micromilling on a Datron Neo computer numerical control mill (Datron, Germany). The channel bottom is estimated to have a few microns of roughness which is one magnitude below the roughness values that were observed by Lade et al.[42] that would produce fluctuations in flow velocity.

2.4.2 Paper pads

Whatman #1 paper (Whatman Grade 1 Qualitative Filter Paper, #28450-160, VWR Scientific, San Francisco, CA) was cut into half circle shapes using a plotter cutter (Graphtec Corporation, Yokohama, Japan). A tight contact between the paper pads and the outlets of the last set of tree channels is essential to maintaining the capillary flow of the fluid. The main characteristics of the paper pads are listed in **Table A3**. The capillary pressure depends on the liquid that is used and the values are in alignment with the experimental results.

2.*4.*3 *Solvents*

The physical properties of the solvents are indicated in **Table A1**. To mitigate evaporation of the solvents, pentanol and nonanol, which are low volatile solvents, (boiling points are 139°C and 213°C for pentanol and nonanol, respectively), were used. Both pentanol and nonanol have been colored with either Solvent Yellow 7 or with Solvent Green 3 (Sigma-Aldrich) at concentrations of 0.50 mg/mL and 1.43 mg/mL, respectively. Aqueous isopropyl alcohol (VWR Scientific) was used at a concentration 50% (v/v) and colored with 0.60% yellow or 1.2% blue food coloring. (McCormick).

2.*4.4 Capillary trees with integrated paper pads flow experiments*

To obtain fluid travel distance and velocity data, 2 mL of the yellow-dyed fluid was pipetted into the reservoir of the device. Once the fluid front reached the end of level 1, a 200 μL refill of the yellow fluid was added. After the yellow fluid wetted the paper pad, 500 μL of the blue-dyed fluid was pipetted into the fluid reservoir with a 200 μL refill after the blue fluid front reached the end of level 1. Data was reported up to the point with when the paper pad was saturated at 90 s for 50% (v/v) isopropyl alcohol, 57 s for pentanol, 154 s for nonanol, for trials 1-3, respectively (**Figure 2.3**, **Figure A2**, and **A3**).

2*.4.5 Imaging and analysis*

Videos of the progression of the solvent flow in the device were recorded using a Nikon-D5300 ultra-high resolution single lens reflective (SLR) camera. The images of the videos were extracted automatically by the code. The location of the tip of the 50% (v/v) isopropyl alcohol flow was pinpointed using MATLAB software, while the travel distance of the pentanol and nonanol flows were measured manually using Fiji (ImageJ) software. For the manual analysis, the scale was set for an individual trial with the "Set Scale" tool. The fluid front was pinpointed with the "Segmented Line" tool and the "Measure" function was used to calculate the total distance traveled along the capillary tree. Each data was from every 10 frames (yellow) or 30 frames (blue).

2.5 References

1. Gervais, L.; Hitzbleck, M.; Delamarche, E. Capillary-driven multiparametric microfluidic chips for one-step immunoassays. *Biosens. Bioelectron*. **2011,** *27*, 64-70.
2. Safavieh, R.; Juncker, D. Capillarics: pre-programmed, self-powered microfluidic circuits built from capillary elements *Lab Chip* **2013**, *13*, 4180-4819.
3. Lucas, R. Ueber Das Zeitgesetz Des Kapillaren Aufstiegs von Flüssigkeiten. *Colloid Polym. Sci.* **1918**, *23* (1), 15–22.
4. Washburn, E. W. The Dynamics of Capillary Flow. *Phys. Rev.* **1921**, *17* (3), 273.
5. Rideal, E. K. On the Flow of Liquids under Capillary Pressure. *Philos. Mag. Ser. 6* **1922**, *44* (264), 1152–1159.
6. Juncker, D.; Schmid, H.; Drechsler, U.; Wolf, H.; Wolf, M.; Michel, B.; de Rooij, N.; Delamarche, E. Autonomous Microfluidic Capillary System. *Anal. Chem.* **2002**, *74*, 6139-6144.
7. Cesaro-Tadic, S., Dernick, G.; Juncker, D.; Buurman, G.; Kropshofer, H.; Michel, B.; Fattinger, C.; Delamarche, E. High-sensitivity miniaturized immunoassays for tumor necrosis factor α using microfluidic systems. *Lab Chip* **2004**, *4*, 563-569.
8. Zimmermann, M.; Schmid, H.; Hunziker, P.; Delamarche, E. Capillary pumps for autonomous capillary systems. *Lab Chip* **2007**, *7*, 119-125.
9. Vestad, T.; Marr, D. W. M.; Oakey, J. Flow control for capillary-pumped microfluidic systems, J. *Micromech. Microeng.* **2004**,*14*, 1503.
10. Satoh, W.; Hosono, H.; Suzuki, H. On-Chip Microfluidic Transport and Mixing Using Electrowetting and Incorporation of Sensing Functions. *Anal. Chem.* **2005**, 77(21), 6857–6863.
11. Kolliopoulos, P.; Jochem, K.; Francis, L.; Kumar, S. Capillary flow of evaporating liquid solutions in open rectangular microchannels. *J. Fluid Mech.*, **2022**, *938*, A22.

12. Lynn, N. S.; Dandy, D. S. Passive Microfluidic Pumping Using Coupled Capillary/Evaporation Effects. *Lab Chip* **2009**, *9* (23), 3422–3429.
13. Zimmermann, M.; Bentley, S; Schmid, H.; Hunziker, P.; Delamarche, E. Continuous flow in open microfluidics using controlled evaporation. *Lab Chip*, **2005**, *5*, 1355-1359.
14. Srinivasan, R. Estimating zero-g flow rates in open channels having capillary pumping vanes. *Int. J. Numer. Meth.* Fluids, **2003**, *41*, 389-4176.
15. Guo, W.; Hansson, J.; van der Wijngaart, W. Capillary pumping independent of the liquid surface energy and viscosity. *Microsyst. Nanoeng*. **2018**, *4*, 2.
16. Olanrewaju, A.; Beaugrand, M.; Yafia, M.; Juncker, D. Capillary Microfluidics in Microchannels: From Microfluidic Networks to Capillaric Circuits. *Lab Chip* **2018**, *18* (16), 2323–2347.
17. Pla-Roca, M.; Juncker, D. PDMS microfluidic capillary systems for patterning proteins on surfaces and performing miniaturized immunoassays. *Methods Mol. Biol.* **2011**, *671*, 177-194.
18. Delamarche, E.; Juncker, D.; Schmid, H. Microfluidics for Processing Surfaces and Miniaturizing Biological Assays. *Adv. Mater.* **2005**, *17*, 2911-2933.
19. Channon, R. B.; Nguyen, M. P.; Scorzelli, A. G.; Henry, E. M.; Volckens, J.; Dandy, D. S.; Henry, C.S. Rapid flow in multilayer microfluidic paper-based analytical devices. *Lab Chip*, **2018**, *18*, 793-802.
20. Channon, R. B.; Nguyen, M. P.; Henry, C. S.; Dandy, D. S. Multilayered Microfluidic Paper-Based Devices: Characterization, Modeling, and Perspectives. *Anal. Chem.* **2019**, *91*, 8966-8972.
21. Mendez, S.; Fenton, E. M.; Gallegos, G. R.; Petsev, D. N.; Sibbett, S. S.; Stone, H.A.; Zhang, Y.; López, G. P. Imbibition in porous membranes of complex shape: quasi-stationary flow in thin rectangular segments. *Langmuir*, **2010**, 26, 1380-1385.
22. Wang, X.; Hagen, J. A.; Papautsky, I. Paper pump for passive and programmable transport. *Biomicrofluidics* **2013**, *7*, 14107.
23. Kokalj, T.; Park, Y.; Vencelj, M.; Jenko, M.; Lee, L.P. Self-powered Imbibing Microfluidic Pump by Liquid Encapsulation: SIMPLE. *Lab Chip*, **2014**, *14*, 4329-4333.
24. Berthier, J.; Brakke, K. A.; Berthier, E. *Open-Microfluidics*; Scrivener-Wiley Publishing, 2016.
25. Berthier, J.; Theberge, A. B.; Berthier, E. *Open-Channel Microfluidics*; IOP Publishing, 2019.
26. Berthier, E.; Dostie, A. M.; Lee, U. N.; Berthier, J.; Theberge, A. B. Open Microfluidic Capillary Systems. *Anal. Chem.* **2019**, *91*, 8739–8750.
27. Lee, J. J.; J. Berthier, J.; Kearney, K.E.; Berthier, E.; Theberge, A.B. Open-channel capillary trees and capillary pumping. Langmuir, **2020**, *36*, 12795–12803.
28. Lee, J. J.; Berthier, J.; Theberge, A. B.; Berthier, E. Capillary Flow in Open Microgrooves: Bifurcations and Networks. *Langmuir* **2019**, *35* (32), 10667–10675.
29. Berthier, J.; Brakke, K. A.; Gosselin, D.; Navarro, F.; Belgacem, N.; and Chaussy, D. Spontaneous capillary flow in curved, open microchannels. Microfluid. Nanofluid. **2016**, *20*, 100.
30. Berthier, J.; Gosselin, D.; Berthier, E. A Generalization of the Lucas–Washburn–Rideal Law to Composite Microchannels of Arbitrary Cross Section. *Microfluid. Nanofluid.* **2015**, *19* (3), 497–507.
31. Darcy, H. Les Fontaines Publiques de La Ville de Dijon. V. Dalmont, 1856.
32. Whitaker, S. Flow in porous media I: A theoretical derivation of Darcy's law. *Transport in Porous Media*, **1986**, *1*, 3-25.
33. S. C. Amico, S. C.; Lekakou, C. Axial impregnation of a fiber bundle. Part 1: Capillary experiments. *Polym. Compos.* **2002**, *23*, 249-263.
34. Ashari, A.; H. Vahedi Tafreshi, H. General capillary pressure and relative permeability

expressions for throughplane fluid transport in thin fibrous sheets. Colloids Surfaces A: Physicochem. Eng. Aspects, **2009**, *346*, 114-122.
35. Dane, J. H.; Hofstee, C.; Corey, A. T. Simultaneous measurement of capillary pressure, saturation, and effective permeability of immiscible liquids in porous media. *Water Resour. Res.* **1998**, *34*, 3687-3692.
36. Babchin, A. J.; Bentsen, R.; Faybishenko, B.; Geilikman, M. B. On the capillary pressure function in porous media based on relative permeabilities of two immiscible fluids: Application of capillary bundle models and validation using experimental data. *Adv. Colloid Interface Sci.* **2016**, *233*, 176-185.
37. Zarandi, M. A. F.; Pillai, K. M.; Kimmel, A. S. Spontaneous imbibition of liquids in glass-fiber wicks. Part I: Usefulness of a sharp-front approach. *AIChE J.* **2017**, *64*, 294-305.
38. Reches, M.; Mirica, K. A.; Dasgupta, R.; Dickey, M. D.; Butte, M. J.; Whitesides, G. M. Thread as a Matrix for Biomedical Assays. *ACS Appl. Mater. Interfaces,* **2010**, *2*, 1722-1728.
39. Vasilakis, N.; Papadimitriou, K. I.; Morgan, H.; Prodromakis, T. High-performance PCB-based capillary pumps for affordable point-of-care diagnostics. *Microfluid. Nanofluidics*, **2017**, *21*, 103.
40. Safavieh, R.; Tamayol, A.; Juncker, D. Serpentine and leading-edge capillary pumps for microfluidic capillary systems. *Microfluid. Nanofluidics*, **2015**, *18*, 357-366.
41. Schaumburg, F.; Berli, C. L. A. Assessing the rapid flow in multilayer paper-based microfluidic devices. *Microfluid. Nanofluidics,* **2019**, *23*, 98.
42. Lade, R. K.; Hippchen, E. J.; Macosko, C. W.; Francis, L. F. Dynamics of Capillary-Driven Flow in 3D Printed Open Microchannels. *Langmuir* **2017**, *33* (12), 2949–2964.
43. Yang, L. J.; Yao, T. J.; Tai, Y.C. The marching velocity of the capillary meniscus in a microchannel. *J. Micromech. Microeng.* **2003**, *14*, 220.
44. Goedecke, N.; Eijkel, J.; Manz, A. Evaporation driven pumping for chromatography application. *Lab Chip*, **2002**, *2*, 219-223.
45. Nie, C.; Frijns, A. J. H.; Mandamparambil, R.; den Toonder, J. M. J. A microfluidic device based on an evaporation-driven micropump. *Biomed. Microdevices* **2015**, *17*, 47.
46. Liu, H.; Zhang, X.; Hong, Z.; Pu, Z.; Yao, Q.; Shi, J.; Yang, G.; Mi, B.; Yang, B.; Liu, X.; Jiang, H.; Hu, X. Nano Energy, **2017**, *42*, 115-121.
47. Berry, S. B.; Lee, J. J.; Berthier, J.; Berthier, E.; Theberge, A. B. Droplet Incubation and Splitting in Open Microfluidic Channels. *Analytical Methods* **2019**, *11* (35), 4528–4536.
48. Dal Dosso, F.; Tripodi, L.; Spasic, D.; Kokalj, T.; Lammertyn, J. Innovative Hydrophobic Valve Allows Complex Liquid Manipulations in a Self-Powered Channel-Based Microfluidic Device. *ACS Sensors,* **2019**, *4*, 694-703.
49. Elizalde, E.; Urteaga, R.; Berli, C. L. A. Rational design of capillary-driven flows for paper-based microfluidics. *Lab Chip*, **2015**, *15*, 2173-2180.
50. Berthier, J.; Brakke, K. A.; Gosselin, D.; Huet, M.; Berthier, E. Metastable capillary filaments in rectangular cross-section open microchannels. *AIMS Biophys.***2014**, *1*, 340-357.

Chapter 3 | On the Dynamic Contact Angle of Capillary-Driven Microflows in Open Channels

Reproduced in part from ***Tokihiro, J.C.;*** *McManamen, A.M.; Phan, D.N.; Thongpang, S.; Blake, T.D.; Theberge, A.B.;[#] Berthier, J.[#] On the dynamic contact angle of capillary-driven microflows in open channels. Langmuir,* ***2024****, 40 (13), 7215-7224.*
[#]Co-corresponding authors

JCT and AMM designed the microfluidic devices, conducted the flow experiments, and analyzed the video frames from the flow experiments. JCT and DNP developed the custom Python code for frame extraction. TDB and JB developed the theoretical model and JB applied the model to the experimental data. JB wrote and applied the MATLAB code to the experimental data. JCT, ST, ABT, and JB designed the study, interpreted the results, and conceptualized ideas. ABT and JB supervised the work. JCT, TDB, and JB wrote the manuscript with all authors revising.

Abstract: The true value of the contact angle between a liquid and a solid is a thorny problem in capillary microfluidics. The Lucas-Washburn-Rideal (LWR) law assumes a constant contact angle during fluid penetration. However, recent experimental studies have shown lower liquid velocities than predicted by the LWR equation, which are attributed to a velocity-dependent dynamic contact angle that is larger than its static value. Inspection of fluid penetration in closed channels has confirmed that a dynamic angle is needed in the LWR equation. In this work, the dynamic contact angle in an open channel configuration is investigated using experimental data obtained with a range of liquids, aqueous and organic, and a PMMA substrate. We demonstrate that a dynamic contact angle must be used to explain the early stages of fluid penetration, i.e., at the start of the viscous regime, when flow velocities are sufficiently high. Moreover, the open channel configuration, with its free surface, enhances the effect of the dynamic contact angle, making its inclusion even more important. We found that for the liquids in our study, the molecular-kinetic theory (MKT) is the most accurate in predicting the effect of the dynamic contact angle on liquid penetration in open channels.

3.1 Introduction

When a fluid flows in contact with a wall, its contact angle generally differs from its static value[1–3]. At the present time there are several approaches to predict the value of the dynamic contact angle (DCA) in the so-called viscous regime defined by Lucas, Washburn, and Rideal (LWR)[4–6]: the hydrodynamic model (HD), the molecular kinetic theory (MKT) and empirical or semi-empirical correlations based on the capillary number. The LWR law is widely used in capillary flows such as flows in channels and for flows in porous media[7,8]. This approach utilizes a static contact angle which assumes a constant contact angle throughout fluid flow. However, recent studies have shown that the use of the LWR law is applicable on a velocity-dependent basis, where in reality, the contact angle is larger than the static angle at high fluid velocities, resulting in the need for a DCA correction. This conclusion stems from the direct observation of the contact angle of spreading liquids on solid surfaces[8-11]. Dynamic contact angles are a real phenomenon. The question is how important is their effect on open channel microfluidics.

The basis for understanding the DCA has been established by, among others, de Gennes[9] who demonstrated that, for a partial wetting, the unbalanced interfacial tension forces, $F = \gamma\ (cos\theta_0 - cos\theta_d)$— where γ is the liquid/air interfacial tension (unit mN/m), q_d and q_0 are the dynamic and equilibrium contact angles respectively—must be compensated either by the viscous dissipation at a mesoscopic scale or by dissipation in the vicinity of the contact line or in the precursor film.

The hydrodynamic (HD) approach corresponds to the case of viscous dissipation at the mesoscopic scale resulting in so-called viscous bending near the wall (**Figure 3.1A**)[10–13].

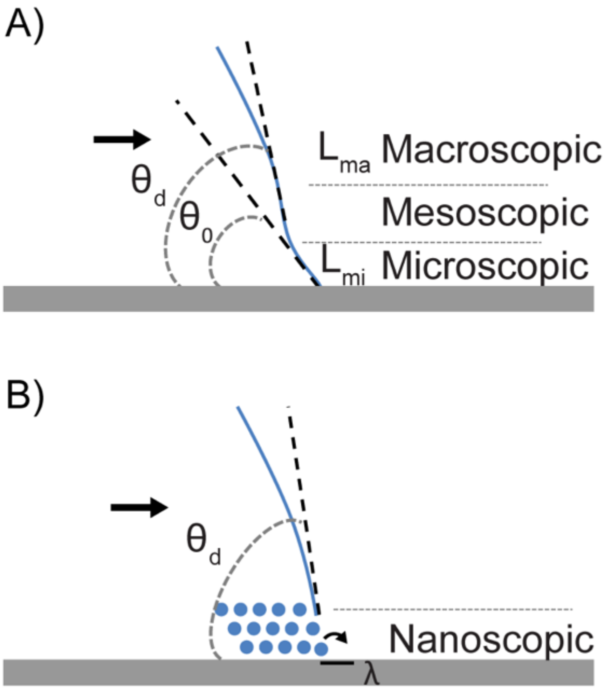

Figure 3.1. Sketches of the two main models for DCA: (A) the hydrodynamic model (HD) assuming a viscous bending at the wall; (B) the molecular dynamic theory (MKT) with the rolling motion of molecules at the wall.

In the HD approach, the increase in the contact angle outside of the microscopic region (L_{mi}) is linked to the cubic root of the capillary number[10]

$$\theta_d^3 = \theta_0^3 + 9\,\chi Ca = \theta_0^3 + 9\,ln(L_{ma}/L_{mi})\,Ca\ , \tag{1}$$

where Ca is the capillary number ($Ca = \mu V/\gamma$, μ being the fluid viscosity in mPa.s and γ the fluid surface tension) and χ is a parameter given by $\chi = ln(L_{ma}/L_{mi})$, L_{ma} being a macroscopic length scale which is of the order of the size of the meniscus and L_{mi} is a microscopic length scale, which is the cutoff length below which the continuum theory breaks down.

On the other hand, adsorption-desorption dynamics of liquid molecules on a solid surface near the TPCL (triple phase contact line) is the basis for the molecular kinetic theory (MKT, **Figure 3.1B**). This approach was first proposed by Blake and Haynes[14] using Eyring's activated-rate theory of stress-modified activated rate processes[15]. According to the MKT, to an approximation, the velocity-dependent dynamic contact angle is given by[14,16,17]

$$\Delta F_{cap} = \gamma\ (cos\theta_d - cos\theta_0) = -\zeta\ V, \tag{2}$$

where ζ is the coefficient of contact line friction per unit length of the contact line (unit Pa.s). Strictly speaking, this simple linear form applies only near equilibrium or where the energy barriers to contact-line movement are small; but as we are interested only in the way in which a change in the dynamic contact angle may provide a correction to the viscosity-dominated flow in the channel, this form is adequate for our immediate purposes.

It was later demonstrated[16–19] that the contact-line friction is related to the equilibrium work of adhesion, Wa, by

$$\frac{\zeta}{\mu} \cong \frac{V_m}{\lambda^3} \exp\left(\frac{W_a}{n\ k_B T}\right) \cong \frac{V_m}{\lambda^3} \exp\left(\frac{\lambda^2 W_a}{k_B T}\right) \tag{3}$$

where λ is the characteristic distance of each molecular displacement (**Figure 3.1B**), k_B is the Boltzmann constant ($k_B \approx 4.14\ pN/nm$), *T* is the temperature (in Kelvin), V_m is the molecular flow volume of the liquid, here approximated by the molecular volume. In (3), *n* is the number of solid-liquid interaction sites per unit area of the solid surface, provided these are distributed uniformly, $n \cong 1/\lambda^2$. Note that at a more fundamental level, ζ is related to the characteristic molecular frequency κ^0(the frequency of molecular absorption, unit MHz) and distance λ for molecular displacements in the vicinity of the triple line: $\zeta = nk_B T/\kappa^0\ \lambda \sim k_B T/\kappa^0\ \lambda^3$.

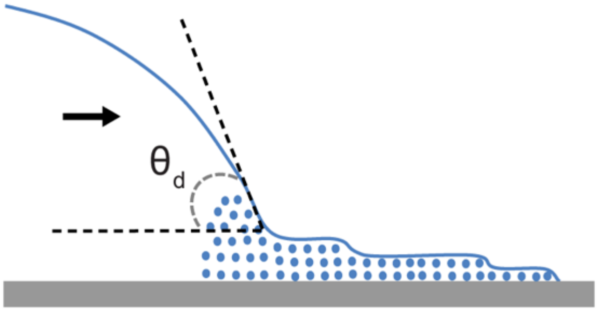

Figure 3.2. Sketch of the molecular kinetic theory – self layering approach where the precursor film is composed of layers of fluid molecules (represented as blue circles).

Note that, in the specific case of the existence of a precursor film[20,21] (where a thin sheet of fluid precedes the TPCL), a modified approach of MKT—called MKT-self-layering—assumes the formation of layers of molecules in the precursor film at the wall combined with the adsorption-desorption phenomenon (**Figure 3.2**)[22–24]. In this model, the wall viscosity, β, is then given by

$$cos\theta_d - cos\theta_0 = -\beta\, V, \tag{4}$$

with $\frac{\beta}{\mu} = \exp\,(\frac{2\,\gamma}{n\,k_BT})$, where μ is the viscosity of the flowing liquid, and *n* is the number of molecules per unit area in the precursor thin film, which is related to σ or the effective diameter of the molecules in the thin film by $n = 1/\sigma^2$.

Finally, let us remark that empirical and semi-empirical correlations have been proposed to predict the value of the DCA. These correlations make use of the capillary number and have the form[25–30]

$$cos\theta = cos\theta_0 - A(1 + cos\theta_0)\, f(Ca)\,, \tag{5}$$

where *A* is a non-dimensional coefficient and *f* is a monotonously increasing function. In many of these correlations, the function, *f*, is of the form, $f(A) = Ca^B$, where Ca is the capillary number, *A* ranges between 2 and 4.96, and *B* is a non-dimensional constant (ranging between 0.42 and 0.7). The term $1 + cos\theta_0$ represents the adhesion energy, $Wa = \gamma\,(1 + cos\theta_0)$.

In this work, we focus on the dynamic contact angle in capillary flows in open channels[31–33]. Contrary to traditional closed channel microfluidics, open channels are characterized by one or more air-liquid interfaces through the removal of at least one channel wall. Open channels have recently gained attention in the microfluidics community due to advantages such as accessibility, easy fabrication or surface treatment of the microfluidic channels, and the reduction in bubble formation during fluid addition and flow. These devices are simple to operate, necessitating only a micropipette, fluid of choice, and the open channel device. Open microfluidics has become widely used in a variety of research fields such as cell culture, protein and metabolite assays, organ-on-a-chip models, and even space applications[34–37]. To some extent, the physics of the microflow in open channels resembles that in closed channels, but some considerations must be adopted for open-channel flow. The LWR law must be modified by using an equivalent contact angle[32,33] —the so-called generalized Cassie angle–in place of the contact angle, and an average friction length in place of the tube radius. It is shown here that, in the early stages of the viscous regime, a dynamic contact angle (DCA) should be used and, based on our experiments, that the most accurate approach is the molecular kinetic model. Our study employs rectangular open-channels milled in poly(methyl methacrylate) (PMMA)—slightly rounded at the bottom inner corners to avoid capillary filaments[38], and several different liquids including water, nonanol, pentanol, chloroform, FC-40, and an aqueous solution of 50% (v/v) isopropyl alcohol.

3.2 Results and Discussion

3.2.1 Theoretical approach

Using the geometry of the open channel, the LWR law yields the relation between velocity, *V,* and travel distance, *z,*

$$V = \frac{\gamma}{\mu}\frac{\bar{\lambda} cos\theta^*}{z}, \qquad (6)$$

where $\bar{\lambda}$ is the average friction length which describes the wall friction (unit mm), θ^* is the generalized Cassie angle which accounts for the effect of the free surface, *g* is the surface tension of the liquid, and *m* is the viscosity. Relation (6) can be rewritten in terms of the capillary number (*Ca*):

$$Ca = \frac{\mu}{\gamma}V = \frac{\bar{\lambda}cos\theta^*}{z} \quad . \qquad (7)$$

Here, the DCA depends on the value of the velocity, represented by the capillary number. Relation (7) shows that if the travel distance is sufficient and/or the channel cross section is sufficiently small ($\bar{\lambda}/z \ll 1$), the use of the static contact angle is justified. Conversely, if this condition is not met, a DCA is present and changes the dynamics of the flow.

In this section, it is shown that the MKT approach can be applied analytically, leading to an easy modification of the extended LW law to take into account the dynamic contact angle. This observation was also made by Wu *et al.*[24] for capillary rise, using the LWR law with an equivalent radius.

In the viscous regime, the capillary force (F_{cap}) balances the wall friction force (whether the channel is closed or open), and

$$F_{cap} = p\ \gamma cos\theta^* = F_{drag} = p\ z\ \mu\frac{V}{\bar{\lambda}} \, . \qquad (8)$$

In relation (8), *z* is the marching—or travel—distance (unit mm), *p* is the total perimeter of a cross section (including the liquid/air boundary if any) (unit mm), $\bar{\lambda}$ is the average friction length[32], and θ^* is the generalized Cassie angle[52] . Substituting $V = dz/dt$, relation (8) can be written as

$$zV = \frac{1}{2}\frac{dz^2}{dt} = \frac{\gamma}{\mu}\bar{\lambda}\ cos\theta^* \ , \qquad (9)$$

or

$$z^2 = \frac{\gamma}{\mu} 2\bar{\lambda} \int_0^t cos\theta^* dt \ , \tag{10}$$

In the case where θ^* is constant, the usual extended Lucas-Washburn law is retrieved. Using the expression of the generalized Cassie angle (27), relation (10) becomes

$$z^2 = \frac{\gamma}{\mu} 2\bar{\lambda} \int_0^t \left(\frac{p_W}{p} cos\theta - \frac{p_F}{p} \right) dt \ . \tag{11}$$

Now, let us use the MKT correlation (2) to express the dynamic contact angle

$$z^2 = \frac{\gamma}{\mu} 2\bar{\lambda} \int_0^t \left[\frac{p_W}{p} \left(cos\theta_0 - \frac{\zeta}{\gamma} V \right) - \frac{p_F}{p} \right] dt = \frac{\gamma}{\mu} 2\bar{\lambda} \int_0^t \left[\left(\frac{p_W}{p} cos\theta_0 - \frac{p_F}{p} \right) - \frac{p_W}{p} \frac{\zeta}{\gamma} \frac{dz}{dt} \right] dt \ , \tag{12}$$

or

$$z^2 = \frac{\gamma}{\mu} 2\bar{\lambda} \, cos\theta_0^* t - \frac{\gamma}{\mu} 2\bar{\lambda} \int_0^t \frac{p_W}{p} \frac{\zeta}{\gamma} \frac{dz}{dt} dt \ . \tag{13}$$

The first term in (13) is the travel distance using the static contact angle ($z_0^2 = \frac{\gamma}{\mu} 2\bar{\lambda} \, cos\theta_0^* t$), and the second term is a correction due to the dynamic contact angle. Relation (13) can be simplified as

$$z^2 = \frac{\gamma}{\mu} 2\bar{\lambda} \, cos\theta_0^* t - 2\bar{\lambda} \frac{p_W}{p} \frac{\zeta}{\mu} z \ . \tag{14}$$

The real travel distance—accounting for the dynamic contact angle correction—is then solved using the quadratic equation:

$$z^2 + 2\bar{\lambda} \frac{p_W}{p} \frac{\zeta}{\mu} z - z_0^2 = 0 \ . \tag{15}$$

In (15), we must keep in mind that *z* and *z₀* are functions of the time, *t*. Therefore, we finally obtain:

$$z = -\bar{\lambda} \frac{p_W}{p} \frac{\zeta}{\mu} + \sqrt{\left(\bar{\lambda} \frac{p_W}{p} \frac{\zeta}{\mu} \right)^2 + z_0^2} \ . \tag{16}$$

It is verified that at $t = 0$ (we neglect the evanescent inertial motion[53]), $z_0 = 0$ and $z = 0$. For a long channel, z_0 becomes large and $z \rightarrow z_0$. Flow velocity can be easily deduced from (16) by time differentiation:

$$V = \frac{V_0}{\sqrt{1+\frac{\left(\bar{\lambda}\frac{p_W}{p}\frac{\zeta}{\mu}\right)^2}{z_0^2}}} , \tag{17}$$

where V_0 is the velocity obtained using the static contact angle, $V_0 = dz_0/dt$. When the travel distance increases, z_0 increases and the real velocity V converges towards the velocity, V_0. Note that when z_0 goes to zero, z goes to zero, and relation (17) indicates that V goes to $V(z \rightarrow 0) = V_0 z_0 / \bar{\lambda}\frac{p_W}{p}\frac{\zeta}{\mu} = p\, \gamma cos\theta^* / \zeta p_W$, indicating that ζ acts like a viscosity associated with the triple line. However, in reality, relation (17) holds when the inertial regime ends i.e., when $z_0 > z_{inertial}$.

3.2.2 *Experimental results and comparison with model*

The importance of the DCA is directly linked to the velocity of the flow. As the flow velocity in the channel is proportional to the ratio of the surface tension and viscosity $\mathrm{V} \approx (\gamma/\mu)/z$, we have categorized the fluids as "fast" and "slow" as a function of their intrinsic velocity, $V_i = \gamma/\mu$. The "fast" fluids correspond to high values of V_i ($V_i \gtrsim 30\ m/s$) and "slow" fluids by low values of V_i ($V_i \lesssim 8\ m/s$).

Water and chloroform are in the first category. **Figure 3.3** shows the dynamics of these two fluids in channels of different cross sections. Clearly, the LWR law which uses the static (Young) contact angle does not account for the flow velocity. A DCA is required to fit the experimental results as seen in **Figure 3.3** where the experimental travel distances and velocities are closely fitted to the values predicted by the DCA theory (blue line). This DCA is obtained using ζ= 0.32 Pa.s for water and 0.20 Pa.s for chloroform.

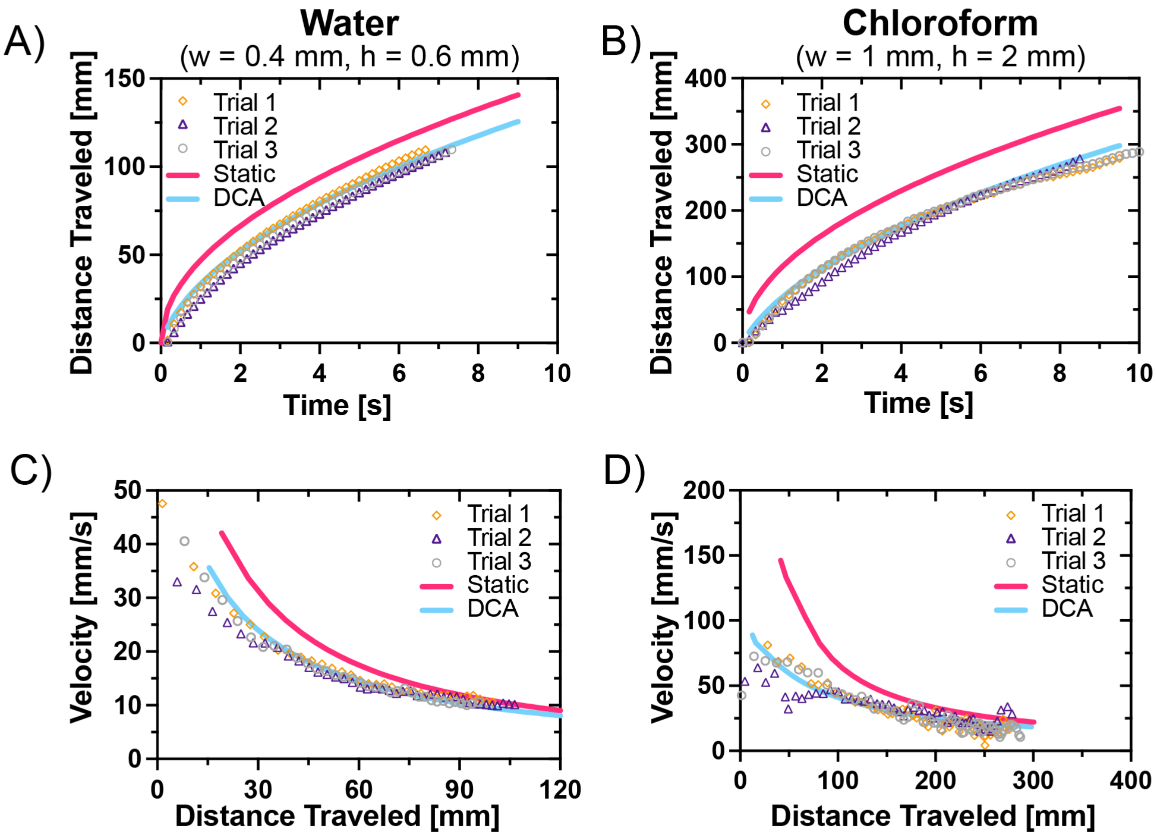

Figure 3.3. Comparison of models using the static and dynamic angles. Plots of travel distance vs. time for water in channel #3 (w = 0.4 mm, h = 0.6 mm) (**A**) and chloroform in channel #1 (w = 1 mm; h = 2 mm) (**B**): comparison between the static contact angle (pink line), dynamic contact angle model (blue line) and experiments (circles, triangles, and diamonds). Plots of velocity vs. travel distance for water (**C**) and chloroform (**D**): comparison between the static contact angle model (pink line), dynamic contact angle model (blue line), and experiments (circles, triangles, and diamonds).

The solution of 50% (v/v) isopropyl alcohol in water is located in the “intermediate” fluids, categorized by a moderate $V_i = \gamma/\mu$ value. **Figure 3.4** shows the dynamics of the flow in relatively large channels (w = 1 mm, h = 2 mm) (**Figure 3.4A** and **C**) compared to small cross sections (w = 0.4 mm, h = 0.4 mm) (**Figure 3.4B** and **D**).

In the first case, where a large cross section was used, a DCA is needed to account for the dynamics as shown through the experimental data clustering around the theoretical DCA travel distances and velocities (**Figure 3.4A** and **C**). On the other hand, the static angle (pink line) is sufficient in the second case of small cross sections (**Figure 3.4B** and **D**). The explanation is related to the value of the velocities, which are high in the first case, and small in the second case.

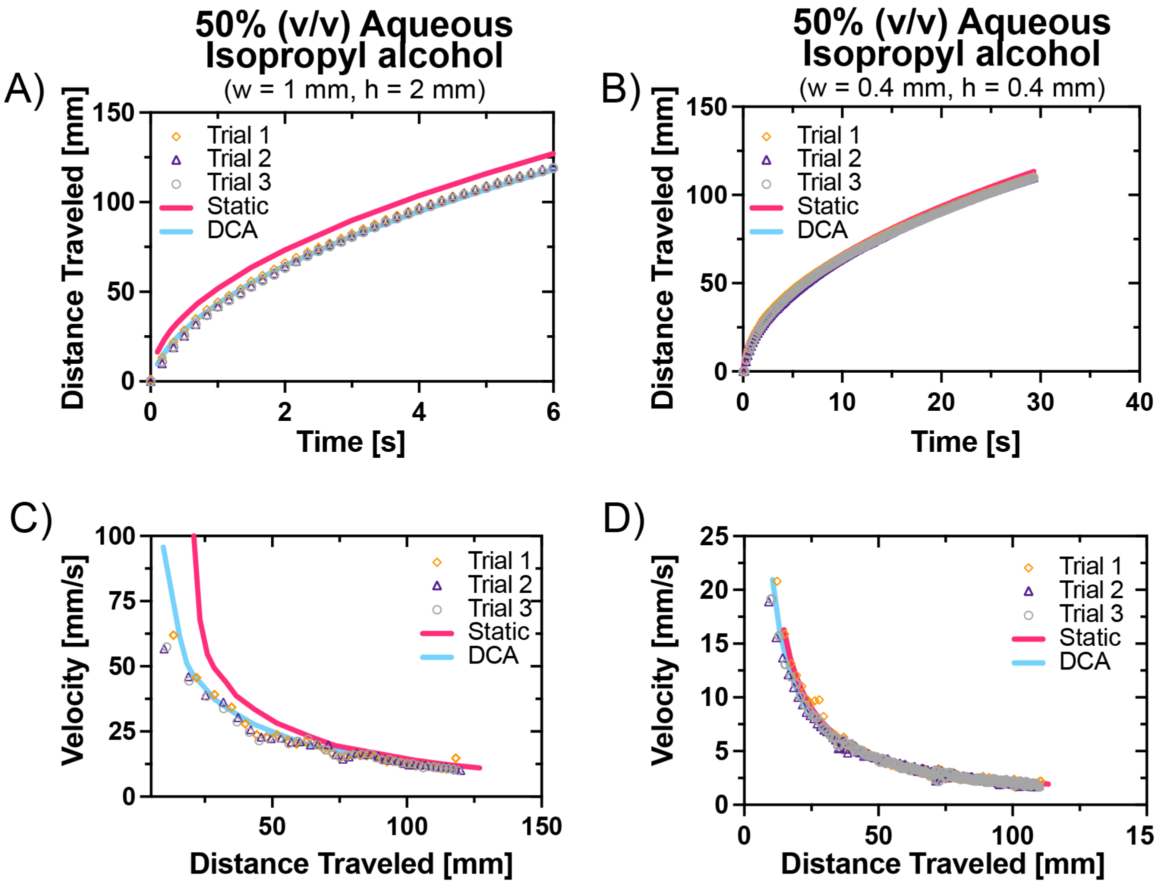

Figure 3.4. Comparison of models using the static and dynamic angles. Plots for travel distance vs. time for 50% (v/v) aqueous isopropyl alcohol in channel #1 (w = 1 mm, h = 2 mm) (**A**) and in channel #4 (w = 0.4 mm; h = 0.4 mm) (**B**): comparison between the static contact angle model (pink line), dynamic contact angle model (blue line), and experiments (circles, triangles, and diamonds). Plots of velocity vs. travel distance for 50% (v/v) isopropyl alcohol in channel #1 (w = 1 mm, h = 2 mm) (**C**) and in channel #4 (w = 0.4 mm; h = 0.4 mm) (**D**): comparison between the static contact angle model (pink line), dynamic contact angle model (blue line), and experiments (circles, triangles, and diamonds).

In the last case of “slow” fluids, the preceding observation is still valid. **Figure 3.5** shows a comparison of the dynamics of pentanol and nonanol in large channels (w = 2 mm, h = 2 mm) for which the wall friction is minimal. A DCA is needed in the case of pentanol (V_i~7 m/s) (**Figure 3.5A** and **C**), but it is not needed for the case for nonanol (V_i~2.5 m/s) (**Figure 3.5B** and **D**).

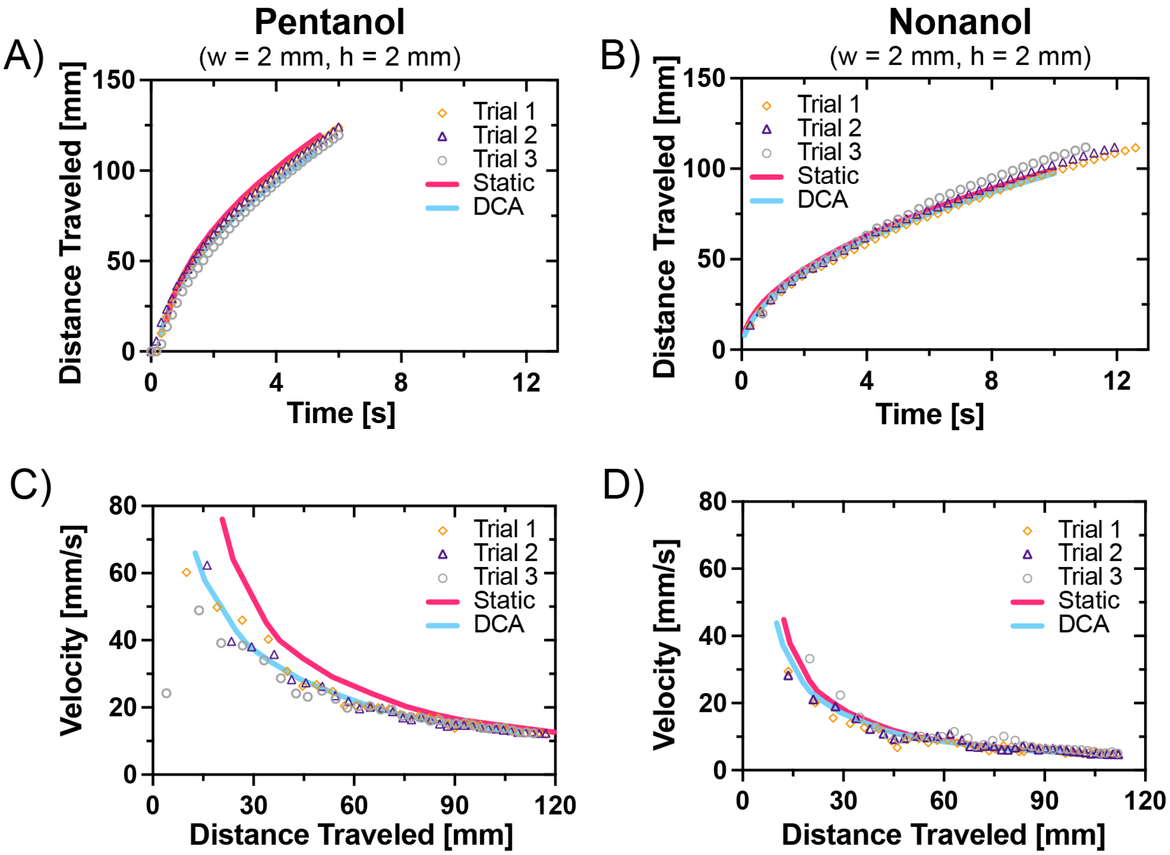

Figure 3.5. Comparison of models using the static and dynamic angles. Plots of travel distance vs. time for pentanol (**A**) and nonanol (**B**) in channel #2 (w = 2 mm, h = 2 mm): comparison between the static contact angle model (pink line), dynamic contact angle model (blue line), and experiments (circles, triangles, and diamonds). Plots of velocity vs. distance for pentanol (**C**) and nonanol (**D**): comparison between the static contact angle model (pink line), dynamic contact angle model (blue line), and experiments (circles, triangles, and diamonds).

3.2.3 Comparison with other correlations

In this section, we briefly present other correlations for DCA and compare them to the MKT approach used in section 3.

Hydrodynamic correlation proposed by Hoffman and Tanner[25,26] yields

$$\theta = 4.5\ Ca^{\frac{1}{3}}\,. \tag{18}$$

Bracke *et al.* correlation[28,29] links the cosine of the dynamic contact angle to the capillary number:

$$cos\theta = cos\theta_0 - 2(1 + cos\theta_0)\, Ca\ . \tag{19}$$

This correlation is very similar to the Seebergh and Berg[30] correlation, while the Jiang *et al.* correlation[27] yields:

$$cos\theta = cos\theta_0 - (1 + cos\theta_0)\, 4.96 \tanh\,(Ca^{0.702})\ . \tag{20}$$

In order to investigate the effectiveness of these empirical correlations to account for the influence of a dynamic contact angle in the LWR equation, a numerical scheme was set up in a MATLAB file[54] for each correlation. A comparison of the different correlations is shown in **Figure 3.6A** for water flowing in the channel #3 (w = 0.4 mm, h = 0.6 mm). Comparison for chloroform and 50% (v/v) isopropyl alcohol are shown in Appendix Section B1.2.

The evolution of the DCA with the distance is plotted in **Figure 3.6A** for the capillary flow of water in channels of cross section, w = 0.4 mm and h = 0.6 mm. The different approaches—constant static contact angle, HD correlations, and MKT—are compared. The MKT approach is the only one that fits the experimental data.

The generalized DCA given by its cosine,

$$cos\theta_d^* = \frac{p_W}{p} cos\theta_d - \frac{p_F}{p}, \tag{21}$$

depends on the capillary number and is shown in **Figure 3.6B** (the value at *Ca* = 0 corresponds to the static Young angle) for the different correlations (Bracke *et al.*[28], Jiang *et al.*[27], Hoffman[25]) using the data for water. The results are very similar except for the MKT correlation with a coefficient ζ = 0.35 Pa.s.

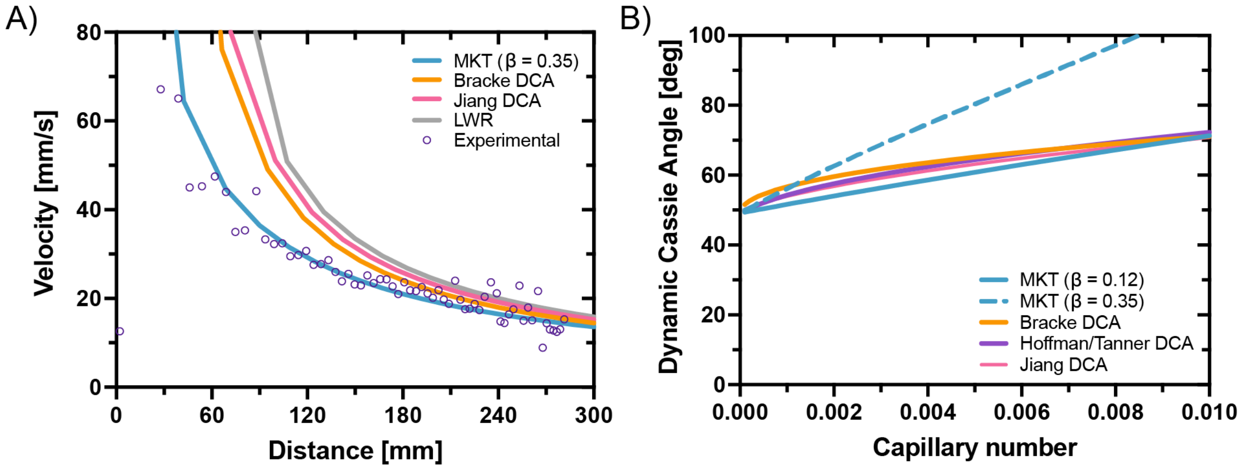

Figure 3.6. A: Comparison of the velocity of a water flow in channel #3 between experiments (open circles), and different correlations. **B:** Comparison between the dynamic contact angles (Cassie generalized contact angles) obtained using the different correlations described in the text in function of the capillary number. The two blue lines correspond to MKT correlations for ζ= 0.12 (blue solid line) and 0.35 Pa.s (blue dotted line).

In **Figure 3.7A** and **B**, the relations between the DCA and the velocity and between the DCA and the travel distance, respectively, are shown for the different liquids used in this work. The importance of taking into account a DCA is evident for the first 50 mm of the open channels.

Let us first remark that the advantage of using an open-channel configuration to assess the MKT approach is the increased sensitivity of the flow velocity to the DCA. A correction, ε, to the cosine of the contact angle has a stronger influence on the capillary force in the case of an open flow:

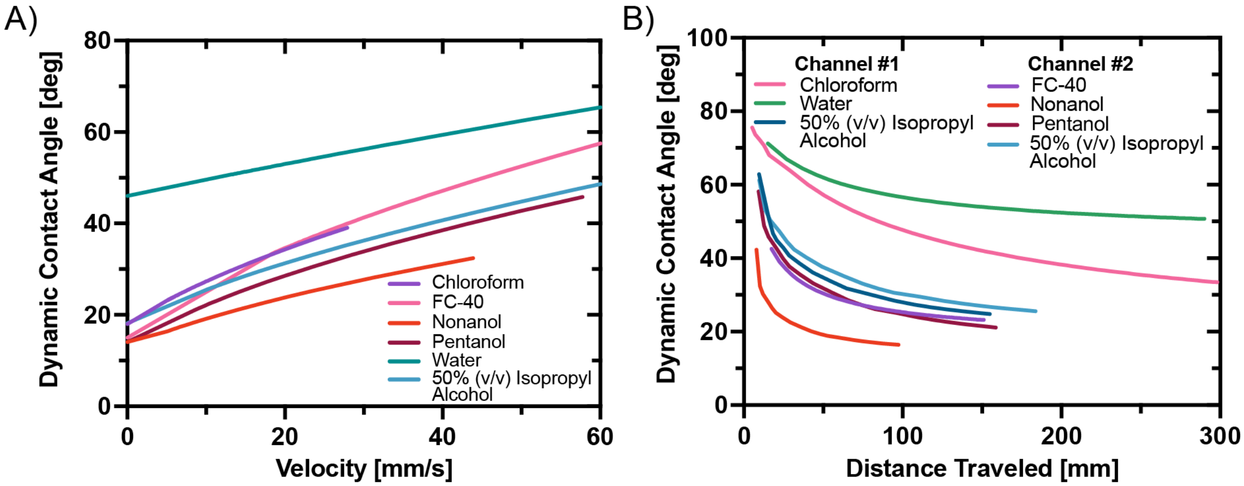

Figure 3.7. A: DCA vs. velocity for the 6 liquids (in the case of water, the PMMA has been treated with O_2 plasma) and **B:** evolution of the DCA with the distance in the channel for in different cases investigated in this work.

$$\frac{\Delta F_{cap}}{F_{cap}}(open) = \frac{(cos\theta_0^* - \varepsilon)}{cos\theta_0^*} = 1 - \frac{\varepsilon}{(p_W/p)\, cos\theta_0 - p_F/p}\ , \tag{22}$$

compared to

$$\frac{\Delta F_{cap}}{F_{cap}}(closed) = 1 - \frac{\varepsilon}{cos\theta_0}. \tag{23}$$

The sensitivity of an open microflow in a rectangular channel has recently been pointed out by Chang *et al.*[53].

3.2.4 Comparison between inertial and viscous regimes

A second remark is focused on the flow regimes (inertial or viscous). In the inertial regime, the velocity field is not established[55]; even if there is the effect due to the triple line friction on the contact angle, the different models presented here cannot be used. We verify that the experimental results used in this work correspond to the viscous regime. In **Figure B6**, the transition times and distances for the liquids and channels used in this study are calculated and listed. It is checked that the corrections associated with ζ shown in **Figures 3.3**, **3.4**, and **3.5** correspond to the viscous regime and not the inertial regime. In Table 3.1, the inertial-viscous transitions for the different cases of **Figures 3.3**, **3.4**, and **3.5** are listed. These times (t_{in}) and travel distance (z_{in}) transitions are located at the very beginning of the velocity vs. distance plots and do not interfere with the MKT approach (and other approaches).

Table 3.1. Transition data between inertial and viscous regimes.

	Channel	Liquid	t_{in} [ms]	z_{in} [mm]
Figure 3.3				
	#3	Water	2.7	1.9
	#1	Chloroform	46	12.3
Figure 3.4				
	#1	50% (v/v) isopropyl alcohol	5.7	2.0
	#4	50% (v/v) isopropyl alcohol	0.7	0.4
Figure 3.5				
	#2	Pentanol	4.0	2.9
	#2	Nonanol	17	4.0

3.2.5 Determination of molecular displacement distance

Finally, we determine the values of the molecular displacement distance (λ) of the MKT approach. Using the software, MATLAB[54], we iteratively determine the values of λ by solving the discretized equation (3) using the experimental fit of ζ

$$\lambda_{i+1}^2 = \frac{k_B T}{W_a}\left\{ln\left(\frac{\zeta}{\mu}\right) - ln\left(\frac{V_m}{\lambda_i^3}\right)\right\}, \tag{24}$$

where *i* is the iteration index. Convergence is rapidly obtained in less than 10 iterations. The displacement distances are listed in the **Table 3.2**. The values of the molecular displacement frequency, κ^0, can then be extracted using the relationship $\kappa^0 = nk_B T/\zeta\,\lambda$. The resulting values λ and κ^0 are listed in **Table 3.2**. The values are usually obtained by direct measurement of the dynamic contact angle and applying the full, non-linear version of the MKT[16]. Such measurements are inherently problematic in microfluidic channels.

Table 3.2. Values of the adhesion energy, W_a, coefficient of line friction z, molecular displacement distances λ for the different liquids and cubic root of molecular diameter ${V_m}^{1/3}$.

	W_a [mN/m]	z [Pa.s]	λ [nm]	${V_m}^{1/3}$ [nm]	k^0 [MHz]
Pentanol	54.6	0.12	0.45	0.56	378
Nonanol	57.1	0.18	0.30	0.66	851
50% (v/v) Isopropyl Alcohol	62.4	0.12	0.56	0.39	196
FC-40	31.3	0.22	0.61	0.84	82
Chloroform	53.1	0.20	0.52	0.51	147
Water	134.4	0.32	0.51	0.31	101

Note that, as expected, the displacement distances are in the range of 4 to 7 Angstroms, which is of the order of the cubic root of the molecular volume (V_m): $\lambda^3 \sim V_m$.

Figure 3.8 shows that the values of the contact-line frictions ζ are in agreement with literature (see **Figure B7**)

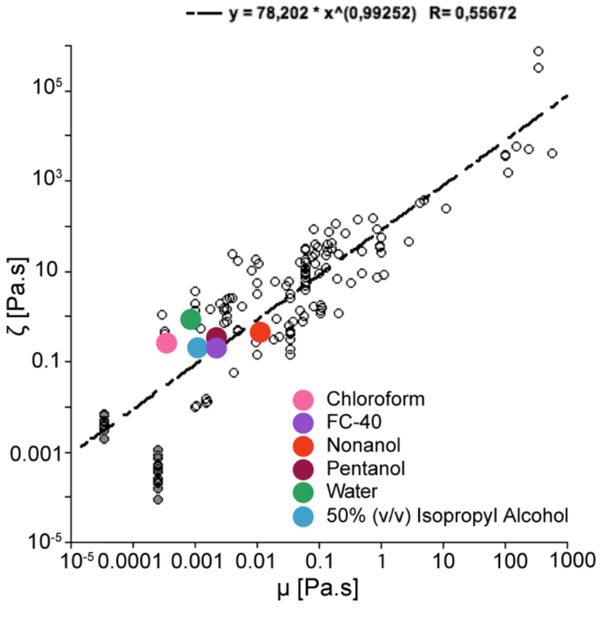

Figure 3.8. Plot of z vs. μ: Comparison of the values collated from the literature (black symbols) and the present study (colored circles)[17]. The literature references are listed in Appendix Section B3. Reproduced with permission from reference 17. Copyright 2013 American Chemical Society.

3.3 Conclusion

Open channel fluidics is a rapidly expanding area of interest for both research and a wide range of potential applications. This is primarily due to advantages such as accessibility, ease of fabrication and surface treatment. However, our understanding of the flow behavior of liquids in such devices remains incomplete, particularly as regards the significance of the dynamic contact angle.

Here, we have developed a model for the influence of the dynamic contact angle on open-channel flow in the viscous regime based on the molecular-kinetic theory of dynamic wetting (MKT). This model introduces the concept of triple-line friction due to localized dissipation processes and explains the increase in the contact angle[16]. In our new work, a closed-form solution is obtained, which shows that if account is taken of the dynamic contact angle, the real travel distance is equal to that given by the generalized Lucas-Washburn-Rideal (LWR) law for open-channels[32,33] minus a correction that correlates the dynamic contact angle with the velocity. These predictions have been validated in experiments carried out for a range of liquids in rectangular open channels made of PMMA. Overall, our experiments point to the same conclusion as Li *et al.* for ionic liquids on fluoropolymer surfaces[56], that the molecular kinetic model accounts more precisely for the dynamic contact angle in capillary flows than the hydrodynamic model.

Significantly, the real velocity of the flow is smaller than the LWR velocity, as reported in the literature for capillary-driven microflows. This is especially important in the first few centimeters of the channel, where the velocity of flow in the early viscous regime is relatively high, and will need to be taken into account in future design and modelling of open-channel fluidic devices where the free surface enhances the effect of the dynamic contact angle.

One additional aspect of the new work is that by combining the measured coefficients of triple-line frictions ζ with a semi-empirical correlation that links the friction to the work of adhesion between the liquid and the solid[18], we have been able to extract reasonable values for the underlying MKT parameters, the molecular jump frequency $\kappa^0$and distance λ that determine ζ, without resorting to direct measurement of the dynamic contact angle, which is inherently difficult in microfluidic channels.

3.4 Materials and Methods

3.4.1 Channel Design and Fabrication

Four different open rectangular channels milled in PMMA have been used: channel #1 (w = 1 mm, h = 2 mm), channel #2 (w = 2 mm, h = 2 mm), channel #3 (w = 0.4 mm, h = 0.6 mm), and channel #4 (w = 0.4 mm, h = 0.4 mm). An engineering drawing of channel #1 is shown in **Figure 3.9**. Detailed engineering drawings of channels #1-4 can be found in **Figure B1**. Calibration markers separated by a known distance apart were milled into the device for scaling purposes during image analysis (**Figure 3.9A**). A profilometer photo of the rounded corners is shown in **Figure 3.9B**.

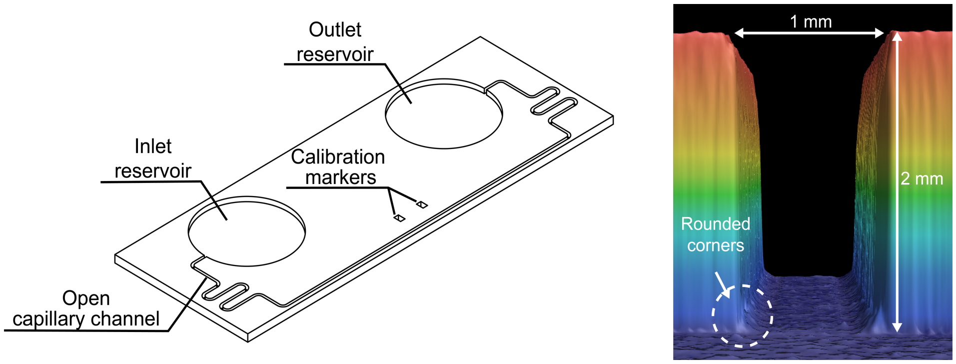

Figure 3.9. A: Isometric view of channel #1 milled in PMMA and **B:** profilometer cross-section of the channel with the rounded corners.

The characteristics of the channels are listed in **Table 3.3**.

Table 3.3. Characteristics of the channels.

Channel	Width	Height	Max channel length	Wetted perimeter	Free perimeter	Friction length
Symbol *units*	*w* *[mm]*	*h* *[mm]*	*l* *[mm]*	p_W *[mm]*	P_F *[mm]*	$\bar{\lambda}$ *[mm]*
Channel #1	1.0	2.0	303	5.0	1.0	0.22
Channel #2	2.0	2.0	120	6.0	2.0	0.44
Channel #3	0.40	0.60	110	1.6	0.4	0.09
Channel #4	0.40	0.40	110	1.2	0.4	0.07

The average friction lengths (rightmost column in **Table 3.3**) representing the wall friction are first approximated by the semi-empirical formulations[33,39] for a rounded-bottom rectangular open channel

$$\bar{\lambda} \cong \frac{1}{3} \frac{w+h}{\left(\frac{2h}{w}+\frac{w}{h}\right)}, \tag{25}$$

Note that for a straight-bottom rectangular open channel, an expression of the friction has been found[40–43].

$$\bar{\lambda} \cong \frac{2}{3} \frac{h}{w} \chi\left(\frac{h}{w}\right)(w+h), \tag{26}$$

where $\chi\left(\frac{h}{w}\right) = 1 + 0.671\frac{h}{w} + 4.1697\left(\frac{h}{w}\right)^2$.

These two formulas produce approximate values of the friction length for moderate aspect ratio rectangular open channels. Note that the second formula corresponds to the case of rectangular channels with sharp inner corners where filaments are present[44]. Hence the two formulas somewhat differ when considering the same aspect ratio channel (see **Appendix Section B2**). The value of the friction length—approximated by (25) —is adjusted on the experimental plots for the flow velocity, using velocities far from the channel entrance, where the contact angle most resembles the static contact angle—as will be shown later in the text (**Figure 3.10**).

The channels were designed using a computer-aided design (CAD) software (Solidworks 2017, Waltham, MA) and the design files were converted to a .simpl file using a computer-aided manufacturing (CAM) software (Fusion 360, Autodesk, San Rafael, CA). Channels were milled in PMMA sheets (3.175 mm thick, #8560K239; McMaster-Carr, Sante Fe Springs, CA).

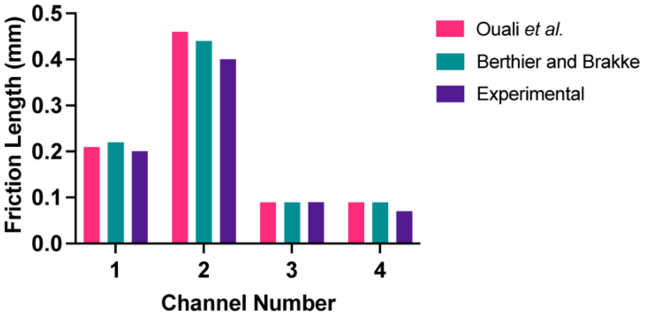

Figure 3.10. Comparison of the different approaches for the friction length: Ouali *et al.*[40] (pink color); Berthier and Brakke[33] (teal color); experiments (purple color).

To create round bottom channels, endmills with a cutter diameter of 1/32" (TR-2-0312-BN) or 1/64" (TR-2-0150-BN) were used (Performance Micro Tool, Janesville, WI). The devices were fabricated via micro-milling on a Datron Neo computer numerical control (CNC) mill (Datron, Germany). After fabrication, the channel dimensions were confirmed using a Keyence wide-area 3D measurement VR-5000 (Keyence Corporation of America, Itasca, IL). The channel bottom is estimated to have a few microns of roughness—due to the milling process— which is one magnitude below the roughness values observed by Lade *et al.* to produce substantial fluctuations in velocity[42]. Note that the effect of small roughness on open-capillary flow dynamics is not yet completely understood, since small reliefs on the wall surface slightly increase the capillary force —due to the Wenzel effect[45] —but also slightly increase the friction force[46]. In our case, the adjustment of the friction length indirectly takes this effect into account.

3.4.2 Solvent Prep and Physical Properties

Various solvents have been used in this study. Aqueous solvents included: deionized and distilled water (American Society for Testing and Materials Type II, HARLECO, Sigma-Aldrich, St. Louis, MO) as well as isopropyl alcohol at a concentration of 50% (v/v) in deionized and distilled water. These solvents were colored with 0.60 % yellow or 1.2 % blue food coloring. (McCormick). Organic compounds such as nonanol (Sigma-Aldrich, St. Louis, MO), pentanol (Sigma-Aldrich, St. Louis, MO), and chloroform (Fisher Scientific, Hampton, NH) have been colored with either Solvent Yellow 7 or with Solvent Green 3 (Sigma-Aldrich, St. Louis, MO) at concentrations of 0.50 mg/mL and 1.43 mg/mL respectively. FC-40 (Sigma-Aldrich, St. Louis, MO) was not colored, but tracking its travel in the channel was still feasible. In the case of water, the channel was treated by oxygen plasma using a Diener Zepto PC EX Type PB plasma treater (Diener Electronic, Germany) no more than 30 minutes prior to experimentation, to avoid contact angle relaxation[47,48]. The physical data for these liquids are listed in **Table 3.4**.

Table 3.4. Properties of the liquids.

	γ [mN/m]	μ [mPa.s]	θ	w [mm]	h [mm]	cos θ*
Water	72	1.0	46	0.4	0.6	0.30
Chloroform	28	0.6	15	1	2	0.64
50% (v/v) Isopropyl alcohol	30	3.0	18	0.4	0.4	0.46
50% (v/v) Isopropyl alcohol	30	3.0	18	1	2	0.63
50% (v/v) Isopropyl alcohol	30	3.0	18	2	2	0.46
FC-40	16	2.5	17	1	2	0.63
Pentanol	25	3.7	13	2	2	0.48
Nonanol	27	11.5	13	2	2	0.48

*Note: These values are from Kim *et al.* 2016[49] and Mohammad *et al.* 2014[50]

The values of the surface tensions and viscosities of the liquids have been taken from physical tables and the literature[49,50]. Surface tension measurements are reported as the surface tension between the air-liquid interface. The contact angles with PMMA have been measured in Lee *et al*. 2019[51] using a Kruss DSA-25E drop shape analyzer (Kruss GmbH, Hamburg, Germany). Contact angles are reported as the average of 5 2-µL droplet measurements collected with the Kruss ADVANCE software. The generalized Cassie angle θ^* was calculated using the static contact angle and the weighted average of the contact angle of each fluid with the wall and the atmosphere. This is defined by:

$$cos\theta^* = \frac{p_W}{p} cos\theta_0 - \frac{p_F}{p}, \tag{27}$$

where θ_0 is the Young (static) contact angle, $p_W$and p_F are the wetted and free perimeters in a cross section, and $p = p_W + p_F$. In the present case, setting the cross section to a rectangle of width, *w,* and height, *h:*

$$cos\theta^* = \frac{(w+2h)cos\theta_0 - w}{2\,(w+h)}. \tag{28}$$

3.4.3 Open-Channel Flow Experiments

To obtain fluid velocities, the prepared fluids were flowed through the uniform cross section channels (#1-4). In channel #1, 2.2 mL of the dyed chloroform, water, and the colorless FC-40 were added to the inlet reservoirs of individual devices. For the devices using chloroform and water, which required an extended travel distance, a refill of 300 µL of the flowing fluid was added to the inlet reservoir to minimize the effect of pressure on the fluid dynamics. A refill was not added for FC-40, since data collection stopped after the fluid front reached the first calibration marker. Data were collected for the chloroform and water experiments until the fluid front of each respective device reached the outlet reservoir. For channel #2, 2.2 mL of the dyed 50% (v/v) isopropyl alcohol, nonanol, and pentanol were added to the inlet reservoir of individual devices connected to the cross section corresponding to w = 2 mm and h = 2 mm. Data were collected until the fluid surpassed the first calibration maker. For channel #3, 140 µL of the dyed water was added to the plasma treated device and data were collected until the fluid front reached the outlet reservoir. For channel #4, 170 µL of 50% (v/v) isopropyl alcohol was added to the inlet reservoir and data were collected until the fluid front reached the outlet reservoir. For each fluid in each channel dimension, experiments were completed in triplicate (n = 3).

Videos of the progression of the flow of the solvent in the device were recorded using a Nikon-D5300 ultra-high resolution single lens reflective (SLR) camera at 60 fps. Devices were set atop a white background with a lab jack underneath. An image of the camera and device set-up can be found in **Figure B2**. A video frame was analyzed every 10 frames using an execution file written in Python. The distance that the fluid front had traveled was measured using ImageJ. The scale for each trial was set using the "Set Scale" function and the calibration markers on the device. The fluid front was tracked using the segmented line function and the total travel distance for each frame was measured using the "Measure" function. Data were exported as a .csv file and imported into Microsoft Excel. Calculations for fluid velocity and comparisons to the theoretical model were also conducted in Microsoft Excel.

3.5 References

1. Huh, C.; Scriven, L. E. Hydrodynamic Model of Steady Movement of a Solid/Liquid/Fluid Contact Line. *J. Colloid Interface Sci.* **1971**, *35* (1), 85–101.
2. Dussan, E. B. On the Spreading of Liquids on Solid Surfaces: Static and Dynamic Contact Lines. *Annu. Rev. Fluid Mech.* **1979**, *11*, 371–400.
3. Blake, T. D.; Haynes, J. Contact-Angle Hysteresis. *Prog. Surf. Membr. Sci.* **1973**, *6*, 125–138.
4. Lucas, R. Ueber Das Zeitgesetz Des Kapillaren Aufstiegs von Flüssigkeiten. *Colloid Polym. Sci.* **1918**, *23* (1), 15–22.
5. Washburn, E. W. The Dynamics of Capillary Flow. *Phys. Rev.* **1921**, *17* (3), 273.
6. Rideal, E. K. On the Flow of Liquids under Capillary Pressure. *Philos. Mag. Ser. 6* **1922**, *44* (264), 1152–1159.
7. Cai, J.; Jin, T.; Kou, J.; Zou, S.; Xiao, J.; Meng, Q. Lucas–Washburn Equation-Based Modeling of Capillary-Driven Flow in Porous Systems. *Langmuir* **2021**, *37* (5), 1623–1636.
8. Berli, C. L. A.; Bellino, M. G. Using Mesoporous Thin Films as Nano-Micro-Fluidic Tools. *Capill.* **2022**, *5* (6), 123–127.
9. De Gennes, P. G. Wetting: Statics and Dynamics. *Rev. Mod. Phys.* **1985**, *57* (3), 827–
10. Cox, R. G. The Dynamics of the Spreading of Liquids on a Solid Surface. Part 1. Viscous Flow. *J. Fluid Mech.* **1986**, *168*, 169–194.
11. Voinov, O. V. Hydrodynamics of Wetting. *Fluid Dyn.* **1976**, *11* (5), 714–721.
12. Dussan, E. B. On the Difference between a Bounding Surface and a Material Surface. *J. Fluid Mech.* **1976**, *75* (4), 609–633.

13. Ramé, E.; Garoff, S. Microscopic and Macroscopic Dynamic Interface Shapes and the Interpretation of Dynamic Contact Angles. *J. Colloid Interface Sci.* **1996**, *177* (1), 234–244.
14. Blake, T. D.; Haynes, J. M. Kinetics of Liquid-Liquid Displacement. *J. Colloid Interface Sci.* **1969**, *30* (3), 421–423.
15. Eyring, H. The Activated Complex in Chemical Reactions. *J. Chem. Phys.* **1935**, *3* (2), 107–115.
16. Blake, T. D. The Physics of Moving Wetting Lines. *J. Colloid Interface Sci.* **2006**, *299* (1), 1–13.
17. Duvivier, D.; Blake, T. D.; De Coninck, J. Toward a Predictive Theory of Wetting Dynamics. *Langmuir* **2013**, *29* (32), 10132–10140.
18. Blake, T. D.; De Coninck, J. The Influence of Solid-Liquid Interactions on Dynamic Wetting. *Langmuir* **2002**, *18*, 7971–7976.
19. Martic, G.; Gentner, F.; Seveno, D.; Coulon, D.; De Coninck, J.; Blake, T. D. A Molecular Dynamics Simulation of Capillary Imbibition. *Langmuir* **2002**, *18*, 7971–7976.
20. Isele-Holder, R. E.; Ismail, A. E. Requirements for the Formation and Shape of Microscopic Precursors in Droplet Spreading. *Langmuir* **2016**, *32* (18), 4472–4478.
21. Gennes, P. G.; Brochard-Wyart, F.; Quéré, David. *Capillarity and Wetting Phenomena: Drops, Bubbles, Pearls, Waves*; Springer, 2004.
22. Hamraoui, A.; Thuresson, K.; Nylander, T.; Yaminsky, V. Can a Dynamic Contact Angle Be Understood in Terms of a Friction Coefficient? *J. Colloid Interface Sci.* **2000**, *226* (2), 199–204.
23. Wu, P.; Nikolov, A.; Wasan, D. Capillary Dynamics Driven by Molecular Self-Layering. *Adv. Colloid Interface Sci.* **2017**, *243*, 114–120.
24. Wu, P.; Nikolov, A. D.; Wasan, D. T. Capillary Rise: Validity of the Dynamic Contact Angle Models. *Langmuir* **2017**, *33*, 7862–7872.
25. Hoffman, R. L. A Study of the Advancing Interface. I. Interface Shape in Liquid—Gas Systems. *J. Colloid Interface Sci.* **1975**, *50* (2), 228–241.
26. Tanner, L. H. The Spreading of Silicone Oil Drops on Horizontal Surfaces. *J. Phys. D: Appl. Phys.* **1979**, *12* (9), 1473–1484.
27. Jiang, T. S.; Soo-Gun, O. H.; Slattery, J. C. Correlation for Dynamic Contact Angle. *J. Colloid Interface Sci.* **1979**, *69* (1), 74–77.
28. Bracke, M.; Voeght, F.; Joos, P. The Kinetics of Wetting: The Dynamic Contact Angle. *Prog. Coll. Polym. Sci.* **1989**, *79*, 142–149.
29. Joos, P.; Van Remoortere, P.; Bracke, M. The Kinetics of Wetting in a Capillary. *J. Colloid Interface Sci.* **1990**, *136* (1), 189–197.
30. Seebergh, J. E.; Berg, J. C. Dynamic Wetting in the Low Capillary Number Regime. *Chem. Eng. Sci.* **1992**, *47* (17–18), 4455–4464.
31. Casavant, B. P.; Berthier, E.; Theberge, A. B.; Berthier, J.; Montanez-Sauri, S. I.; Bischel, L. L.; Brakke, K.; Hedman, C. J.; Bushman, W.; Keller, N. P.; Beebe, D. J. Suspended Microfluidics. *Proc. Natl. Acad. Sci. U.S.A.* **2013**, *110* (25), 10111–10116.
32. Berthier, J.; Gosselin, D.; Berthier, E. A Generalization of the Lucas–Washburn–Rideal Law to Composite Microchannels of Arbitrary Cross Section. *Microfluid. Nanofluid.* **2015**, *19* (3), 497–507.
33. Berthier, J.; Brakke, K. A.; Berthier, E. *Open-Microfluidics*; Scrivener-Wiley Publishing, 2016.
34. Berthier, E.; Dostie, A. M.; Lee, U. N.; Berthier, J.; Theberge, A. B. Open Microfluidic Capillary Systems. *Anal. Chem.* **2019**, *91*, 8739–8750.
35. Oliveira, N. M.; Vilabril, S.; Oliveira, M. B.; Reis, R. L.; Mano, J. F. Recent Advances on Open Fluidic Systems for Biomedical Applications: A Review. *Mater. Sci. Eng. C.* **2018**, *C 97*, 851–863.

36. Lee, B.; Kim, S.; Ko, J.; Lee, S. R.; Kim, Y.; Park, S.; Kim, J.; Hyung, S.; Kim, H. Y.; Jeon, N. L. 3D Micromesh-Based Hybrid Bioprinting: Multidimensional Liquid Patterning for 3D Microtissue Engineering. *NPG Asia Mater.* **2022**, *14* (1), 6–16.
37. Weislogel, M. M.; Graf, J. C.; Wollman, A. P.; Turner, C. C.; Cardin, K. J. T.; Torres, L. J.; Goodman, J. E.; Buchli, J. C. How Advances in Low-g Plumbing Enable Space Exploration. *NPJ Microgravity* **2022**, *8* (1), 16.
38. Concus, P.; Finn, R. On the Behavior of a Capillary Surface in a Wedge. *Proc. Natl. Acad. Sci. U.S.A.* **1969**, *63* (2), 292–299.
39. Berthier, J.; Theberge, A. B.; Berthier, E. *Open-Channel Microfluidics*; IOP Publishing, 2019.
40. Ouali, F. F.; McHale, G.; Javed, H.; Trabi, C.; Shirtcliffe, N. J.; Newton, M. I. Wetting Considerations in Capillary Rise and Imbibition in Closed Square Tubes and Open Rectangular Cross-Section Channels. *Microfluid. Nanofluid.* **2013**, *15* (3), 309–326.
41. Baret, J.-C.; Decré, M. M. J.; Herminghaus, S.; Seemann, R. Transport Dynamics in Open Microfluidic Grooves. *Langmuir* **2007**, *23* (9), 5200–5204.
42. Lade, R. K.; Hippchen, E. J.; Macosko, C. W.; Francis, L. F. Dynamics of Capillary-Driven Flow in 3D Printed Open Microchannels. *Langmuir* **2017**, *33* (12), 2949–2964.
43. Kolliopoulos, P.; Jochem, K. S.; Lade, R. K.; Francis, L. F.; Kumar, S. Capillary Flow with Evaporation in Open Rectangular Microchannels. *Langmuir* **2019**, *35* (24), 8131–8143.
44. Kolliopoulos, P.; Jochem, K. S.; Johnson, D.; Suszynski, W. J.; Francis, L. F.; Kumar, S. Capillary-Flow Dynamics in Open Rectangular Microchannels. *J Fluid Mech.* **2021**, *911*, A32.
45. Bamorovat Abadi, G.; Bahrami, M. The Effect of Surface Roughness on Capillary Rise in Micro-Grooves. *Sci. Rep.* **2022**, *12* (1), 14867.
46. Gloss, D.; Herwig, H. Wall Roughness Effects in Laminar Flows: An Often Ignored Though Significant Issue. *Exp. Fluids* **2012**, *49* (2), 461–470.
47. Vesel, A.; Mozetic, M. Surface Modification and Ageing of PMMA Polymer by Oxygen Plasma Treatment. *Vacuum* **2012**, *86*, 634–637.
48. Sikora, A.; Czylkowski, D.; Hrycak, B.; Moczała-Dusanowska, M.; Łapiński, M.; Dors, M.; Jasiński, M. Surface Modification of PMMA Polymer and Its Composites with PC61BM Fullerene Derivative Using an Atmospheric Pressure Microwave Argon Plasma Sheet. *Sci. Rep.* **2021**, *11* (1), 9270.
49. Kim, S.; Thiessen, P. A.; Bolton, E. E.; Chen, J.; Fu, G.; Gindulyte, A.; Han, L.; He, J.; He, S.; Shoemaker, B. A.; Wang, J.; Yu, B.; Zhang, J.; Bryant, S. H. PubChem Substance and Compound Databases. *Nucleic Acids Res.* **2016**, *44* (Database issue), D1202.
50. Mohammad, A. A.; Alkhaldi, K. H. A. E.; Altuwaim, M. S.; Al-Jimaz, A. S. Effect of Temperature and Chain Length on the Viscosity and Surface Tension of Binary Systems of N,N-Dimethylformamide with 1-Octanol, 1-Nonanol and 1-Decanol. *J. Chem. Thermodyn.* **2014**, *74*, 7–15.
51. Lee, J. J.; Berthier, J.; Theberge, A. B.; Berthier, E. Capillary Flow in Open Microgrooves: Bifurcations and Networks. *Langmuir* **2019**, *35* (32), 10667–10675.
52. Berthier, J.; Brakke, K. A.; Berthier, E. A General Condition for Spontaneous Capillary Flow in Uniform Cross-Section Microchannels. *Microfluid. Nanofluid.* **2014**, *16* (4), 779–785.
53. Chang, L.-H.; Kumar, S. Capillary Filling in Open Rectangular Microchannels with a Spatially Varying Contact Angle. *Langmuir* **2023**, *39* (50), 18526–18536.
54. MATLAB. No Title.
55. Quéré, D. Inertial Capillarity. *EPL* **1997**, *39* (5), 533–538.
56. Li, H.; Sedev, R.; Ralston, J. Dynamic Wetting of a Fluoropolymer Surface by Ionic Liquids. *Phys. Chem. Chem. Phys.* **2011**, *13*, 3952–3959.

Chapter 4 | The Dynamics of Capillary Flow in an Open-Channel System Featuring Trigger Valves

Reproduced in part from ***Tokihiro, J.C.;*** *Robertson, I.H.; Gregucci, D.; Shin, A.; Michelini, E.; Nicholson, T.M.; Olanrewaju, A.; Theberge, A.B.;[#] Berthier, J.;[#] Berthier, E. [#] The dynamics of capillary flow in an open-system featuring trigger valves. Scientific Reports,* ***2024****, 14, 31732.*
[#]Co-corresponding authors

Please refer to journal site for supplementary materials referenced in this chapter: doi.org/10.1038/s41598-024-82329-3

JCT, IHR, and DG designed the devices. JCT, IHR, DG, and AS conducted the experiments. JCT and IHR analyzed the video frames from the flow experiments. JCT, IHR, DG, and AS fabricated the devices. JB developed and applied the theoretical model and MATLAB code. JCT, IHR, DG, TMN, AO, ABT, JB, and EB designed the study, interpreted the results, and conceptualized ideas. EM, TMN, ABT, and JB supervised the work. JCT, IHR, DG, ABT, and JB wrote the manuscript with all authors revising.

Abstract: Trigger valves are fundamental features in capillary-driven microfluidic systems that stop fluid at an abrupt geometric expansion and release fluid when there is flow in an orthogonal channel connected to the valve. The concept was originally demonstrated in closed-channel capillary circuits. We show here that trigger valves can be successfully implemented in open channels. We also show that a series of open-channel trigger valves can be placed alongside or opposite a main channel resulting in a layered capillary flow. We developed a closed form model for the dynamics of the flow at trigger valves based on the concept of average friction length and successfully validated the model against experiments. For the main channel, we discuss layered flow behavior in the light of the Taylor-Aris dispersion theory and in the channel turns by considering Dean theory of mixing. This work has potential applications in autonomous microfluidics systems for biosensing, at-home or point-of-care sample preparation devices, hydrogel patterning for 3D cell culture and organ-on-a-chip models.

4.1 Introduction

Microfluidic devices precisely move fluids through small channels and can use surface tension effects (capillary forces) defined by channel geometry and surface chemistry to achieve self-powered and self-regulated operation. Capillary microfluidics is driven through spontaneous capillary flow (SCF)[1–7] and can perform timed multi-step processes by leveraging capillary forces encoded in device architecture without the need for external triggers (e.g., pushing a button, programming an electrical signal, or other user activity).[8–11] Trigger valves (TGVs) are one of the main geometric features/control elements that make autonomous capillary-driven fluid addition possible. TGVs are modified passive stop valves that release a confined liquid upon the capillary-driven flow of another or a similar liquid in an orthogonal channel to the stop valve (**Figure 1A**). These valves are widely used in a variety of closed-channel point-of-care diagnostic applications such as immunoassays for bacterial, antibody, and protein detection antibody or protein detection as well as live-cell staining.[12–15] There is a wealth of theoretical, experimental, and applied work using closed-channel TGVs.[12–24] While the concept of using TGV in open microfluidic systems have been introduced in brief, [19,25,26] there is a need for more in-depth theoretical development and experimental validation.

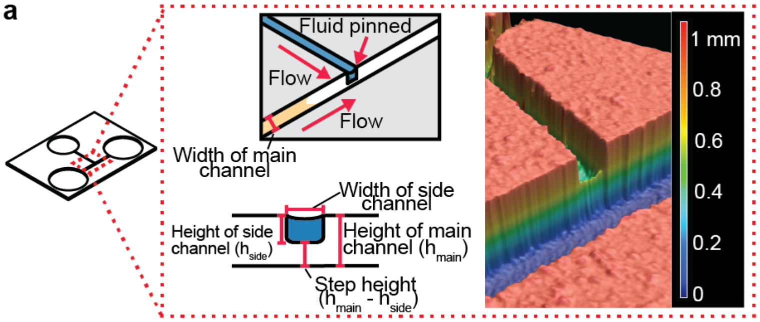

Design considerations for open trigger valve devices

- Contact angle and channel dimensions allow SCF
- Step and perpendicular side channel are required for fluid pinning
- Incubation time is determined by travel distance after trigger valve

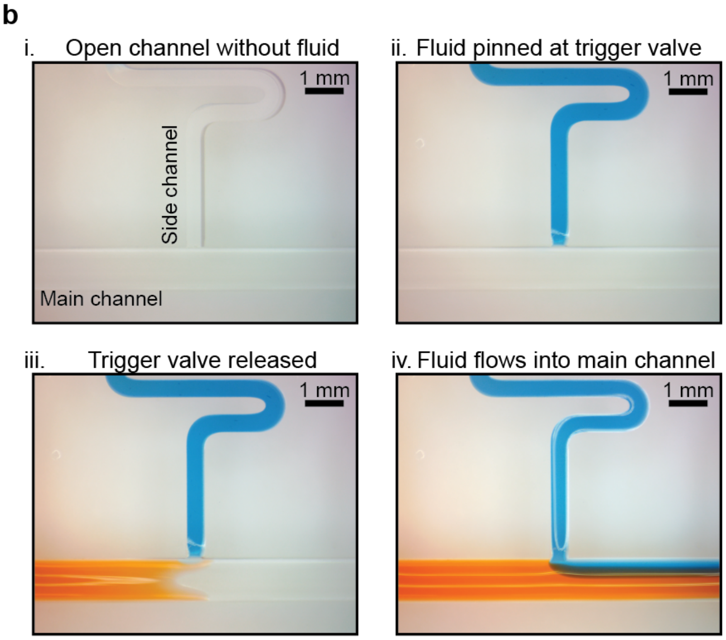

i. Open channel without fluid

ii. Fluid pinned at trigger valve

iii. Trigger valve released

iv. Fluid flows into main channel

Figure 4.1. *Considerations and operation of trigger valving in open channels.* (**a**) Open-channel device with one TGV highlighting the intersection of the main channel and side channel and key aspects of TGV devices. (Inset) Drawings of the side channel opening indicating where pinning occurs (upper left panel) and a view of the trigger valve gate with the step from the bottom of the main channel to the bottom of the side channel (lower left panel)—a critical feature preventing flow into the empty main channel. Accompanying Keyence profilometer photo of an example open TGV (right panel). (**b**) A series of images illustrating TGV release in open channels starting with an empty main and side channel (**bi**) with the same channel dimensions as the sketch in i and ii. (**bii**) After liquid is added to the side channel, the fluid pins at the edge of the opening to the main channel where it remains stationary. (**biii**) When the main channel fluid makes contact with the pinned fluid, the side channel liquid is de-pinned. (**biv**) Fluids from main channel and side channel flows then stabilize over time.

Open microfluidics has been used for many applications in organ-on-a-chip models, space science, neuronal networks, and cancer research.[27–30] Open microfluidics leverages one or more air-liquid interfaces through the removal of one or more channel walls to enable improved accessibility of the channels. The popularity of open microfluidics is linked to several advantages such as accessibility, low cost, easy fabrication, and easy surface treatment.[1,4–7] Through the removal of a channel wall, open channels afford the ability to add fluids at any point in a channel. Adding TGVs to open channels now add a layer of flexibility to autonomously introduce another flow of fluids to a channel – which opens the possibilities for hybrid open/closed devices. Many channel geometries, architectures, and valves reported in closed microfluidics may be applied to open microfluidic configurations to increase their capabilities and range of applications.

Drawing on prior work in closed-channel systems, we consider here the so-called two-layer or “stair-step” TGVs that have a higher stability than one-level valves due to the two-dimensional geometric expansion conferred by the separation of the main and side channels, which prevents leakage of pinned fluid (**Figure 4.1a**).[9,19,24] In capillary-driven devices, the flow is regulated by surface energies and geometric features. Passive valves, which include TGVs, based on geometrical pinning are a common method for fine control of flow and on-chip programming. Geometrically, pinning occurs when capillary pressure is lost due to a sudden change in the channel architecture (such as an enlargement). Pinning of the fluid at the TGV “gate” is important to ensure that the fluid stops flowing until the depinning by a perpendicular flow by a miscible fluid. Retention of the liquid in the side channel until the main flow reaches the TGV relies on the liquid being pinned at the gate (or aperture), which refers to the edges of the side channel that intersects with the main channel (**Figure 4.1b**). Pinning of a liquid on edges depends on the edge angle and on the liquid-solid contact angle.[31–34] If the constraints on the liquid (e.g., pressure) exceed the pinning angle threshold, pinning does not occur. Otherwise, pinning is stable, allowing us to leverage this phenomenon to create TGVs in open configurations.

In this work, we show that TGVs can be positioned in series in open-channel geometries through the de-pinning of multiple channels with immobilized fluids and that we can leverage characteristic features to design an open-TGV device. We also investigate the dynamics of flow and present an analytical model describing the travel distances and flow velocities based on the concept of friction length[3] with a comparison to experimental results. Sequential de-pinning of trigger valves results in layered co-flows when the different liquids are miscible or have a very small liquid-liquid surface tension, enabling autonomous controlled fluid addition. The use of trigger valves was also used to demonstrate applicability through the detection of nitrites in water and meat samples.

4.2 Results and Discussion

We present an analytical model of TGVs in open capillary channel configurations – a new tool for the open microfluidics tool kit. While the concept of open TGVs have been introduced in brief[26], to our knowledge, this is the first in-depth development of theory complemented with a comparison to in-lab experiments. Throughout our study, three important characteristic aspects of the open TGVs were investigated: programmed TGV release, fluid velocity, and fluid layering.

4.2.1 Model

A sketch of an open capillary device with TGVs on the same side or opposite side of the main channel is shown in **Figure 4.2a** and **b**, respectively. Side channels are filled with immobile liquids (blue, yellow and purple). The “main” or “primary” fluid flows due to capillarity and sequentially opens the different gates, i.e., de-pins the immobilized side liquids which start co-flowing in the main channel. The side channels can be placed on the same side of the main channel (**Figure 4.2a**) or in a staggered arrangement (**Figure 4.2b**).

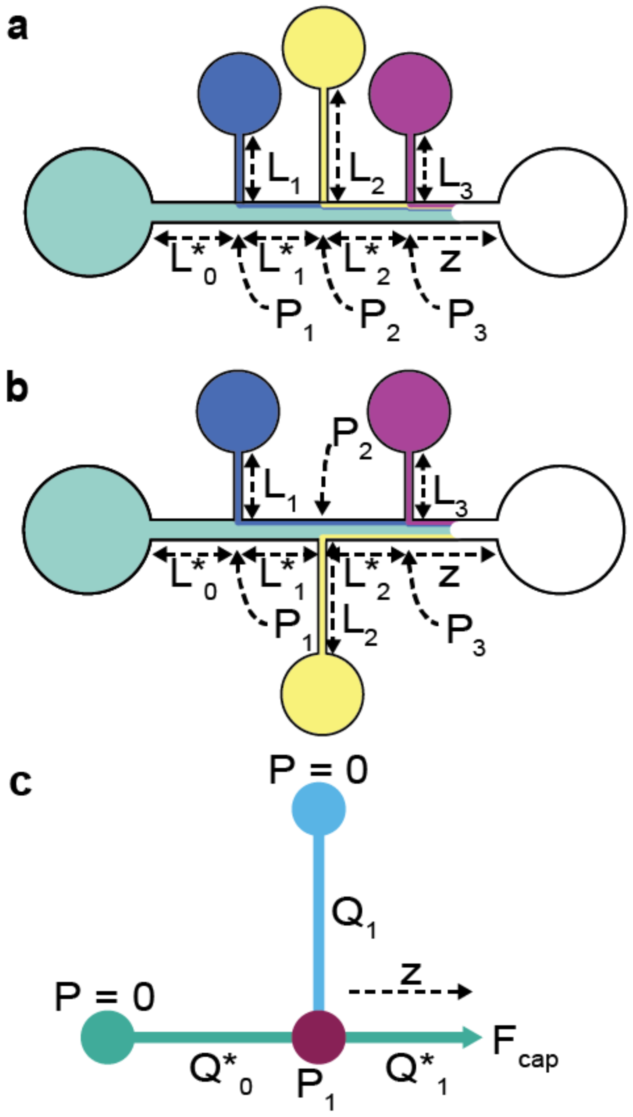

Figure 4.2. Sketch of the device with the three TGVs, placed on the same side (**a**) or on opposite sides (**b**), in the notations, a star denotes the main channel. (**c**): schematic of the flow at a node (intersection of the TGV and main channel) used for the calculation. The letter *Q* corresponds to a volumetric flow rate, and *P* to a pressure.

Figure 4.2c shows the principle of the calculation of the travel distance of the front meniscus (z) as a function of time after the front meniscus has passed a TGV. The flow is actuated by the capillary pressure at the front meniscus and balanced by the friction on the different wetted walls. In the inlet channel (before the first TGV),—and referenced by the index 0 in the calculation—the travel distance is determined by the generalized LWR (Lucas-Washburn-Rideal) law.[35] Table 1 details symbols with their corresponding units.

Table 4.1. Notations.

Name	notation	unit	Remarks/References
Length of channel	L_i	mm	Lengths of side channels
Length of main channel sections	L^*_i	mm	Lengths between two nodes (TGVs)
Cross-sectional area	S	mm^2	Different for main and side channels
Average friction length	$\bar{\lambda}_i$	mm	Characteristic of friction[35]
Perimeter (total)	p_i	mm	Includes free perimeter
Perimeter (wetted)	$p_{W,i}$	mm	Only wetted part
Perimeter (free)	$p_{F,i}$	mm	Perimeter of free surface (in a cross-section)
Viscosity (dynamic)	μ	mPa.s	Nonanol
Surface tension	γ	mN/m	Nonanol
Contact angle	θ	degrees	Static contact angle
Generalized Cassie angle	θ^*_i	degrees	Generalized Cassie angle for open channels
Contact angle	θ_d	degrees	Dynamic contact angle
Pressure	P	mPa	Pressure at the nodes
Capillary pressure	P_{cap}	mPa	Laplace pressure of the meniscus
Flow rate	Q	mm^3/s	volumetric flow rate
Velocity	V	mm/s	Averaged in a cross section (side channels)
Velocity	V^*	mm/s	Averaged in a cross section (main channel)
Travel distance	z	mm	Middle of advancing meniscus
Geometrical coefficient	A_i	mm^3	Side channel
Geometrical coefficient	A^*	mm^3	Main channel
Auxiliary geometrical coefficient	B_i	mm^3	Node coefficients
Time	t	s	

$$z_0(t) = \sqrt{\frac{\gamma}{\mu} 2\bar{\lambda}_0 \cos\theta_0^*\ t}. \tag{1}$$

If necessary, relation (1) can be modified by a dynamic contact angle.[35,36] The algebraic developments for the determination of flow past the TGVs are lengthy and are detailed in **Appendix Section C1**. We only present here the principle behind the model (**Figure 4.2c**). Let us introduce the geometric coefficients $A_i = \frac{\bar{\lambda}_i S_i^2}{L_i\, p_i}$ and $A_i^* = \frac{\bar{\lambda}_i^* S_i^{*2}}{L_i^*\, p_i}$ where the star (*) denotes the main channel and *i* is the channel index (**Figure 2a**). These coefficients have the dimension of volume (mm^3) and solely depend on the width, depth, and length of each channel. The principle of the calculation can be easily shown considering the first TGV. The pressure at node 1, P_1, is expressed by the two relations

$$P_1 = \frac{L_1\, p_1}{S_1}\, \mu \frac{V_1}{\bar{\lambda}_1} = \mu \frac{Q_1}{A_1} = \mu \frac{Q_0^*}{A_0^*}, \tag{2}$$

this can be combined with the mass conservation relation $Q_1^* = Q_0^* + Q_1$ to produce the relation between the pressure at the node and the meniscus velocity ($V_1^* = Q_1^*/S_1^*$):

$$P_1 = \mu \frac{S_1^*\, V_1^*}{A_1 + A_0^*}. \tag{3}$$

In the viscous regime, the capillary force balances the wall friction which, in terms of pressure, yields the relation

$$P_{cap} = \frac{\gamma\, p_1^* \cos\theta_1^*}{S_1^*} = \frac{z}{L_1^*} \mu\, \frac{S_1^* V_1^*}{A_1^*} + P_1. \tag{4}$$

Using $V_1^* = dz/dt$ and combining (3) and (4) yields the solution,

$$z = -\frac{L_1^* A_1^*}{(A_1 + A_0^*)} + \sqrt{\left[\frac{L_1^* A_1^*}{(A_1 + A_0^*)}\right]^2 + z_1^2}\ , \tag{5}$$

where z_1 is the travel distance corresponding to the LWR law in the main channel, and $z_1(\tau) = \sqrt{\frac{\gamma}{\mu} 2\bar{\lambda}_0 \cos\theta_0^*\ \tau}$, where z_1 and τ are the distance and time starting from node 1. The principle can be extended by recurrence to an arbitrary number of TGVs as the side liquids are identical with the only difference being the slight changes from added coloring—and co-flow as a unique liquid downstream each trigger valve (see **Appendix Section C1**). We then obtain

$$z = -\frac{L_n^* A_n^*}{(A_n + B_{n-1})} + \sqrt{\left[\frac{L_n^* A_n^*}{(A_n + B_{n-1})}\right]^2 + z_n^2}, \tag{6}$$

where the B_i are a mathematical sequence including all preceding A_i^* and A_i.

4.2.2 Programmed trigger valve release allows for tunable timing between fluidic events

We investigated how to achieve tunable timing between fluid events by using defined distances between TGVs. Towards this goal, we used the analytical model from Section 4.2.1 and validated the results through in-lab experiments (**Figure 4.3**). We designed two channels fabricated in poly(methyl)methacrylate (PMMA) with three TGVs (cross-section dimensions of w = 400 mm and h = 600 mm) oriented along the main channel (cross-section dimensions of w = 1 mm and h = 1 mm). The TGVs in Devices 1 and 2 were separated by travel distances of 15 and 30 mm, respectively. Nonanol was chosen as the main and side channel fluid with slight differences in coloring to visualize the flow, but constant viscosity. To ensure sustained fluid pumping, a paper pad was added to the end of the main channel. For Device 1, the time between the release of TGV one and two was 3.70 (±0.05) seconds and the time between TGV release of two and three was 3.93 (±0.06) seconds. For Device 2, the time between TGV release increased with the longer channel length to 7.67 (± 0.10) and 9.83 (±0.20), respectively. (**Figure 4.3a and b**, designs in **Figure C6**). Data reported are the average of three trials with the standard deviation. Data for all trials can be found in **Figure C8**. Comparison of the experimental data to the theoretical model for fluid front travel distance and velocity, correspond closely to each other, validating that our model predicts fluid flow in open channels with integrated TGVs.

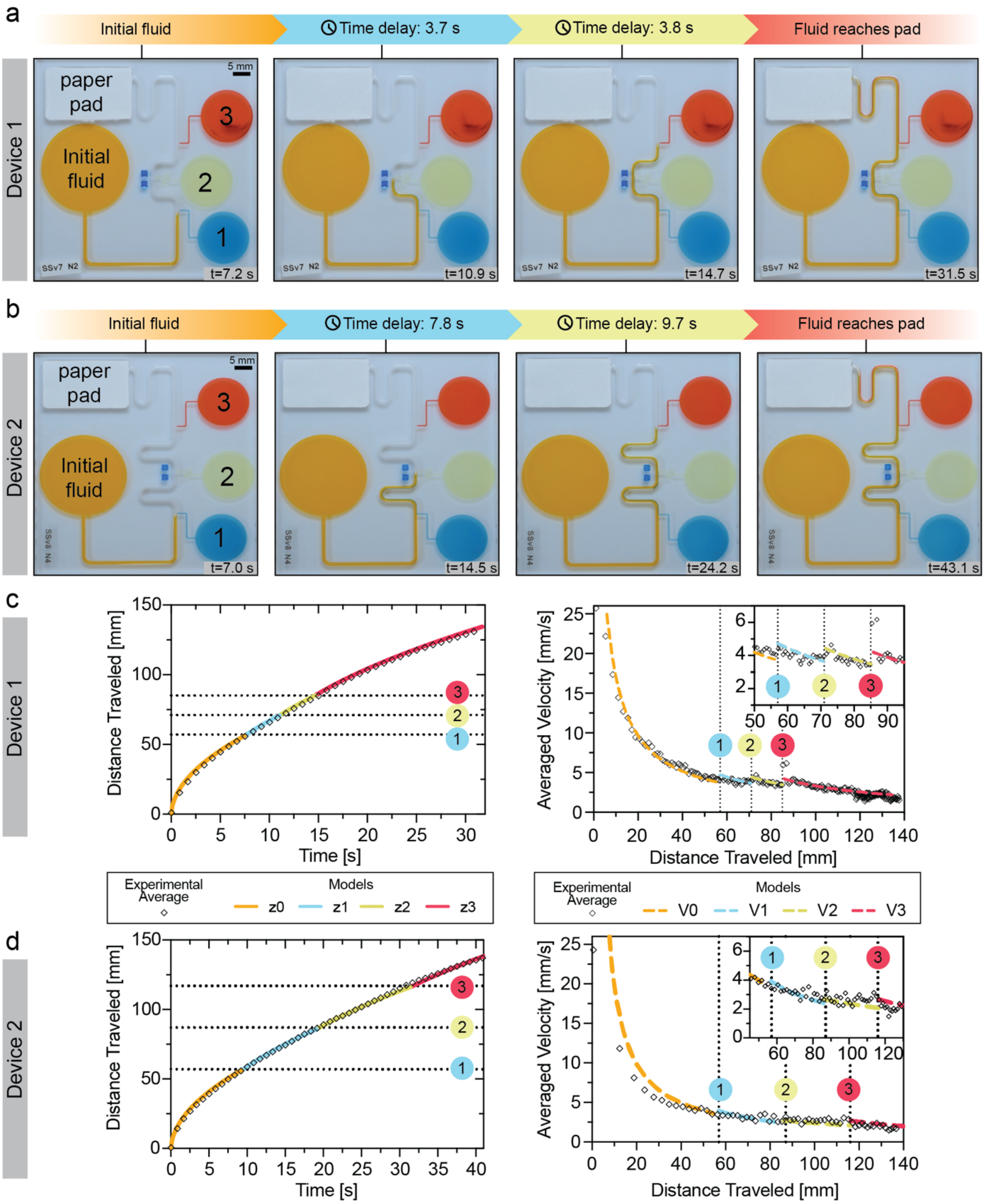

Figure 4.3. *Distance between TGVs provides timed control of fluid release.* Progression of flow in devices with parallel TGVs spaced approximately 15 mm (a, device 1) and 30 mm (**b**, device 2) apart. Comparison of model (solid line) with experimental fluid front travel distance (diamonds) at the meniscus over time for device 1 (**c**, left) and 2 (**d**, left). Experimental data was averaged for three trials (n=3). Model is presented in segments corresponding to the calculated travel distances prior to the TGV release (orange, z0), between the first and second TGV (blue, z1), between the

second the third valves (yellow, z2) and between the third valve and the paper pad (red, z3). Experimental velocities (diamonds) were calculated from the travel distance and fluid velocities of each channel were calculated from the travel distance progression and are compared against the calculated model velocities (dashed line) using a dynamic contact angle model (V0, orange) for the inlet. Model is shown at the first (blue, V1), second (yellow, V2), and third (red, V3) valves due to the increase in velocity upon TGV release. Data is averaged from three (n=3) trials. Raw data can be found in **Figure C8**.

Like closed channels, implementing TGVs in open-channels is important for on-chip control of fluid addition and programming of timed incubations, waiting periods, or wash steps for the application of this tool in assays, workflows, and reactions such as antibody patterning, polymerase chain reactions (PCR) or enzyme-linked immunosorbent assays (ELISA). Channel geometries and side channel flow rates can be designed to control how much fluid is added to the channel to achieve a certain final concentration or add a set amount of fluid into the flow. Moreover, the ability to implement this method of fluid addition in open channels could enable the automation of fluid addition by controlling when a fluid or reagent is added and the speed/flow rate at which the fluid is introduced, thus reducing the need for additional manual pipetting.

4.2.3 Investigation of dynamics in open trigger valves

We further investigated the effect of TGV release on the main channel fluid dynamics. For this study, we used parallel TGVs spaced 3.70 mm apart (Images of flow progression can be found in **Figure 4.4a**). Using nonanol, we measured the travel distance over time (**Figure 4.4e** and **f**) and noted the spatial locations of the TGVs (black dotted lines). Upon closer inspection of the TGV region of the graphs (**Figure 4c**, inset), the model predicts a stair-like trend where the TGVs cause an increase in fluid velocity. Shortening the distances between the valves makes this trend more evident (**Figure 4c** and **d**). The release of a TGV increases the flow velocity where the side channel acts as an additional reservoir closer to the front meniscus than the inlet reservoir on the main channel. Therefore, the velocity increases in the main channel at the opening of the TGV. Notably, the experimental data shows correlation with these predicted jumps. A comparison of experimental results to the theory for TGVs on opposing sides can be found in **Figure C9** and raw data for valves on the same side and on opposite sides can be found in **Figure C10**. Further, an investigation of an increased travel distance between the last trigger valve and the paper pad showed the model is valid for even longer channel lengths (**Figure C11**).

In a comprehensive view, the release of the fluid at a TGV increases the velocity of the main channel in the geometrical configuration of the present device; however, in reality, this effect is more complex. The lengths and widths of the side channels as well as the distances between the valves are determining parameters for the velocity jump in the main channel at a TGV (these dimensions are included in the constants B_i and A_i of the model). More specifically, the wall friction in the side channels conditions the velocity jump. A detailed analysis is done in **Appendix Section C2**. Briefly, there is a positive velocity jump at a TGV, and this jump is higher when the friction in the side channel is less. Thus, when we consider this in an applications view, the lengths of the side channels, distances between the side channels, and the cross-section dimensions are critical aspects to take into consideration. In cases where specific conditions need to be met, the presented model allows users to predict the fluid velocities and flow rates of the side channel pumping which can inform users in determining optimal dimensions.

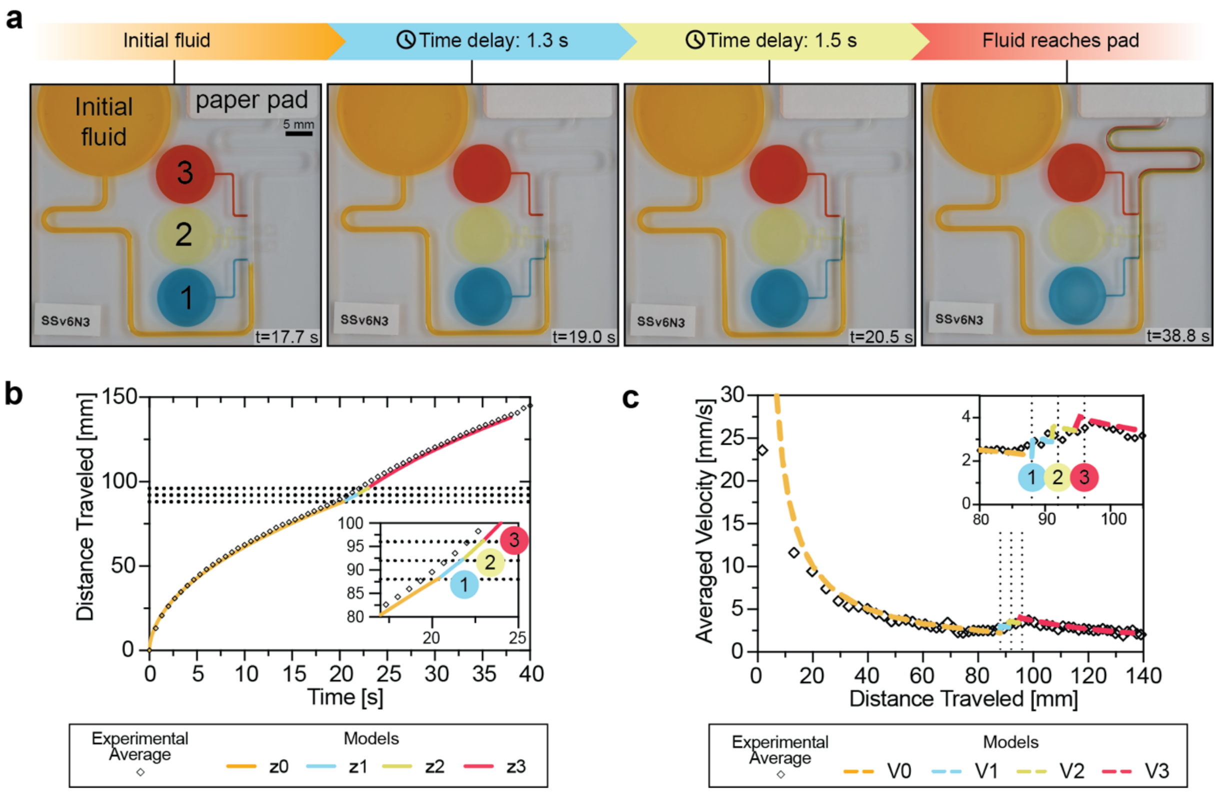

Figure 4.4. *Open channel flow experiments show an increase in velocity after each valve opening.* Progression of fluid flow through device with shorter distances between TGVs (**a**). Comparison of the theoretical model (solid line) with experimental fluid front travel distance at the meniscus (diamonds) for devices with three side channels in parallel. Experimental data were averaged for four trials (n=4). Model is presented in segments corresponding to the calculated travel distances prior to the TGV release (orange, z0), between the first and second TGV (blue, z1), between the second the third valves (yellow, z2) and between the third valve and the paper pad (red, z3). (**b**) Fluid velocities were calculated from the travel distance and the experimental data (diamonds) compared against the calculated model (dashed line) velocities using a dynamic contact angle model (orange, V0) for the inlet. Model is shown at the first (blue, V1), second (yellow, V2), and third (red, V3) valves due to the increase in velocity upon TGV release. Raw data can be found in **Figure C10**.

4.2.4 Trigger valves enable layering in open systems

We investigated the co-flowing of fluids after the release of each TGV. With the pinning of each fluid at the gate and the subsequent release by the main channel fluid, each valve demonstrates a “burst” phase into the main channel where the fluid starts flowing into the channel. The thickness of the layer is initially large, but stabilizes over time. Using dyed nonanol and devices with parallel TGVs (**Figure 4.4**), layer width measurements were taken at 0.5 mm after the valve in the main fluid channel for each of the valves, monitoring only the topmost fluid layer. The measurements were taken until the fluid exited the frame. **Figure 4.5** shows the layering and a comparison of the layer thicknesses over time and a side view image of the fluid layers for trigger valves on the same side of the main channel. Layer thickness comparison for valves on opposing sides of the main channel can be found in **Figure C13**.

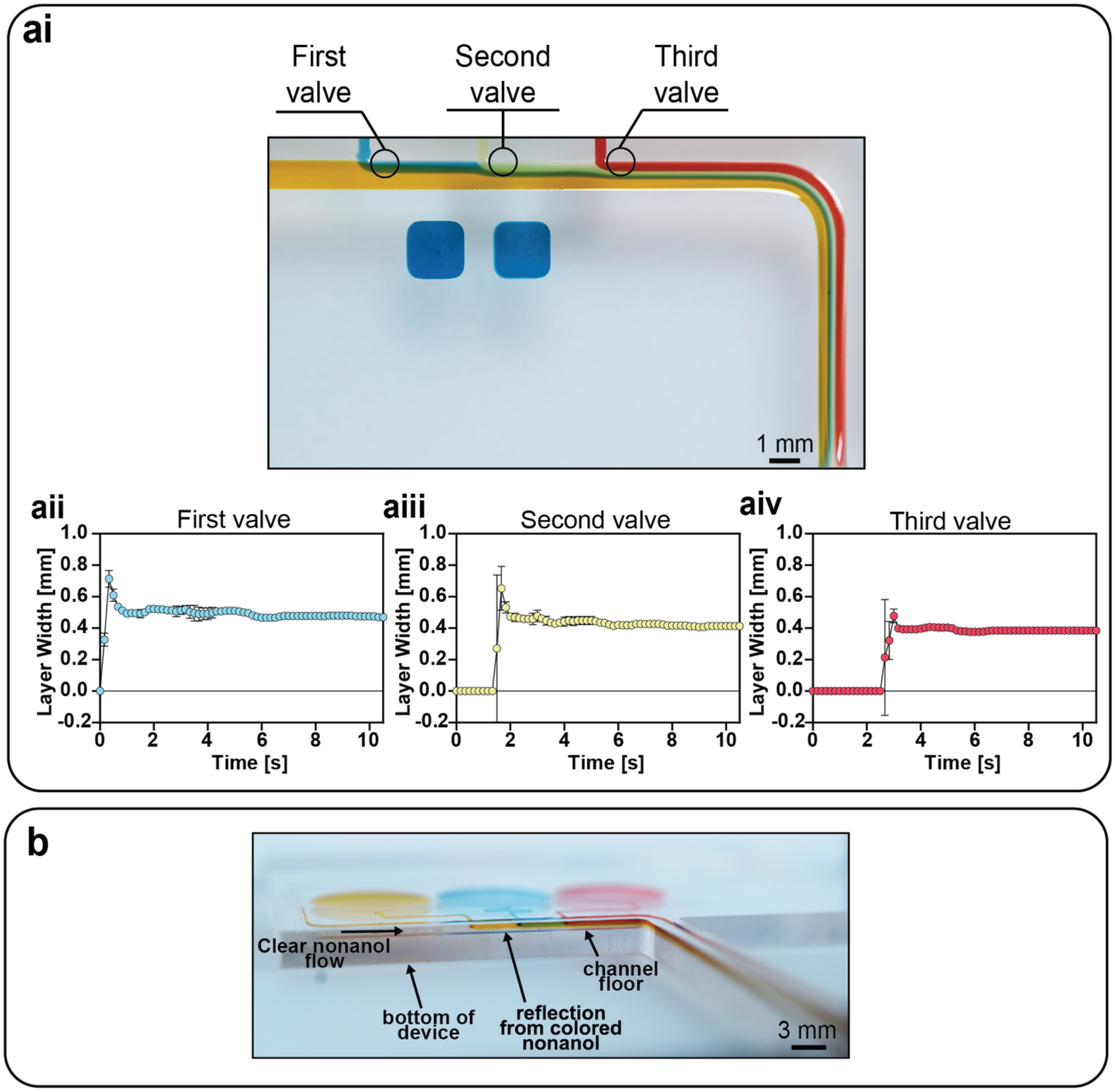

Figure 4.5. *Fluid layers released by the TGVs stabilize in width over time.* (**ai**) Image of the fluid layers in a parallel configuration. Circles indicate where layer thickness measurements were taken for each layer (0.5 mm after each valve). Plots of the measured layer widths over time for the

parallel channel configuration after the first (**aii**), second (**aiii**), and third (**aiv**) valves. Data are shown as an average of three replicates (n = 3) with error bars indicating standard deviation. Layer widths are reported at a defined point in the channel (see diagram in **Figure C14**). (**b**) A side view image of the fluid layering after all three valves were released by undyed (clear) nonanol. Order of colored nonanol used in the side channels for part b were adjusted for visualization of the layers and are not the same as in part a.

After each TGV release, we observed an increase in layer width at the initial opening and then a stabilization of the fluid layers over time with uniform layering of the topmost layers. Moreover, the fluid layers become a cascade of layer thickness with the succession of TGV opening in series where the topmost layer (layer closest to the channel wall) is wide and previously released layers become thinner (**Figure 4.5aii-aiv**). The decrease in width is observed to be due to the previous layers shifting downwards into the main channel and the most recently released layer on top demonstrating an observed 3D effect–a complex phenomenon for the work of a future study. Despite this effect and the initial burst at the gate, layering is uniform between each valve as seen in the **Figure 4.5ai** to **aiv** and we have maintained separation of the layers through 30 mm after all the TGVs are released with the continued capillary pumping by the paper pad. Additional layering data for opposite-facing trigger valves can be found in **Figure C13**. A diagram of the location of measurement with respect to each valve can be found in **Figure C14**. True layering measurements in 2D and 3D and a detailed study of the underlying fundamental fluid dynamics are focal points for future work.

Understanding the effect of fluid layering is an interesting aspect of fundamental open microfluidics. Layering or laminar co-flows are important in the applications of TGVs to create functional devices as this can be used to create a liquid-liquid interface for chemical reactions or on-chip patterning of hydrogels and antibodies. Comparatively, in closed channels, similar flows have been achieved; however, our system enables access to the channel contents for manipulation or interaction with the flows if needed for a specific application. Open-channel devices are also well suited for studies of the mixing of the channel contents, although fluid mixing is not demonstrated here as shown in **Figure 4.5a**.

Table 4.2. Notations.

Name	Notation	Unit	Remarks/References
Time	t	s	
Mixing length	L	mm	Length where noticeable mixing occurs
Hydraulic radius	R_H	mm	
Peclet number	Pe	Non-dimensional	
Viscosity	V	Pa.s	Fluid's resistance to flow
Molecular diffusion coefficient	D	m^2/s	
Boltzmann constant	k_B	J/K	
Temperature	T	K	Kelvin
Molecular radius	R	pm	
Reynold's number	Re	Non-dimensional	
Dean number	De	Non-dimensional	

The reason for this absence of mixing stems from the smallness of the molecular diffusion compared to the axial convection. Symbols with the corresponding definition and units are presented in **Table 4.2**. The Taylor-Aris dispersion theory compares the axial convection time scale $t_{conv} \sim L/V$ to the radial diffusion time $t_{diff} \sim \delta^2/D$. Because the diffusion coefficient *D* in liquids is small, t_{diff} is large and the length where the two characteristic times balances L is given by[37,38]

$$L \cong \frac{\delta^2 \, V}{D} = \delta \, Pe, \qquad (7)$$

where δ is a typical dimension of the fluid layer (the width in our case), *V* is the liquid velocity, *D* is the molecular diffusion coefficient and *Pe* is the Peclet number ($Pe = \delta V/D$). The diffusion coefficient of nonanol can be approximated by the Stokes–Einstein–Sutherland equation, for diffusion of spherical particles through a liquid with low Reynolds number

$$D \cong \frac{k_B \, T}{6 \, \pi \, \mu \, r_m}, \qquad (8)$$

where r_m is the molecular radius, T is the temperature and K_B is the Boltzmann constant. Per literature[36], the nonanol radius was found to be of the order of 0.4 nm and the constant $k_B\,T$ is approximately 4.11 pN.nm at room temperature. Using the value of 0.011 Pa.s for the viscosity of nonanol, we obtain $D\sim 4\ 10^{-11}$ m^2/s. If we consider a liquid "filament" or "layer" coflowing with the carrier flow, with a typical width of 200 μm, the Taylor-Aris diffusion length is of the order of $L\sim$ 50 –100 cm for a velocity on the order of 1 – 2mm/s. In this case, the molecular diffusion does not play an important role in the flow downstream of the TGVs along a length of 20 – 50 cm. The convective velocity V of 1 mm/s is much larger than the radial propagation D/δ of 0.25 μm/s: considering a duration of 50 seconds, molecules in the layer have moved by 50 mm in the axial direction while the radial diffusion is only 12.5 μm.

However, the situation would be different when using different liquids and/or narrower channels. For example, the coefficient of diffusion of water is fifteen times higher than nonanol ($D\sim 10^{-9}$ m^2/s) and even if the velocity of the flow is twice that of nonanol, we find Taylor-Aris dispersion lengths of the order of 20 cm. The same reasoning suggests that there is probably also a lower limit to the size of the layers: in the case of nonanol, the Taylor-Aris dispersion length decreases to 25 cm for a layer width of 100 μm. Hence, a layering process is not automatically obtained.

On the other hand, there are cases where mixing is desirable, such as fertility applications where one fluid (purified sperm preparation) needs to be mixed with another (sperm cryoprotectant) at a planned rate. In this case, mixing features—inspired by the many devices developed for forced flows— can be added in the main channel after the last TGV. For example, turns might promote mixing. This effect—called Dean effect—is due to the formation of a vortex in the turn. The formation of a vortex in a turn is characterized by the Dean number[39,40]

$$De = Re\sqrt{\frac{R_H}{R_{turn}}} = \frac{VR_H}{\nu}\sqrt{\frac{R_H}{R_{turn}}}, \tag{9}$$

where *De* is the Dean number and *Re* the Reynolds number. The Dean number must be larger than 1 to observe a vortex in the turn. In our case, $V \sim 3$ mm/s, $R_H \sim 1$ mm, $\nu \sim 1.3\ 10^{-5}$ m^2/s, so that $Re \sim 0.2$ and $De \sim 0.1$ which explains the absence of mixing in the turns.[39,40] Note that this low Dean number is due to the high value of the viscosity and relatively low surface tension of nonanol that condition the velocity of the open capillary flow. Complete mixing is also not seen in the paper pads as shown by the flow profile of the paper pads (**Figure C15**), but a deeper study in the mixing within the paper pads is a focus for future work. However, this might not be the case for "faster" liquids, such as water, isopropyl alcohol solutions, etc. A definition of "faster" liquids is given in reference[36].

Lastly, coloring the different layers of the flowing liquids enables an accurate observation of the open capillary flow in a turn. It is observed that the innermost part of the fluid flows first in a turn, then the outer fluid catches up. This observation has already been reported in the literature[41] which is due to the travel length of each layer remaining the same.

4.2.5 Trigger valves enable nitrite detection in open channels

Lastly, as a proof-of-concept, we applied the open channel trigger valves to the detection of nitrites in water and meat samples. This approach takes advantage of the precise control of capillary flow dynamics to facilitate sequential reagent flow and mixing. For nitrite detection, the Griess reaction was exploited using sulfanilamide (Reagent 1) as aromatic amine and N-1-(naphthyl)ethylenediamine (Reagent 2) as a coupling agent from a commercially-available nitrite colorimetric test kit. The Griess reaction is an azo coupling mechanism, where an aromatic amine in acidic conditions reacts with nitrite ions to form a reactive diazonium salt, which can be combined with an electron-rich coupling agent to form a diazo dye characterized by absorption of visible light at 540 nm. This reaction enables a colorimetric response visible by the naked eye with a pink color, the intensity of which correlates with nitrite concentration. By utilizing open channel TGVs, the system ensures controlled successive interactions between reagents and the analyte; it is important that the sample is first mixed with the Reagent 1 before mixing with Reagent 2. We designed a device (engineering drawing found in **Figure C7**) with two TGVs and two circular mixing paper pads (one after each TGV) to facilitate reagent mixing. Reagent 1 is released by the first valve and flows into the main channel to reach the first mixing paper pad together with the sample. The presence of a paper pad contributes to mixing the reagents and forming the diazonium salt intermediate before reaching the second valve. When the mixing flow reaches the last valve, Reagent 2 is released and mixed in a second circular paper pad, enabling the final stage of mixing. This second pad also functions as the test pad for result evaluation by the naked eye through a change in color from white to pink if nitrite ions are present.

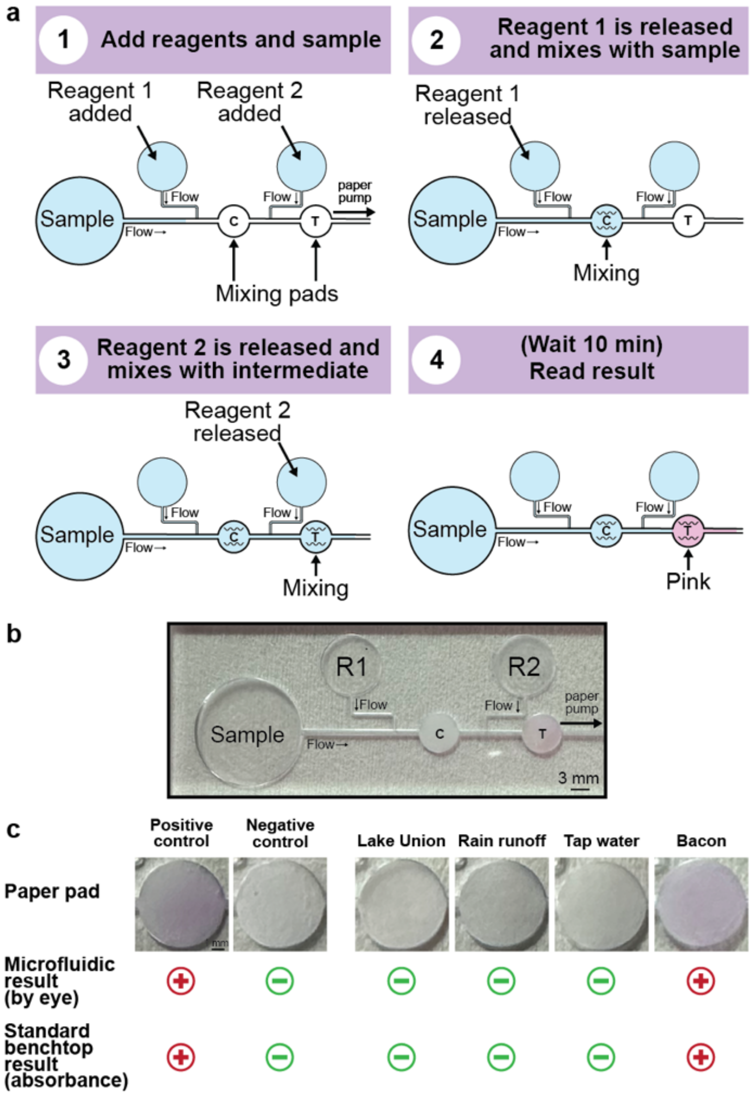

Figure 4.6. *Trigger valves enable on-chip nitrite detection via the Griess reaction.* (**a**) Schematic of device operation using the Griess reaction. Reagents 1 and 2 (R1 and R2) are added to the side reservoirs and are subsequently released by the flow of the sample with interspersed mixing steps via circular paper pads. Pads function as mixers as well as control (C) and test (T) zones. (**b**) Representative photograph of a device to detect nitrites in bacon samples. (**c**) Representative images of paper pads from Griess reaction with a 5 mg/L nitrite ion standard solution (positive control), deionized and distilled water (negative control), Lake Union (Seattle, Washington) water sample, rain runoff water sample, Seattle tap water sample, and a bacon sample. A red plus sign denotes a positive test result; A green minus sign denotes a negative test result (pink not visible by eye or spectrophotometer readout yielding a concentration below 1 mg/L). Experiments were done in triplicate (n=3) with different devices (**Figure C16**). Concentration data for the environmental and meat samples measured using the standard benchtop method can be found in **Table C4**.

Using our device, we tested deionized and distilled water and a 5 mg/L nitrite ion standard solution as negative and positive controls, respectively. We expected no color change in the deionized and distilled water and a pink color change in the nitrite standard solutions, which were observed in our experiments. We then applied this work to environmental samples of water collected from Lake Union (Seattle, Washington), rain runoff from a rose garden, and a Seattle water tap. As nitrite can be found in fertilizers and agricultural lands, we chose various water sources to test for nitrite. In these tests, we did not detect a color change by eye. We then compared our results to the gold standard benchtop method through absorbance measurements; the absorbance values were below our set threshold of 1 mg/L (the United States Environmental Protection Agency (EPA) Maximum Contaminant Level (MCL) for drinking water). Lastly, we tested commercially-available bacon strips for the presence of nitrite, a commonly used food additive. We were able to detect visually the presence of nitrite via our microfluidic device and confirmed this result through the gold standard benchtop method. These systems are particularly suited for point-of-need applications in environmental monitoring, where rapid and reliable detection of nitrite and other analytes is critical. Taken together, we conclude that open trigger valves can be used to simplify workflows for multistep reactions.

4.3 Conclusion

In this work, we have developed the concept of a TGV for capillary flows in open channels, building on prior work on valving in closed channels[8–10,12–24]. We demonstrate that the TGV principle is compatible with open capillary flows using the example of stair-step TGVs. This type of valve is highly effective because the side fluids are stably immobilized by the sharp solid edges on three sides of the aperture and the presence of air on the fourth, upper side. This work—while fundamental here—has the potential to be useful in a multitude of fields such as biomedical research, biosensors, and point-of-care diagnostics.

Using TGVs in series—on the same side or on opposite sides of the main channel—results in the multi-layering of fluid flows. In conventional microfluidics, co-flows have already been achieved due to the high degree of laminarity. Here, we show that layered co-flows can also be achieved for capillary flows in open channels. This principle is also valid for closed-channel capillary flows. The layering continues along the entire channel due to poor molecular mixing caused by low Reynolds numbers. This occurs when the channel length is much shorter than the threshold length predicted by the Taylor-Aris dispersion theory. At low velocities (approximately <5 mm/s) and intermediate to high viscosities (>4 mPa.s; e.g., nonanol capillary flow)[36], no vortex forms in the channel turns—in line with Dean's vortex theory—and no liquid mixing occurs. However, this applies to very viscous liquids. Analyzing Dean's flow in turning open channels is a logical extension of this work. In addition, we observed a 3D effect in the co-flows where the fluid layers overlap along the flow, which will be a focus of future work.

The flow dynamics can be predicted by an analytical model based on the fundamental concept of average friction length, which describes wall friction. In the viscous mode—quickly established in the channels—the model balances the constant capillary force (as long as the main channel maintains a constant cross-section) and the pressure drop due to friction in the main and various side channels. A recurrence relation is derived to calculate the flow dynamics for an arbitrary number of TGVs.

Very narrow co-flows are of great interest for applications in biology and chemistry. This work shows that very narrow liquid layers can co-flow in an open channel depending on the geometric configuration of the channels. For example, with three TGVs in series, the width of the fluid layers is less than one-fourth of the main channel width. Achieving smaller scale widths is important for open microfluidic applications and opens a new avenue for small scale patterning of fluids (e.g., hydrogels[42]), chemical micro-reactions, or could be a precursor to mixing.

4.4 Materials and Methods

4.4.1 Device design and fabrication

Two general device configurations were designed for this study: three TGVs oriented along the same side and the opposite side of the main channel. All devices had a main channel with cross-section dimensions of width and height equal to 1 mm. The side channels had cross-section dimensions of width = 400 μm, height = 600 μm with a TGV gate at the intersection of the end of the side channel and the main channel. Each device differed by the total length of the main and side channels, distance between TGV gates, and the configuration of the side channels along the main channel. For the Griess reaction device, two trigger valves were used and a circular well (7.1 mm diameter) were added after each trigger valve for reagent mixing. Images and schematics of two representative designs can be found in **Figure 4.3**. Engineering drawings of all the devices used in this study can be found in **Figure C6** and **C7**.

Computer-aided designs (CAD) and computer-aided machining (CAM) G-code (.simpl) files for the devices were created in Autodesk Fusion (Autodesk, San Francisco, California). Devices were milled using a Datron Neo computer numerical control (CNC) mill (Datron Dynamics, Milford, New Hampshire) in 3.175 mm poly(methyl)methacrylate plates (#8560K239; McMaster-Carr, Sante Fe Springs, California) for the open-channel flow dynamics experiments or 4.00 mm polystyrene plates (#ST31-SH-000200; Goodfellow Corporation, Pittsburgh, Pennsylvania) for the nitrite detection via the Griess reaction. The channels were milled to have rounded inner corners to prevent the formation of capillary filaments using endmills with a cutter diameter of 1/32” (TR-2-0312-BN) or 1/64” (TR-2-0150-BN) from Performance Micro Tool (Janesville, Wisconsin). Channel dimensions and the quality of the milled cuts were verified using a Keyence wide area 3D measurement VR-5000 profilometer (Keyence Corporation of America, Itasca, Illinois). The channel bottom is estimated to have a few microns of roughness due to the

Datron milling process, which is one magnitude below the roughness values observed by Lade *et al.* to produce substantial fluctuations in velocities in the capillary flow.[43]

After fabrication, the devices were ultra-sonicated in 70% (v/v) aqueous ethanol for 30 minutes to remove any residues and debris using the Branson M2800H. The cleaning solvent was reused no more than five times. After sonication, the devices were rinsed in fresh 70% (v/v) aqueous ethanol and subsequently in deionized (DI) water. Devices were then added to a bioassay dish and partially covered with the lid to dry in the hood overnight. For the devices milled in polystyrene, devices were oxygen-plasma treated with a Diener Zepto PC EX Type PB plasma treater.

Paper pads for the devices were designed in Adobe Illustrator 2023 (Adobe, San Jose, California) and cut into 15.2 mm wide and 25 mm long rectangular pieces or into a circular shape with a 7.00 mm diameter. The paper pads were Cytiva Whatman #1 filter papers (#1001-185) and cut out using the Graphtec CE-7000 plotter cutter and the Cutting Master 5 program (Graphtec America, Irvine, California). Paper pads were stored in a bioassay dish prior to use.

4.4.2 Solvent preparation and physical properties

For trials conducted with channels on the same side in our flow velocity experiments, nonanol (Sigma-Aldrich, # 131210) served as the flowing liquid. Dyed nonanol solutions were made using Sudan I (Sigma-Aldrich, #103624), Sudan III (Sigma-Aldrich, #S4131), Solvent Green 3 (Sigma-Aldrich, #211982), and Solvent Yellow 7 (#S4016), each at concentrations of 0.5 mg/ml or 1.43 mg/ml. For all other devices, stock solutions of dyed nonanol were prepared using Sudan I, Sudan III, Solvent Green 3, and Solvent Yellow 7 in 10 ml volumetric flasks at concentrations of 1 mg/ml. These solutions were subsequently diluted with nonanol to concentrations of 0.5 mg/ml or 1.43 mg/mL for all trials.

For the Griess reaction, sodium nitrite (#S2252, Sigma-Aldrich, St. Louis, Missouri) in H_2O was used as flowing liquid. A stock solution of 750 mg/L of sodium nitrite in ASTM H_2O (#6442-

85, Harleco, was diluted up to reach a concentration of nitrite ions of 5.0 mg/L. Griess reactants, sulfanilamide (Reagent I) and N-(1-Naphthyl)-Ethylenediamine in hydrochloric acid (Reagent II) from the “Nitrite/Nitrate Colorimetric Test” (Roche) kit (#11746081001, Millipore Sigma-Aldrich, St. Louis, Missouri). Reagents I and II were used as provided and not diluted. Environmental water samples were collected and stored at 4°C prior to sample preparation as followed: a 150 mL water sample was collected from Lake Union, Seattle, Washington with a Corning polystyrene bottle, a 15 mL sample of rain runoff from a rose garden was collected with an eyedropper into a 15 mL Falcon conical tube, and commercially available bacon (Private Collection center-cut double smoked bacon) was procured at a local grocery store. Tap water was collected in a 15 mL Falcon conical tube prior to experimentation. The water sample collected from Lake Union and the rain run-off were filtered twice using a 0.45 µm nylon (Fisherbrand Basix, Thermo Fisher Scientific, Waltham, Massachusetts) and a 0.2 µm Whatman cellulose acetate (CA) syringe filter (#6901-2502, Cytiva, Danaher Corporation, Washington, D.C.) to filter out any sediment and debris. The bacon was processed as described by Crowe *et al*.[44] The bacon sample was then filtered three times using a 190 µm fine mesh paint strainer (Magca LTD), 0.22 µm CA vacuum filter (Corning Incorporated, Corning, New York), and lastly, a 0.2 µm CA syringe filter.

4.4.3 Open-channel flow experiments

The devices were positions on a white background atop an adjustable lab jack. Videos capturing the progression of solvent flow in the devices were recorded using a Nikon D5300 ultra-high resolution single lens reflective (SLR) camera at 60 fps. Tabletop photography lights were adjusted to reduce shadows in the video. To obtain the distance that the fluid in the main channel traveled over time and/or to demonstrate fluid layering, the dyed nonanol was used and a paper pad was inserted into the rectangular outlet reservoir.

For the devices with extended lengths (**Figure 4.3**) between the TGVs, 106.02 µL of blue, yellow, and red dyed nonanol were added to the first, second, and third side channels, respectively. For the devices with 3.70 mm between the valves (**Figure 4.4** and **4.5**) on the same side and opposite sides of the channel, 57.02 µL were used instead. A visual check for depinning at the gate was done to ensure fluid flow is stopped. Afterwards, 490 µL of orange-dyed nonanol was added to the circular main reservoir. Devices were left to flow to release the TGVs and data collection stopped when the paper pad wicked the fluid. For the travel distance and fluid velocity experiments, data collection stopped when the paper pad wicked the fluid. For the layering experiments, the device with the valves on the same side followed the same order of colored nonanol in the side channels as the fluid velocity experiments. The device with TGVs on opposite sides of the main channel, blue, red, and yellow dyed nonanol were added first, second, and third TGVs, respectively, for enhanced contrast between the layers and better visualization of the fluid layering.

4.4.4 Nitrite detection via the Griess reaction experiment

A calibration curve was generated using a 96-well plate and the nitrite detection kit with standards (in triplicate) of the following concentrations: 5.00, 3.75, 2.5, 1.00, 0.5, 0.25, 0.1, and 0.05 mg/L (0.05 mg/L sample as not included in the calibration curve due to a negative absorbance value). Water samples from Lake Union, rain run-off, faucet tap, and bacon were prepared in triplicate wells and prepared as described by the kit protocol. After 15 minutes, the absorbance of each well at 540 nm was measured using a Cytation 5 cell imaging multimode reader (Agilent Biotek, Santa Clara, California). The mean absorbance values were used for the calibration curve and the samples. Sample concentrations were interpolated using the equation of the standard curved and reported as a mean concentration (± standard deviation) (**Table C4**).

For the microfluidic experiment, two circular paper pads on top of each other were inserted into the circular wells and one rectangular paper pad was added to the end reservoir. 57.02 µL of Reagent I and Reagent II were added to the first and second side channels, respectively, into the device shown in **Figure C16**. 300 µL of nitrite sample were added to the main reservoir and devices were left to flow to release the TGVs and mix the reactants. Six refills of 57.2 µL were done in sequence to maintain Laplace pressure. In the future, the device geometry could be modified to eliminate the need for refills. Fluids were left to flow for 10 minutes after the release of the second valve. At the 10-minute mark, the device was flipped over onto a TechniCloth (#TX609, TexWipe, Kernersville, North Carolina) to stop the flow. On the backside, the second paper pad was visually evaluated for a pink color change by comparing the color with the color of the control paper pad (the first paper pad along the main channel). Images were taken with an iPhone 14 Pro smartphone camera.

4.4.5 Image capture and data analysis

Images for the fluid dynamics were analyzed as described by Tokihiro *et al.*[36] In brief, an image was captured every 10-30 frames using a custom Python program for the travel distance and velocity analysis. From the images, the fluid front was tracked using the segmented line and measure tools in ImageJ (National Institutes of Health). The resulting measurements were exported as a .csv file. For the layering images, every frame was extracted from the video using the custom python program for the layering measurements. The thickness of the topmost layers was measured after 0.5 mm from each valve until the fluid front reached the end of the frame. The measurements were exported as a .csv file. MATLAB codes were prepared for theory projects and are included in the supplementary material.

4.5 References

1. Casavant, B. P.; Berthier, E.; Theberge, A. B.; Berthier, J.; Montanez-Sauri, S. I.; Bischel, L. L.; Brakke, K.; Hedman, C. J.; Bushman, W.; Keller, N. P.; Beebe, D. J. Suspended Microfluidics. *Proc Natl Acad Sci U S A* **2013**, *110* (25), 10111–10116.
2. Berthier, E.; Dostie, A. M.; Lee, U. N.; Berthier, J.; Theberge, A. B. Open Microfluidic Capillary Systems. *Anal Chem* **2019**, *91* (14), 8739–8750.
3. Berthier, J.; Brakke, K. A.; Berthier, E. *Open Microfluidics*; Scrivener-Wiley Publishing, 2016.
4. Oliveira, N. M.; Vilabril, S.; Oliveira, M. B.; Reis, R. L.; Mano, J. F. Recent Advances on Open Fluidic Systems for Biomedical Applications: A Review. *Materials Science and Engineering: C* **2019**, *97*, 851–863.

5. Kaigala, G. V.; Delamarche, E. *Open-Space Microfluidics: Concepts, Implementations, Applications*; Wiley Publishing, 2018.
6. Zeng, Y.; Khor, J. W.; Van Neel, T. L.; Tu, W.-C.; Berthier, J.; Thongpang, S.; Berthier, E.; Theberge, A. B. Miniaturizing Chemistry and Biology Using Droplets in Open Systems. *Nature Reviews Chemistry* | **2023**, *7*, 439–455.
7. Dudukovic, N. A.; Fong, E. J.; Gemeda, H. B.; Deotte, J. R.; Cerón, M. R.; Moran, B. D.; Davis, J. T.; Baker, S. E.; Duoss, E. B. Cellular Fluidics. *Nature* **2021**, *595*, 58–65.
8. Lynn, N. S.; Dandy, D. S. Passive Microfluidic Pumping Using Coupled Capillary/Evaporation Effects. *Lab Chip* **2009**, *9* (23), 3422–3429.
9. Zimmermann, M.; Hunziker, P.; Delamarche, E. Valves for Autonomous Capillary Systems. *Microfluid Nanofluidics* **2008**, *5* (3), 395–402.
10. Melin, J.; Roxhed, N.; Gimenez, G.; Griss, P.; Vanderwijngaart, W.; Stemme, G. A Liquid-Triggered Liquid Microvalve for on-Chip Flow Control. *Sens Actuators B Chem* **2004**, *100* (3), 463–468.
11. Azizian, P.; Casals-Terré, J.; Ricart, J.; Cabot, J. M. Diffusion-Free Valve for Preprogrammed Immunoassay with Capillary Microfluidics. *Microsyst Nanoeng* **2023**, *9* (1), 91.
12. Olanrewaju, A. O.; Ng, A.; DeCorwin-Martin, P.; Robillard, A.; Juncker, D. Microfluidic Capillaric Circuit for Rapid and Facile Bacteria Detection. *Anal Chem* **2017**, *89* (12), 6846–6853.
13. Achille, C.; Parra-Cabrera, C.; Dochy, R.; Ordutowski, H.; Piovesan, A.; Piron, P.; Van Looy, L.; Kushwaha, S.; Reynaerts, D.; Verboven, P.; Nicolaï, B.; Lammertyn, J.; Spasic, D.; Ameloot, R. 3D Printing of Monolithic Capillarity-Driven Microfluidic Devices for Diagnostics. *Advanced Materials* **2021**, *33* (25), 2008712.
14. Safavieh, R.; Juncker, D. Capillarics: Pre-Programmed, Self-Powered Microfluidic Circuits Built from Capillary Elements. *Lab Chip* **2013**, *13* (21), 4180–4189.
15. Zhang, Y.; Li, Y.; Luan, X.; Li, X.; Jiang, J.; Fan, Y.; Li, M.; Huang, C.; Zhang, L.; Zhao, Y. A 3D Capillary-Driven Multi-Micropore Membrane-Based Trigger Valve for Multi-Step Biochemical Reaction. *Biosensors (Basel)* **2022**, *13* (1).
16. Gervais, L.; de Rooij, N.; Delamarche, E. Microfluidic Chips for Point-of-Care Immunodiagnostics. *Adv Mater* **2011**, *23* (24), H151–H176.
17. Olanrewaju, A.; Beaugrand, M.; Yafia, M.; Juncker, D. Capillary Microfluidics in Microchannels: From Microfluidic Networks to Capillaric Circuits. *Lab Chip* **2018**, *18* (16), 2323–2347.
18. Wang, S.; Zhang, X.; Ma, C.; Yan, S.; Inglis, D.; Feng, S. A Review of Capillary Pressure Control Valves in Microfluidics. *Biosensors (Basel)* **2021**, *11* (10), 405.
19. Zhang, L.; Jones, B.; Majeed, B.; Nishiyama, Y.; Okumura, Y.; Stakenborg, T. Study on Stair-Step Liquid Triggered Capillary Valve for Microfluidic Systems. *Journal of Micromechanics and Microengineering* **2018**, *28* (6), 065005.
20. Choi, J.; Kang, D.; Han, S.; Kim, S. B.; Rogers, J. A. Thin, Soft, Skin-Mounted Microfluidic Networks with Capillary Bursting Valves for Chrono-Sampling of Sweat. *Adv Healthc Mater* **2017**, *6* (5), 1601355.
21. Lee, C.-Y.; Wang, W.-T.; Liu, C.-C.; Fu, L.-M. Passive Mixers in Microfluidic Systems: A Review. *Chemical Engineering Journal* **2016**, *288*, 146–160.
22. Menges, J.; Meffan, C.; Dolamore, F.; Fee, C.; Dobson, R.; Nock, V. New Flow Control Systems in Capillarics: Off Valves. *Lab Chip* **2021**, *21* (1), 205–214.
23. Kinahan, D. J.; Kearney, S. M.; Dimov, N.; Glynn, M. T.; Ducrée, J. Event-Triggered Logical Flow Control for Comprehensive Process Integration of Multi-Step Assays on Centrifugal Microfluidic Platforms. *Lab Chip* **2014**, *14* (13), 2249–2258.

24. Mohammed, M. I.; Abraham, E.; Desmulliez, M. P. Y. Rapid Laser Prototyping of Valves for Microfluidic Autonomous Systems. *Journal of Micromechanics and Microengineering* **2013**, *23* (3), 035034.
25. Gosselin, D.; Berthier, J.; Chaussy, D.; Belgacem, N. Capillary Flows: Dynamic and Geometry Effects. In *COMSOL Conference*; Grenoble, France, 2015.
26. Berthier, J.; Brakke, K. A.; Berthier, E. Spontaneous Capillary Flows in Open U-Grooves. In *Open Microfluidics*; Scrivener-Wiley Publishing, 2016.
27. Li, Q.; Niu, K.; Wang, D.; Xuan, L.; Wang, X. Low-Cost Rapid Prototyping and Assembly of an Open Microfluidic Device for a 3D Vascularized Organ-on-a-Chip. *Lab Chip* **2022**, *22* (14), 2682–2694.
28. Nijhuis, J.; Schmidt, S.; Tran, N. N.; Hessel, V. Microfluidics and Macrofluidics in Space: ISS-Proven Fluidic Transport and Handling Concepts. *Frontiers in Space Technologies* **2022**, *2*, 779696.
29. Nebuloni, F.; Do, Q. B.; Cook, P. R.; Walsh, E. J.; Wade-Martins, R. A Fluid-Walled Microfluidic Platform for Human Neuron Microcircuits and Directed Axotomy. *Lab Chip* **2024**, *24* (13), 3252–3264.
30. Rane, A.; Tate, S.; Sumey, J. L.; Zhong, Q.; Zong, H.; Purow, B.; Caliari, S. R.; Swami, N. S. Open-Top Patterned Hydrogel-Laden 3D Glioma Cell Cultures for Creation of Dynamic Chemotactic Gradients to Direct Cell Migration. *ACS Biomater Sci Eng* **2024**, *10* (5), 3470–3477.
31. Buguin, A.; Talini, L.; Silberzan, P. Ratchet-like Topological Structures for the Control of Microdrops. *Applied Physics A* **2002**, *75* (2), 207–212.
32. Ondarçuhu, T. Total or Partial Pinning of a Droplet on a Surface with a Chemical Discontinuity. *Journal de Physique II* **1995**, *5* (2), 227–241.
33. Bico, J.; Marzolin, C.; Quéré, D. Pearl Drops. *Europhysics Letters (EPL)* **1999**, *47* (2), 220–226.
34. Berthier, J.; Brakke, K. A. *The Physics of Microdroplets*; Scrivener-Wiley Publishing, 2014.
35. Berthier, J.; Gosselin, D.; Berthier, E. A Generalization of the Lucas–Washburn–Rideal Law to Composite Microchannels of Arbitrary Cross Section. *Microfluid Nanofluidics* **2015**, *19* (3), 497–507.
36. Tokihiro, J. C.; McManamen, A. M.; Phan, D. N.; Thongpang, S.; Blake, T. D.; Theberge, A. B.; Berthier, J. On the Dynamic Contact Angle of Capillary-Driven Microflows in Open Channels. *Langmuir* **2024**, *40* (13), 7215–7224.
37. Ritter, P.; Osorio-Nesme, A.; Delgado, A. 3D Numerical Simulations of Passive Mixing in a Microchannel with Nozzle-Diffuser-like Obstacles. *Int J Heat Mass Transf* **2016**, *101*, 1075–1085.
38. Ward, K.; Fan, Z. H. Mixing in Microfluidic Devices and Enhancement Methods. *Journal of Micromechanics and Microengineering* **2015**, *25* (9), 094001.
39. Dean, W. R. Note on the Motion of Fluid in a Curved Pipe. *The London, Edinburgh, and Dublin Philosophical Magazine and Journal of Science* **1927**, *4* (20), 208–223.
40. Dean, W. R. The Stream-Line Motion of Fluid in a Curved Pipe. *The London, Edinburgh, and Dublin Philosophical Magazine and Journal of Science* **1928**, *5* (30), 673–695.
41. Nivedita, N.; Ligrani, P.; Papautsky, I. Dean Flow Dynamics in Low-Aspect Ratio Spiral Microchannels. *Sci Rep* **2017**, 44072.
42. Lee, U. N.; Day, J. H.; Haack, A. J.; Bretherton, R. C.; Lu, W.; DeForest, C. A.; Theberge, A. B.; Berthier, E. Layer-by-Layer Fabrication of 3D Hydrogel Structures Using Open Microfluidics. *Lab Chip* **2020**, *20* (3), 525–536.
43. Lade, R. K.; Hippchen, E. J.; Macosko, C. W.; Francis, L. F. Dynamics of Capillary-Driven Flow in 3D Printed Open Microchannels. *Langmuir* **2017**, *33* (12), 2949–2964.
44. Crowe, W.; Elliott, C. T.; Green, B. D. Evaluating the Residual Nitrite Concentrations of Bacon in the United Kingdom. *Foods* **2020**, *9* (7), 916.

Chapter 5 | Open-Channel Droplet Microfluidic Platform for Passive Generation of Human Sperm Microdroplets

Reproduced in part from Nicholson, T.M.;,# **Tokihiro, J.C.;*** Tu, W.C.; Khor, J.W.; Lee, U.N.; Berthier, E.; Amory, J.K.; Walsh, T.J.; Muller, C.H.; Theberge, A.B.# Open-channel droplet microfluidic platform for passive generation of human sperm microdroplets. ACS Biomaterials Science and Engineering, **2025**, 11(3), 1373–1378.*
**Equal Contribution*
#Co-corresponding authors

Please refer to journal site for supplementary materials referenced in this chapter: 10.1021/acsbiomaterials.4c02005

TMN and JCT conducted the human sperm experiments. JCT fabricated the devices. JCT and WCT tested the devices and conducted and analyzed the microdroplet volume experiment. TMN, JCT, and WCT conducted and analyzed the device usability experiments. JCT, JW, and UNL designed and modified the droplet generator. JW designed the droplet holder. TMN, JKA, TJW, and CHM advised on the human sperm experiments. TMN, JCT, WCT, CHM, and ABT interpreted the results. TMN, JCT, WCT, and ABT designed the study and interpreted the results. TMN, JCT, WCT, JKA, TJW, CHM, and ABT conceptualized ideas. TMN and ABT supervised the work. TMN, JCT, WCT, and ABT wrote the manuscript with all authors revising.

Abstract: Sperm cryopreservation is important for many individuals across the globe. Recent studies show that vitrification is a valuable approach for maintaining sperm quality after freeze-thawing processes and requires sub-microliter to microliter volumes. A major challenge for the adoption of vitrification in fertility laboratories is the ability to pipette small volumes of sample. Here, we present an open droplet generator that leverages open-channel microfluidics to passively generate sub-microliter to microliter volumes of purified human sperm samples and preserves sperm kinematics. We conclude that our platform is compatible with human sperm, an important foundation for future implementation of vitrification in fertility laboratories.

5.1 Introduction

Infertility is defined as the inability to conceive after 12 months of unprotected intercourse, or 6 months for couples with a female partner over the age of 35.[1] Infertility is common, affecting 12.7% of couples in the US or one in six individuals worldwide; a male factor is identified in up to half of couples.[2–5] Sperm cryopreservation (freezing of sperm for later use) is a component of treatment for many patients with infertility, and also benefits individuals facing military service, individuals planning treatment for cancer, and transgender or nonbinary individuals prior to therapies that impact fertility potential. Traditional sperm cryopreservation techniques (slow and rapid freezing) are associated with adverse impacts on sperm motility, which may decline by 30-50% post-thaw.[6,7] Thus, there is a clinical need for improvement in sperm cryopreservation to maintain sperm quality.[8]

Ultra-rapid freezing, or vitrification, is the process of directly inserting small volumes of liquid into liquid nitrogen to reduce ice crystal formation and is the standard approach to cryopreservation of oocytes and embryos.[9,10] Prior studies have established the benefits of vitrification for sperm preservation[11,12] and proposed devices that can be used in the vitrification process.[13–15] A major barrier that has prevented the adoption of vitrification for sperm is the need for generation and manipulation of small fluid volumes (< 1 microliter) to achieve the rapid cooling rates required for vitrification.[16–19] In standard vitrification workflows, sperm samples are portioned into sub-microliter to microliter volumes using a pipette, which can be time-consuming and challenging to achieve, thus resulting in a need for generating small volumes in an autonomous fashion.[20]

Towards this need, we present a platform to encapsulate purified sperm in microdroplets which leverages hydrostatic and interfacial surface tensions to autonomously generate microliter to nanoliter droplets[21] without the need for peripheral equipment such as syringe pumps or actuators to drive fluid flow. Our workflow also features a manual step that allows for the manipulation and movement of the droplet through a stylette or forceps into a droplet holder seated in the device, a feature that is only afforded through open channel microfluidics. On a broad scale, microfluidics has been shown to be valuable and fitting for sperm preparation, selection, and analysis for the ability to achieve high-throughput, mimic the female reproductive tract, and enhance assisted reproductive technology (ART) workflows.[22–25] Open droplet microfluidic devices (including this platform) utilize an air-liquid interface via the removal of the device ceiling, allowing for direct access to the droplets within the device which enables transferring, sorting, moving, and patterning of droplets.[26–31] In this study, we have generated sub-microliter to microliter sized droplets of purified sperm samples from three healthy sperm donors and demonstrate preservation of sperm motilities and kinematics pre- and post- sample preparation and droplet generation.

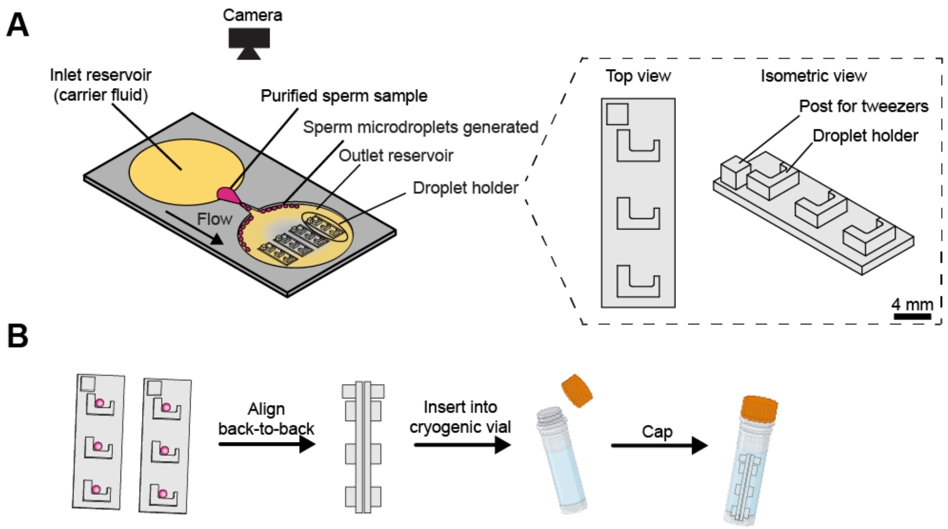

Figure 5.1. Schematic of open-channel droplet generator and insertion of droplet holder into a cryovial. This device (**A**) enables the encapsulation of human sperm in microdroplets and the movement from the device to a droplet holder. This holder contains three slots that can hold one droplet each and, after vitrification (**B**) when placed back-to-back, the holder is able to be placed into a commercial cryogenic vial for long term storage. Created with BioRender.com.

5.2 Results and Discussion

We have adapted an established droplet generator[21] (**Figure 5.1A**) to be able to seat removable droplet holders (**Figure 5.1A**) for the storage of sperm microdroplets in commercial cryogenic vials (**Figure 5.1B**). For ultra-rapid freezing methods such as vitrification via liquid nitrogen, sperm specimens which can contain millions of sperm per milliliter require the sample to be fractioned into small volumes (~1 µL) using a pipette; however, pipetting can be arduous and challenging at low volumes. Our goal for this study is to be able to implement sperm in our device at concentrations that are normal for a healthy patient; encapsulation of sperm at very low concentrations or even a single sperm cell in a microdroplet is not the focus of this work and would only apply to a small percentage of men (1%)[32]. Thus, we leveraged open-channel droplet microfluidics to aliquot purified sperm samples from healthy males with normal sperm counts into microdroplets. The workflow for device operation can be found in **Figure 5.2**. We used purified motile sperm samples at a concentration of approximately 6.1 to 7.7 x 10^6 sperm/mL. A microscope image of a single droplet of the purified sperm can be found in **Figure D1**. We have experimentally determined that the mean volume (± standard deviation) of our droplets is 0.874 µL (± 0.3 µL) (**Figure D2**). Given a 0.874 µL droplet size, we expect 5.5 to 6.9 x 10^3 sperm per droplet, which is more than sufficient for in vitro fertilization (IVF). As sperm requirements vary among fertility treatments, we can meet different needs through droplet pooling to increase sperm numbers or by adjusting the initial concentration of purified sperm that is loaded into the platform. While our droplets are not monodisperse as have been achieved in closed-channel microfluidics[33–35], our goal is not to achieve the same degree of monodispersity, but rather to generate small droplets in a passive open system that allows for subsequent manipulation and movement of the droplets. The droplet volumes and dispersity generated by our system are fully acceptable for vitrification for fertility applications.[36]

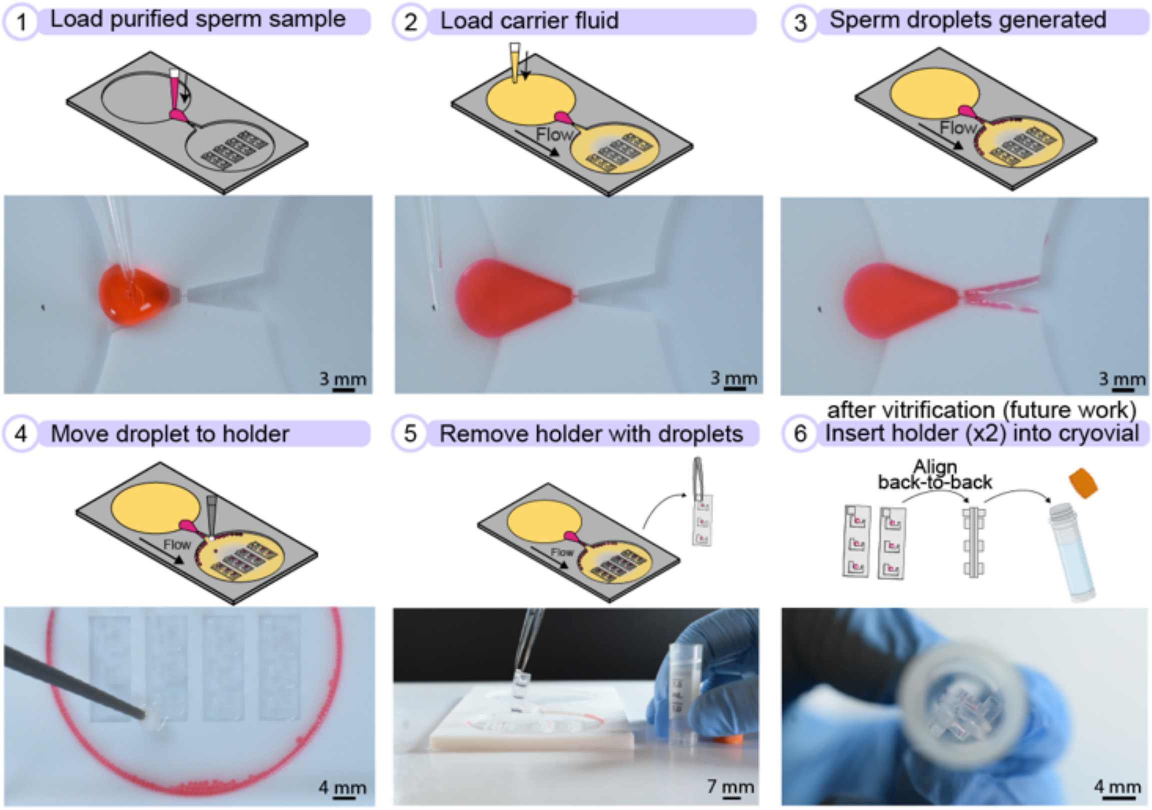

Figure 5.2. Operation of open-channel droplet generator. A 180-µL sample of purified sperm is loaded with a pipette into the inlet region and carrier fluid consisting of 2% fluorosurfactant in HFE-7500 is subsequently added to the inlet reservoir to initiate droplet generation. Droplets are then autonomously generated, which can be moved to the droplet holder using a stylette or PTFE-coated forceps. Created with BioRender.com.

Within the device, there are four rectangular wells in the outlet reservoir for the seating of the droplet holders. The droplet holder measures 7 mm wide by 20 mm long and 3.92 mm in height and is fabricated out of polystyrene, which is a known biocompatible material. Each slot has a height of 1.50 mm. Each droplet holder can contain three individual droplets and has a handle to allow the holder to be picked up by forceps for vitrification and back-to-back placement into a cryogenic vial (**Figure 5.1B** and SI video). Additional droplet holders can be used to store additional droplets depending on the fertility preservation goals of the patient. We tested device usability with users of varying degrees of experience by determining the time needed to fill all droplet holder slots (**Figure 5.3**). “Expert” users had prior experience with droplet movement while the “novice” users had basic lab skills, but did not have any experience with the device or droplet movement. Our users were able to move 12 droplets successfully with each user decreasing in time needed with subsequent trials (**Figure 5.3**), demonstrating that even new users can operate our device. Currently, manipulation of microdroplets containing human gametes (oocytes) is performed exclusively by highly trained and experienced embryologists using a micromanipulator microscope. Our usability data supports that sperm microdroplet manipulation with our system could be performed by users with basic lab skills. We also examined droplet stability and imaged droplets over the course of 42 minutes after generation. We found that droplets remained in the partitioned state for the entire length of time. Images of the stable droplets can be found in **Figure D3**. No droplet merging was observed during and after droplet transfer to the holder as seen in video “Droplet moving.mp4”.

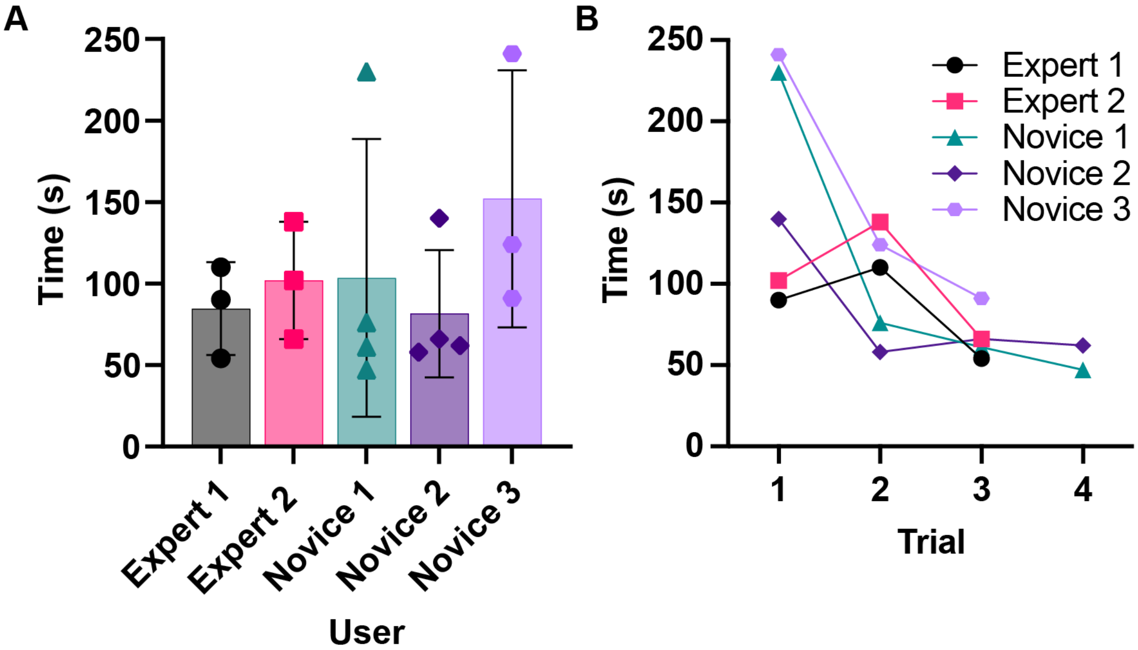

Figure 5.3. Microdroplets can be successfully manipulated by users of varying experience levels. Users at “expert” and “novice” experience levels were asked to move 12 micro-droplets for three or four trials (n=3 or 4). The time needed for each trial was recorded and an average time for each user is shown with the standard deviation (**A**). (**B**) A plot showing the progression of each user and the time required to complete the task over each consecutive trial.

In this study, the use of dye in sperm samples is crucial for visualization during droplet generation and manipulation. To address this, we investigated sperm motility and kinematic parameters before and after exposure to the dye and the PTFE device. We assessed sperm motility parameters in three sperm donors using an automated sperm analyzer platform, Integrated Visual Optic System (IVOS) (**Figure 5.3** and **D4**). A representative participant is presented in **Figure 5.3** and additional participant data can be found in **Figure D4**.

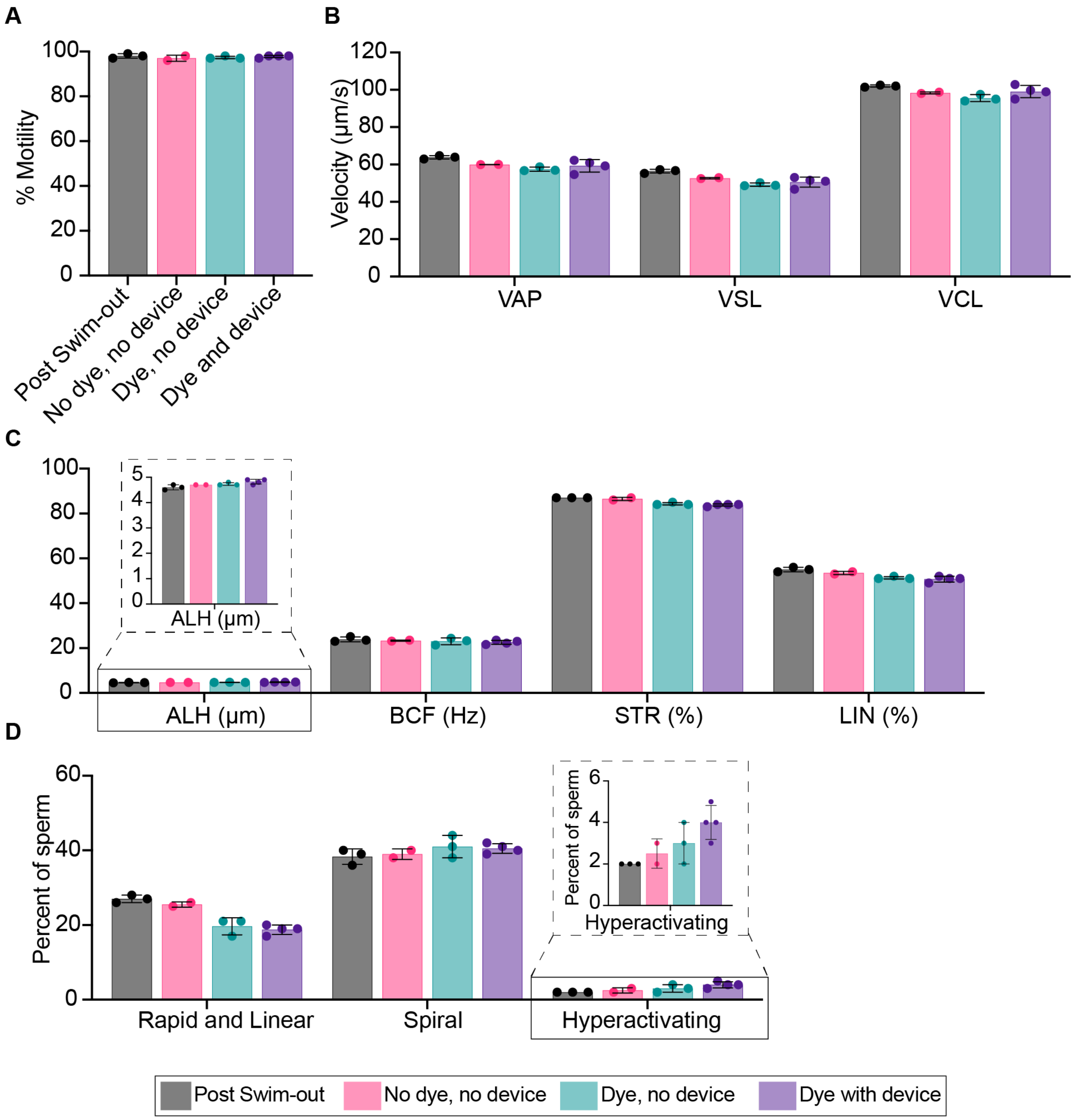

Figure 5.4. Sperm (**A**) motilities, (**B**) velocities, (**C**) amplitude lateral height (ALH), beat/cross frequency (BCF), straight-ness (STR) and linearity (LIN) measurements, and (**D**) movements from one representative participant. The sperm data were collected from post swim-out samples, no dye and no device samples (No dye, no device), with dye (1:500, v/v) without device samples (dye, no device) and with both dye (1:500, v/v) and device samples (dye with device). Three individual participant experiments were conducted with different devices; data from one participant is shown here (**Figure 5.4**), and all data is included in the Appendix (**Figure D4**). Each data point represents an individual device and measurement; the bar graph represents the mean ± SD of n = 2-4 devices/measurements.

In these graphs, we present sperm motility data (**Figure 5.4A**) as well as additional kinematic measures including average path velocity (VAP), straight-line velocity (VSL), curvilinear velocity (VCL), (**Figure 5.4B**) amplitude of lateral head displacement (ALH), beat/cross frequency (BCF), straightness (STR), linearity (LIN), (**Figure 5.4C**) as well as percentage of sperm that are rapid and linear, spiraling, and hyperactivating (**Figure 5.4D**).[37,38] We found no notable decline in motility parameters when comparing the sperm samples exposed to dye and the PTFE device or when one or both of those conditions are absent. We have included the post swim-out parameters here, which are measured immediately after swim-out, to account for differences in sperm motilities and kinematics over time, but no apparent differences were found.

5.3 Conclusion

Here, we have sustained sperm motility and kinematics using healthy male participants with normal sperm parameters with our adapted open-channel droplet generator. A novel droplet holder feature is also presented, allowing for the storage of droplets in cryogenic vials, which is a highly adaptable feature of our platform. Moreover, our device requires only a pipette, the sperm sample, droplet generation reagents, the device, and droplet holders to operate. With no peripheral equipment necessary and no specialized training needed to generate the droplets, there is strong potential to implement this platform in labs across a broad range of resource levels. Most importantly, our device enables direct access to the droplets for selection and manipulation, which is only afforded through open channels. To our knowledge, our device is one of the few to autonomously generate small volumes for the purposes of sperm vitrification. While our workflow is only autonomous in the droplet generation aspect, we eliminated the need for small-volume pipetting, a technical limitation to sperm preparation for vitrification. Future work may include developing methods to automate droplet manipulation and storage as has been done previously in closed systems.[39,40] The device and workflow presented here lays the foundation for a new approach to sample preparation for vitrification of sperm, where maintaining sperm motility after passage through the device is crucial in the successful implementation of this device in the clinical setting. Future work will involve performing vitrification of samples generated by our device and comparison of post-thaw sperm quality with conventional methods. Facilitating the adoption of vitrification for sperm could benefit individuals needing fertility preservation, fertility laboratories, and sperm banks.

5.4 Materials and Methods

The open-platform droplets generator used in this study was developed from Khor et al.[21] The device with a 0.2 mm wide constriction region was chosen since the expected droplet volumes were less than or equal to 1 µL (**Figure 5.1**). Detailed device design and fabrication procedures are in supplemental material. Carrier fluids were prepared from pure HFE-7500 engineered fluid (The 3M Co., St. Paul, Minnesota) with 2 wt% FS-008 fluorosurfactant (RAN Biotechnologies Inc., Beverly, Massachusetts). HEPES buffered formulation with 0.5% Human Serum Albumin sperm wash (#2003, InVitro Care Inc., Frederick, Maryland) was used as the aqueous phase, which was tinted with red dye (McCormick & Co., Hunt Valley, Maryland) at a concentration of 1:500 (v/v) for visualization of the droplets in the device.

Four droplet holders were then inserted into the slots in the outlet reservoir. A 180 µL aliquot of the dyed sperm wash was added to the inlet platform of the constriction region. Afterwards, 1.5 mL of carrier fluid was pipetted to the larger inlet portion of the device. Once droplet generation began, 0.5 mL of carrier fluid was added to maintain hydrostatic pressure. Devices were then observed for passive droplet generation. Video in supplemental materials shows passive droplet formation.

A stylette or Polytetrafluoroethylene (PTFE)-coated straight-tip forceps (#2A-SA-SE-TC15, Excelta One Star, Buellton, CA) were used to move the droplets from the device to the holder. A single droplet was transferred to each of the droplet holder slots. The droplet holders are designed to be placed back-to-back in a commercial 2 mL polypropylene cryogenic vial

(#03374059, Corning Inc., Corning, NY) for long term storage. A video of droplet transfer can be found in the supplementary materials.

Under an approved Institutional Review Board (STUDY00009510) protocol, healthy subjects provided informed consent and semen samples via masturbation following 2-5 days of abstinence.[20] The semen samples were purified using a direct swim-out procedure.20 Motile sperm preparation was added to the device according to Khor et al.[21] and sperm kinematics were measured for different conditions (with and without dye and passage through the device) using the Hamilton Thorne Research (Beverly, MA) Integrated Visual Optical System (IVOS). A detailed protocol for the swim-out and the device operation can be found in **Appendix Section D1**.

5.5 References

1. McLaren, J. F. Infertility Evaluation. *Obstet Gynecol Clin North Am* **2012**, *39* (4), 453–463.
2. Carson, S. A.; Kallen, A. N. Diagnosis and Management of Infertility: A Review. *JAMA* **2021**, *326* (1), 65–76.
3. Agarwal, A.; Mulgund, A.; Hamada, A.; Chyatte, M. R. A Unique View on Male Infertility around the Globe. *Reproductive Biology and Endocrinology* **2015**, *13* (1), 37.
4. Agarwal, A.; Baskaran, S.; Parekh, N.; Cho, C.-L.; Henkel, R.; Vij, S.; Arafa, M.; Panner Selvam, M. K.; Shah, R. Male Infertility. *The Lancet* **2021**, *397* (10271), 319–333. https://doi.org/10.1016/S0140-6736(20)32667-2.
5. Dohle, G.; Colpi, G.; Hargreave, T.; Papp, G.; Jungwirth, A.; Weidner, W. EAU Guidelines on Male Infertility. *Eur Urol* **2005**, *48* (5), 703–711. https://doi.org/10.1016/j.eururo.2005.06.002.
6. Kramer, R. Y.; Garner, D. L.; Bruns, E. S.; Ericsson, S. A.; Prins, G. S. Comparison of Motility and Flow Cytometric Assessments of Seminal Quality in Fresh, 24-Hour Extended and Cryopreserved Human Spermatozoa. *J Androl* **1993**, *14* (5), 374–384.
7. Donnelly, E. T.; Steele, E. K.; McClure, N.; Lewis, S. E. M. Assessment of DNA Integrity and Morphology of Ejaculated Spermatozoa from Fertile and Infertile Men before and after Cryopreservation. *Human Reproduction* **2001**, *16* (6), 1191–1199.
8. Pusch, H. H. The Importance of Sperm Motility for the Fertilization of Human Oocytes in Vivo and in Vitro. *Andrologia* **2009**, *19* (5), 514–527.
9. Rozati, H.; Handley, T.; Jayasena, C. Process and Pitfalls of Sperm Cryopreservation. *J Clin Med* **2017**, *6* (9), 89.
10. Rienzi, L.; Gracia, C.; Maggiulli, R.; LaBarbera, A. R.; Kaser, D. J.; Ubaldi, F. M.; Vanderpoel, S.; Racowsky, C. Oocyte, Embryo and Blastocyst Cryopreservation in ART: Systematic Review and Meta-Analysis Comparing Slow-Freezing versus Vitrification to Produce Evidence for the Development of Global Guidance. *Hum Reprod Update* **2016**, *23* (2), 139–155.
11. Isachenko, V.; Isachenko, E.; Katkov, I. I.; Montag, M.; Dessole, S.; Nawroth, F.; van der Ven, H. Cryoprotectant-Free Cryopreservation of Human Spermatozoa by Vitrification and Freezing in Vapor: Effect on Motility, DNA Integrity, and Fertilization Ability. *Biol Reprod* **2004**, *71* (4), 1167–1173.

12. Isachenko, V.; Isachenko, E.; Montag, M.; Zaeva, V.; Krivokharchenko, I.; Nawroth, F.; Dessole, S.; Katkov, I. I.; der Ven, H. van. Clean Technique for Cryoprotectant-Free Vitrification of Human Spermatozoa. *Reprod Biomed Online* **2005**, *10* (3), 350–354.
13. Schuster, T. G.; Keller, L. M.; Dunn, R. L.; Ohl, D. A.; Smith, G. D. Ultra-Rapid Freezing of Very Low Numbers of Sperm Using Cryoloops. *Human Reproduction* **2003**, *18* (4), 788–795.
14. Sun, J.; Chen, W.; Zhou, L.; Hu, J.; Li, Z.; Zhang, Z.; Wu, Y. Successful Delivery Derived from Cryopreserved Rare Human Spermatozoa with Novel Cryopiece. *Andrology* **2017**, *5* (4), 832–837.
15. Chen, Y.; Li, L.; Qian, Y.; Xu, C.; Zhu, Y.; Huang, H.; Jin, F.; Ye, Y. Small-Volume Vitrification for Human Spermatozoa in the Absence of Cryoprotectants by Using Cryotop. *Andrologia* **2015**, *47* (6), 694–699.
16. Tao, Y.; Sanger, E.; Saewu, A.; Leveille, M.-C. Human Sperm Vitrification: The State of the Art. *Reproductive Biology and Endocrinology* **2020**, *18* (1), 17.
17. O'Neill, H. C.; Nikoloska, M.; Ho, H.; Doshi, A.; Maalouf, W. Improved Cryopreservation of Spermatozoa Using Vitrification: Comparison of Cryoprotectants and a Novel Device for Long-Term Storage. *J Assist Reprod Genet* **2019**, *36* (8), 1713–1720.
18. Huang, C.; Gan, R.-X.; Zhang, H.; Zhou, W.-J.; Huang, Z.-H.; Jiang, S.-H.; Ji, X.-R.; Gong, F.; Fan, L.-Q.; Zhu, W.-B. Novel Micro-Straw for Freezing Small Quantities of Human Spermatozoa. *Fertil Steril* **2020**, *114* (2), 301–310.
19. Chen, Y.; Li, L.; Qian, Y.; Xu, C.; Zhu, Y.; Huang, H.; Jin, F.; Ye, Y. Small-Volume Vitrification for Human Spermatozoa in the Absence of Cryoprotectants by Using Cryotop. *Andrologia* **2015**, *47* (6), 694–699.
20. World Health Organization. *WHO Laboratory Manual for the Examination and Processing of Human Semen*, Sixth.; Geneva, 2021.
21. Khor, J. W.; Lee, U. N.; Berthier, J.; Berthier, E.; Theberge, A. B. Interfacial Tension Driven Open Droplet Microfluidics. *Adv Mater Interfaces* **2023**, *10* (7).
22. Eamer, L.; Nosrati, R.; Vollmer, M.; Zini, A.; Sinton, D. Microfluidic Assessment of Swimming Media for Motility-Based Sperm Selection. *Biomicrofluidics* **2015**, *9* (4), 044113.
23. Nosrati, R.; Graham, P. J.; Zhang, B.; Riordon, J.; Lagunov, A.; Hannam, T. G.; Escobedo, C.; Jarvi, K.; Sinton, D. Microfluidics for Sperm Analysis and Selection. *Nat Rev Urol* **2017**, *14* (12), 707–730.
24. Cho, B. S.; Schuster, T. G.; Zhu, X.; Chang, D.; Smith, G. D.; Takayama, S. Passively Driven Integrated Microfluidic System for Separation of Motile Sperm. *Anal Chem* **2003**, *75* (7), 1671–1675.
25. Berendsen, J. T. W.; Kruit, S. A.; Atak, N.; Willink, E.; Segerink, L. I. Flow-Free Microfluidic Device for Quantifying Chemotaxis in Spermatozoa. *Anal Chem* **2020**, *92* (4), 3302–3306.
26. Zeng, Y.; Khor, J. W.; van Neel, T. L.; Tu, W.; Berthier, J.; Thongpang, S.; Berthier, E.; Theberge, A. B. Miniaturizing Chemistry and Biology Using Droplets in Open Systems. *Nat Rev Chem* **2023**, *7* (6), 439–455.
27. Berry, S. B.; Lee, J. J.; Berthier, J.; Berthier, E.; Theberge, A. B. Droplet Incubation and Splitting in Open Microfluidic Channels. *Analytical Methods* **2019**, *11* (35), 4528–4536.
28. Lee, J. J.; Berthier, J.; Brakke, K. A.; Dostie, A. M.; Theberge, A. B.; Berthier, E. Droplet Behavior in Open Biphasic Microfluidics. *Langmuir* **2018**, *34* (18), 5358–5366.
29. Soitu, C.; Stovall-Kurtz, N.; Deroy, C.; Castrejón-Pita, A. A.; Cook, P. R.; Walsh, E. J. Jet-Printing Microfluidic Devices on Demand. *Advanced Science* **2020**, *7* (23).
30. Soitu, C.; Feuerborn, A.; Tan, A. N.; Walker, H.; Walsh, P. A.; Castrejón-Pita, A. A.; Cook, P. R.; Walsh, E. J. Microfluidic Chambers Using Fluid Walls for Cell Biology. *Proceedings of the National Academy of Sciences* **2018**, *115* (26).

31. Soitu, C.; Feuerborn, A.; Deroy, C.; Castrejón-Pita, A. A.; Cook, P. R.; Walsh, E. J. Raising Fluid Walls around Living Cells. *Sci Adv* **2019**, *5* (6).
32. Cocuzza, M.; Alvarenga, C.; Pagani, R. The Epidemiology and Etiology of Azoospermia. *Clinics* **2013**, *68*, 15–26.
33. Nan, L.; Zhang, H.; Weitz, D. A.; Shum, H. C. Development and Future of Droplet Microfluidics. *Lab Chip* **2024**, *24* (5), 1135–1153.
34. Amirifar, L.; Besanjideh, M.; Nasiri, R.; Shamloo, A.; Nasrollahi, F.; de Barros, N. R.; Davoodi, E.; Erdem, A.; Mahmoodi, M.; Hosseini, V.; Montazerian, H.; Jahangiry, J.; Darabi, M. A.; Haghniaz, R.; Dokmeci, M. R.; Annabi, N.; Ahadian, S.; Khademhosseini, A. Droplet-Based Microfluidics in Biomedical Applications. *Biofabrication* **2022**, *14* (2), 022001.
35. Teh, S.-Y.; Lin, R.; Hung, L.-H.; Lee, A. P. Droplet Microfluidics. *Lab Chip* **2008**, *8* (2), 198.
36. Practice Committees of the American Society for Reproductive Medicine and Society of Reproductive Biologists and Technologists. A Review of Best Practices of Rapid-Cooling Vitrification for Oocytes and Embryos: A Committee Opinion. *Fertil Steril* **2021**, *115* (2), 305–310.
37 Mortimer, D.; Barratt, C. L. R.; Bjorndahl, L.; de Jager, C.; Jequier, A. M.; Muller, C. H. What Should It Take to Describe a Substance or Product as “Sperm-Safe.” *Hum Reprod Update* **2013**, *19* (suppl 1), i1–i45.
38. Hamilton Thorne Biosciences. *IVOS Sperm Analysis System*; Hamilton Thorne Biosciences: Beverly, MA, 2022; Vol. 12.
39. Courtney, M.; Chen, X.; Chan, S.; Mohamed, T.; Rao, P. P. N.; Ren, C. L. Droplet Microfluidic System with On-Demand Trapping and Releasing of Droplet for Drug Screening Applications. *Anal Chem* **2017**, *89* (1), 910–915.
40. Huebner, A.; Bratton, D.; Whyte, G.; Yang, M.; deMello, A. J.; Abell, C.; Hollfelder, F. Static Microdroplet Arrays: A Microfluidic Device for Droplet Trapping, Incubation and Release for Enzymatic and Cell-Based Assays. *Lab Chip* **2009**, *9* (5), 692–698.

Appendix

A. Appendix for Chapter 2

Reproduced in part from ***Tokihiro, J.C.;**** *Tu, W.C.;* Berthier, J.;* Lee, J. J.; Dostie, A.; Khor, J.W.; Eakman, M.; Theberge, A.B.;# Berthier, E.# Enhanced capillary pumping using open channel capillary trees with integrated paper pads. Physics of Fluids,* ***2023****, 35, 082120.*

** Equal contribution*

#Co-corresponding authors

TABLE A1. Physical properties of the solvents. The term $\sqrt{\left(\frac{\gamma}{\mu}\right)2\lambda cos\theta^*}$ is the coefficient of the extended Lucas-Washburn law and there is a slight difference between the value obtained from literature and from experiments.

Physical property	50% IPA	Nonanol	Pentanol
[a] Surface tension γ [mN/m]	24	28.5	25.4
[a] Viscosity μ [mPa•s]	3.2	11.2	3.75
[a,b] Contact angle θ [deg]	18	13	10
$\gamma \cos \theta$ [mN/m]	22.8	27.8	25.5
[c] $\gamma \cos \theta^*$ [mN/m]	14.6	15.3	15.5
[d] Literature data $\sqrt{\left(\frac{\gamma}{\mu}\right)2\lambda\, cos\theta^*}$ [mm/s$^{1/2}$]	48.2	28.5	38.7
[e] Experimental data $\sqrt{\left(\frac{\gamma}{\mu}\right)2\lambda cos\theta^*}$ [mm/s$^{1/2}$]	40	23-25	40

[a] air at room temperature[4-7]; [b] contact angle of the solvent on native PMMA; [c] $\cos \theta^*$ is the Cassie contact angle[8]; [d] calculated using values in the table on line 1 (γ), 2 (μ), 5 ($\gamma \cos \theta^*$), and λ = 259 µm[1,2]. [e] fit with the travel distance in the root channel (z_0).

TABLE A2. Characteristic dimensions of the homothetic channels.

Dimension	Level 0 (root)	Level 1	Level 2	Level 3
Width [mm]	1.06	0.90	0.77	0.65
Depth [mm]	1.76	1.50	1.28	1.08
Wetted perimeter p_0 [mm]	4.13	3.51	3.00	2.53
[a]Friction length λ [µm]	259	220	187	159
Cross-sectional area S_0 [mm^2]	1.75	1.26	0.92	0.66

[a] obtained from previous publication.[1,2]

TABLE A3. Characteristics of Whatman #1 paper pads.

[a] Physical and geometrical properties	Symbol	Value	Unit
Permeability	K	2.3×10^{-6}	mm^2
Porosity	φ	0.7	-
Capillary pressure (50% isopropyl alcohol)	P_{cap}	3300	Pa
Capillary pressure (nonanol)	P_{cap}	55004100	Pa
Capillary pressure (pentanol)	P_{cap}	4500	Pa

[a] porosity and permeability are obtained from the literature[3], capillary pressures were determined by fitting K and φ to the experimental data.

Section A1. Dynamics of capillary flow in the open-channel capillary tree

Root channel. We derive first the dynamics in the root channel. Neglecting the evanescent initial inertial regime,[9,10] the balance between capillary force F_{cap} and wall friction F_{drag} leads to

$$F_{cap} = p\,\gamma\,cos\theta^* = F_{drag} = p\,z_0\bar{\tau} = p\,z_0\left(\mu\frac{V_0}{\lambda}\right), \tag{S1}$$

where $\bar{\tau}$ is the average friction, p the total channel perimeter in a cross section, V_0 the average velocity (which is a function of time and/or travel distance), λ the average friction length, μ the viscosity, γ the surface tension, and θ^* the generalized Cassie angle[11] (in order to take into account the free surface of the open channel and accommodate for the potential of non-monolithic channels comprising different materials on the floor and walls). Then we have the relation between travel distance and time

$$\frac{d\,z_0^2}{dt} = \frac{2\,\lambda\,\gamma\,cos\theta^*}{\mu}\,, \tag{S2}$$

And finally

$$z_0 = \sqrt{\frac{2\,\lambda\,\gamma\,cos\theta^*}{\mu}}\,\sqrt{t} \tag{S3}$$

Note that the time at which the flow reaches the bifurcation at a distance L_0 from entrance, is

$$t_0 = \frac{\mu}{2\lambda\,\gamma\,cos\theta^*}\,L_0^2 = \frac{L_0^2}{C} \tag{S4}$$

where $C = \frac{2\,\lambda\,\gamma\,cos\theta^*}{\mu}$.

Tree branches. After the first bifurcation, at the level *n*, we must use a formulation that uses the pressures and write the pressure equilibrium along a fluidic path[1,12–15]

$$p_0\,L_0\,\mu\frac{V_0}{\lambda_0}\frac{1}{S_0} + \cdots + p_n\,z_n\,\mu\frac{V_n}{\lambda_n}\frac{1}{S_n} = \frac{p_n\,\gamma\,cos\theta_n^*}{S_n}\,, \tag{S5}$$

where z_n here is the travel distance in the n^{th} ramification, S_n the cross-sectional area and V_n the velocity in the daughter branch ($V_n = \frac{dz_n}{dt}$). Relation (S5) indicates that the capillary pressure is equal to the pressure associated to the friction along a path starting from the root channel to the n^{th} channel. Using the relations linked to the homothetic ratio α, we have for the cross-sectional perimeters are

$$p_n = \alpha p_{n-1} = \cdots = \alpha^{n-1} p_1 = \alpha^n p_0, \tag{S6}$$

and the cross-sectional areas are

$$S_n = \alpha^2 S_{n-1} = \cdots = \alpha^{2(n-1)} S_1 = \alpha^{2n} S_0 \tag{S7}$$

Moreover, the friction lengths are homothetic because they are proportional to the hydraulic diameter of the channel

$$\lambda_n = \alpha \lambda_{n-1} = \cdots = \alpha^{n-1} \lambda_1 = \alpha^n \lambda_0 \tag{S8}$$

Hence the ratio $\frac{p_i}{\lambda_i}$ is constant for all indices *i* from *0* to *n*, equal to $\frac{p_0}{\lambda_0}$. Moreover, the Cassie angles are everywhere the same, i.e., $\theta^* = \theta_1^* = \cdots = \theta_n^*$. Substituting (S6), (S7) and (S8) in (S5) yields

$$\alpha^{2n} L_0\, V_0 + \alpha^{2(n-1)}\, L_1\, V_1 + .. + \alpha^2 L_{n-1} V_{n-1} + \, z_n\, V_n = \frac{p_n}{p_0} \frac{\gamma}{\mu} \lambda_0\, cos\theta^* \; = \alpha^n \frac{\gamma}{\mu} \lambda_0\, cos\theta^* = \alpha^n \frac{C}{2}. \tag{S9}$$

Using the mass conservation equation,

$$V_0 = (2\,\alpha^2) V_1 = (2\,\alpha^2)^2\, V_2 \; = \cdots = (2\,\alpha^2)^n\, V_n, \tag{S10}$$

and remarking that $V_n = \frac{dz_n}{dt}$, (S9) becomes a differential equation in *z_n* that can be integrated to obtain a quadratic polynomial in z_n

$$z_n^2 + 2[(2\alpha^4)^n L_0 \; + \; (2\,\alpha^4)^{n-1}\, L_1 + \cdots + \; 2\alpha^4 L_{n-1}] z_n = \alpha^n C\, (t - t_{n-1}) \;, \tag{S11}$$

Denoting $A_n = (2\alpha^4)^n L_0 \; + \; (2\,\alpha^4)^{n-1}\, L_1 + \cdots + 2\alpha^4 L_{n-1} = (2\alpha^4)^n L_0 \Sigma_{n-1}$, where $\Sigma_{n-1} = \left[1 + \frac{L_1}{2\alpha^4 L_0} + \cdots + \frac{L_{n-1}}{(2\,\alpha^4)^{n-1} L_0}\right]$, the solution is

$$z_n = A_n \left[-1 + \sqrt{1 + \frac{\alpha^n C}{A_n^2}\, (t - t_{n-1})}\right] \tag{S12}$$

Note that the travel distance given by relation (S12) is not of the conventional Lucas-Washburn form ($z \approx \sqrt{t}$), but of the form $z \approx -A + \sqrt{A^2 + \alpha^n Ct}$.

Section A2. Dynamics of capillary flow in the paper pads (coupled to that in the open-channel capillary tree)

When reaching the extremities of the tree branches, the liquid start wicking the paper pads. The motion wicking of the pads is governed by Darcy's law [16,17]

$$V_p = -\frac{K}{\mu\phi} \nabla P = \frac{K}{\mu\phi} \frac{P_{cap} - P_j}{z_p}. \tag{S13}$$

where P_{cap} is the capillary pressure of the paper and P_j the pressure at the junction channel-paper pad. K is the permeability of the pad and φ its porosity. The index p refers to the paper. The triplet (P_{cap}, K, φ) characterizes the paper strip.[18,19]

Three assumptions are used in the present model. First, the paper pads are homogeneous, i.e., there are no regions of higher or lower porosity. Hence, degree of saturation (local percentage of liquid) is assumed the same everywhere in the paper pad.[20,21] As a consequence, the capillary pressure P_{cap} is constant everywhere, and there is no smearing of the advancing contact line, which is described in the literature as a sharp front approach.[22] Second, it is assumed that the dilatation of the paper fibers with the penetrating the liquid is negligible, so that the porosity φ is constant everywhere in the pad. Third, the cellulose fibers do not absorb the wicking liquid, so that the mass conservation is independent of the time. Then equation (S13) can be cast under the form

$$\frac{d(z_p)^2}{dt} = \frac{2K}{\mu\phi} \left(P_{cap} - P_j\right). \tag{S14}$$

In order to solve equation (S14), the pressure P_j mut be determined. According to (S5)

$$P_j = p_0\, L_0\, \mu \frac{V_0}{\lambda_0} \frac{1}{S_0} + \cdots + p_n\, L_n\, \mu \frac{V_n}{\lambda_n} \frac{1}{S_n} \ , \qquad \text{(S15)}$$

where *n* is the channel level at the junction with the paper pads. Using again (S6), (S7), (S8) and (S10), the pressure P_j can be expressed as

$$P_j = p_0\, L_0\, \mu \frac{V_0}{\lambda_0} \frac{1}{S_0} \left(1 + \frac{L_1}{L_0} \frac{1}{2\, \alpha^4} + \cdots + \frac{L_n}{L_0} \frac{1}{(2\, \alpha^4)^n}\right) = p_0\, L_0\, \mu \frac{V_0}{\lambda_0} \frac{1}{S_0} \Sigma_n \qquad \text{(S16)}$$

Using the mass conservation equation, the velocity V_0 can be expressed in function of the velocity in the paper

$$V_0 S_0 = 2^n \phi V_p S_p \ , \qquad \text{(S17)}$$

where S_p is the total cross-sectional area of the pad. We consider two types of paper pads: rectangular and conical (triangular). We can group together the two geometries by writing

$$S_p = S_{p,0} + 2\beta\, h_p\, z_p \ , \qquad \text{(S18)}$$

where z_p is the penetration distance, h_p is the thickness of the paper pad, $S_{p,0}$ the cross section of the paper at the junction—there can be a sharp increase of section between the last channels of the tree and the pads— and β the cone semi-angle. In the case of a rectangular pad, $\beta = 0$. In the case of a cone, the wetted cross-section in the paper pad is assumed to have a perfectly rounded interface.

Successively substituting (S18) in (S17) and (S17) in (S16) yields the expression of the pressure P_j in function of V_p and z_p

$$P_j = \frac{p_0\, L_0}{\lambda_0 S_0}\, \mu\, \Sigma_n\, 2^n \phi V_p \left(\frac{S_{p,0}}{S_0} + \frac{2\beta\, h_p\, z_p}{S_0}\right) . \qquad \text{(S19)}$$

For simplifying the notations, let us note $a_n = 2^n \Sigma_n K \frac{p_0 L_0}{\lambda_0\ S_0}$, $\delta = \frac{S_0}{2\, \beta\, h_p}$ and $b = \frac{2K}{\mu\phi} P_{cap}$. The two first parameters a_n and δ have the dimension of a length, while the unit for *b* is mm^2/s. Substituting

(S19) in (S14), and using the relation $V_p = \frac{dz_p}{dt}$, produce the differential equation for the penetration distance z_p

$$\frac{d(z_p)^2}{dt}\left(1+\frac{a_n}{\delta}\right)+2a_n\,\frac{S_{p,0}}{S_0}\,\frac{dz_p}{dt}-b=0. \tag{S20}$$

The solution is

$$z_p=\frac{a_n}{\left(1+\frac{a_n}{\delta}\right)}\frac{S_{p,0}}{S_0}\left(-1+\sqrt{1+\left(\frac{S_0}{S_{p,0}}\right)^2\frac{b\left(1+\frac{a_n}{\delta}\right)\tau}{a_n^2}}\right)\;, \tag{S21}$$

where τ = *t* - *t_n* is the time taken from the entrance of the pad (τ = 0, z_p = 0). Note that, for rectangular pads, $\delta=\infty$, ($\frac{1}{\delta}=0$), and (S21) becomes

$$z_p=a_n\frac{S_{p,0}}{S_0}\left(-1+\sqrt{1+\left(\frac{S_0}{S_{p,0}}\right)^2\frac{b\,\tau}{a_n^2}}\right)\;. \tag{S22}$$

For rectangular pads, it is verified that, if the capillary pressure P_{cap} in the paper is very high (the parameter *b* is large), (S22) can be simplified, and the travel distance in the paper is $z_p \approx \sqrt{bt}=\sqrt{\frac{2K\,P_{cap}}{\mu\phi}t}$, which is simply the Lucas-Washburn law for paper alone, obtained by direct integration of (S14) with P_j = 0. In this case, the influence of the tree completely disappears.

In the general case, deriving (S21) in respect to time, the velocity of the fluid in the pad is

$$V_p=\frac{S_0}{S_{p,0}}\frac{b}{2a_n\sqrt{1+\left(\frac{S_0}{S_{p,0}}\right)^2\frac{b\left(1+\frac{a_n}{\delta}\right)\tau}{a_n^2}}}\;. \tag{S23}$$

Using the mass conservation equation (S17), the velocity in the root channel when the liquid wicks the paper is given by

$$V_{root} = 2^n V_p \phi \frac{S_p}{S_0} \; = \phi \left(\frac{S_{p,0}}{S_0} + \frac{z_p}{\delta} \right) \frac{S_0}{S_{p,0}} \frac{b}{2a_n \sqrt{1 + \left(\frac{S_0}{S_{p,0}} \right)^2 \frac{b\left(1 + \frac{a_n}{\delta}\right)\tau}{a_n^2}}} \quad , \tag{S24}$$

where z_p is given by (S21). At the precise time when the fluid contacts the pad (τ = 0, z_p = 0), relation (S24) yields $V_{root,0} = \frac{\phi\, b}{2a_n}$, and replacing a_n and b by their expressions, $\frac{P_{cap}}{\Sigma_n} = \frac{p_0 L_0}{S_0} \frac{\mu\, V_{root,0}}{\lambda_0}$, which is the expression of the pressure P_0 at the end of the root channel when the velocity is $V_{root,0}$.

Let us consider the case of conical pads. The penetration distance z_p can be removed from (S24) by using (S21)

$$V_{root} = \frac{2^{n-1}\phi\, b}{a_n} \frac{\left(\delta + a_n\sqrt{1 + D\tau}\right)}{(\delta + a_n)\sqrt{1 + D\tau}} \; , \tag{S25}$$

where $D = \left(\frac{S_0}{S_{p,0}} \right)^2 \frac{b\left(1 + \frac{a_n}{\delta}\right)}{a_n^2}$.

The unit of D is 1/s. In the case of rectangular pads, the derivation of V_{root} yields

$$V_{root} = \frac{2^{n-1}\phi\, b}{a_n} \frac{1}{\sqrt{1 + D_r\tau}} \; , \tag{S26}$$

where $D_r = \left(\frac{S_0}{S_{p,0}} \right)^2 \frac{b}{a_n^2}$

TABLE A4. Summary of coefficients used in the different solvents.

Coefficient	Unit	50% Isopropyl Alcohol	Nonanol	Pentanol
a	mm	0.0026	0.0026	0.0026
d	mm	1.6	1.6	1.6
a/ d	-	0.002	0.002	0.002
Sp_0/Sp	-	0.38	0.38	0.38
b	mm^2/s	3.7	1.8	2.0
Viscosity μ	mPa.s	3.2	11.2	3.75
Capillary pressure P_{cap}	Pa	2072	4116	4500
$2^n S_n$	-	11.34	11.34	11.34
Surface tension γ	mN/m	24	28.5	25.5
Contact angle θ	degrees	18	13	10
Cassie contact angle θ^*	degrees	55.5	52.0	51.1
Capillary force $\gamma \cos \theta^*$	mN/m	13.6	17.5	15.6
Washburn coefficient $\sqrt{\left(\frac{\gamma}{\mu}\right) 2\lambda \cos\theta^*}$	$mm/s^{1/2}$	47.0	28.5	38.7
Washburn coefficient from fit with experiments $\sqrt{\left(\frac{\gamma}{\mu}\right) 2\lambda \cos\theta^*}$	$mm/s^{1/2}$	38	25	40

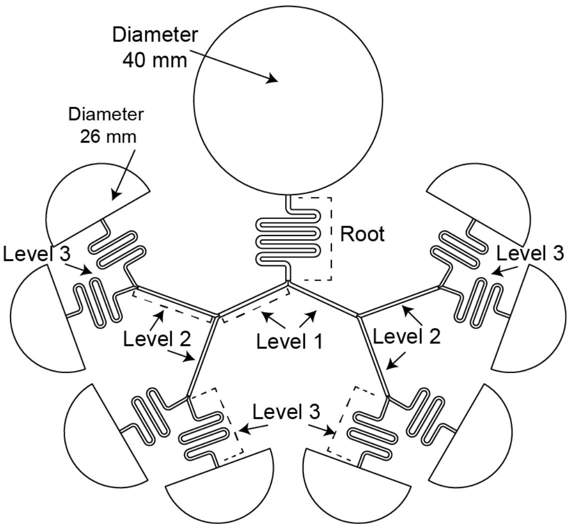

Level (L)	Length (mm)	Width (mm)	Depth (mm)
0 (root)	98.0	1.06	1.76
1	18.2	0.90	1.50
2	20.1	0.77	1.28
3	58.8	0.65	1.08

Figure A1. Engineering drawing of device with dimensions.

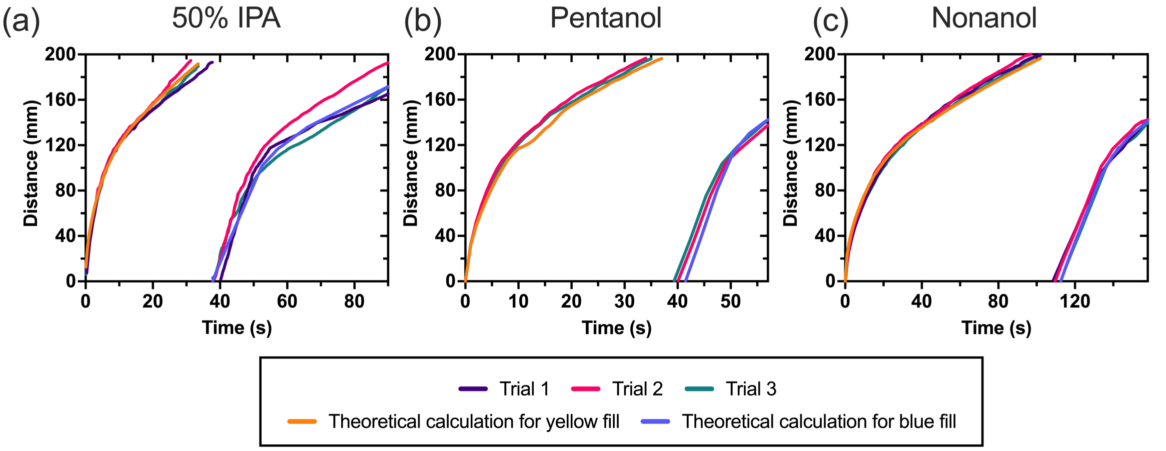

Figure A2. Raw data plots of all trials for (a) 50% (v/v) isopropyl alcohol (IPA), (b) pentanol, and (c) nonanol of distance traveled over time.

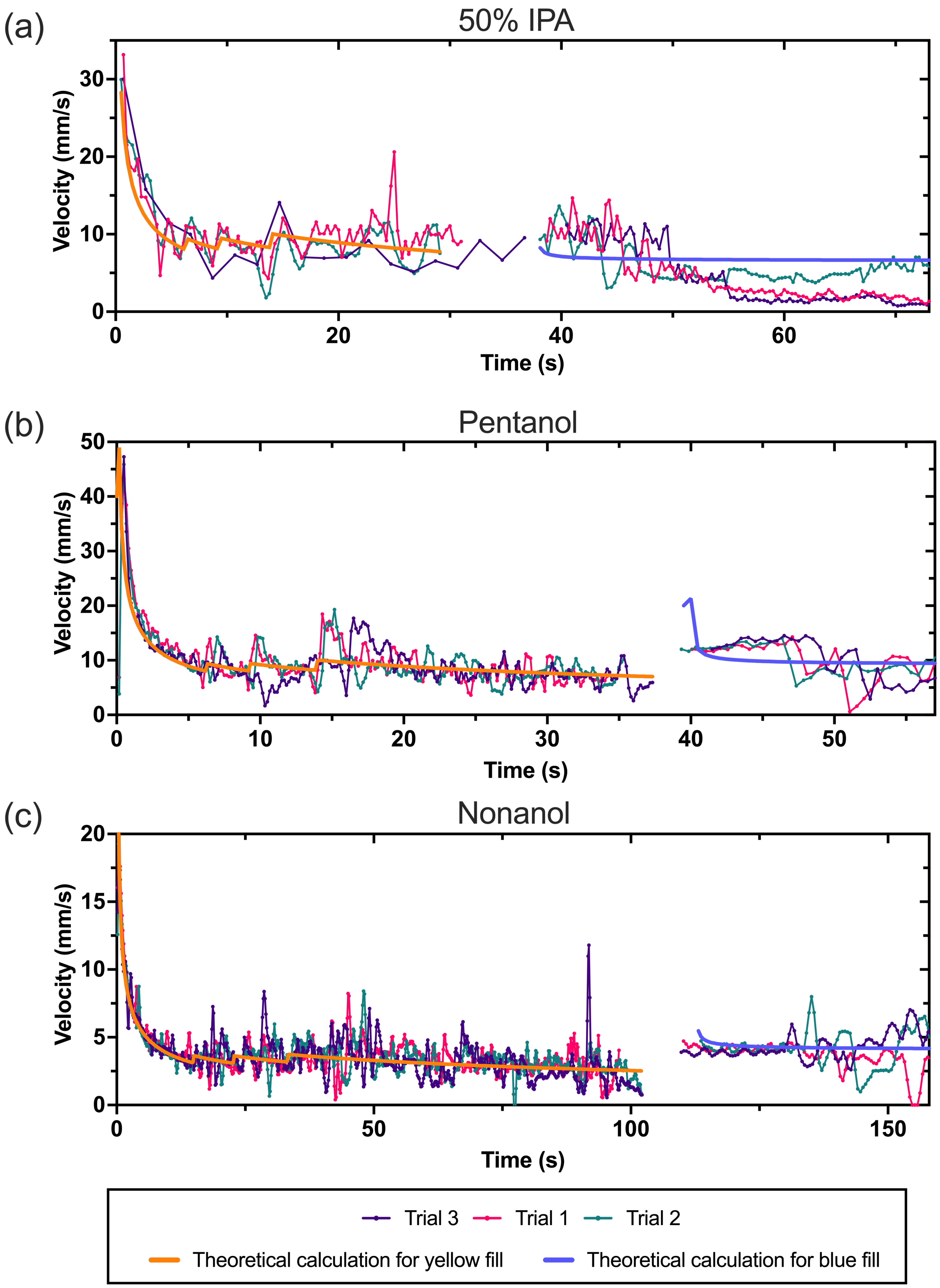

Figure A3. Raw data plot of all trials for (a) 50% (v/v) isopropyl alcohol (IPA), (b) pentanol, and (c) nonanol of velocity over time.

References

1. [1] Lee, J. J.; Berthier, J.; Theberge, A. B.; Berthier, E. Capillary Flow in Open Microgrooves: Bifurcations and Networks. *Langmuir* **2019**, *35* (32), 10667–10675.
2. Lee, J. J.; J. Berthier, J.; Kearney, K.E.; Berthier, E.; Theberge, A.B. Open-channel capillary trees and capillary pumping. Langmuir **2020**, *36*, 12795–12803.
3. Boodaghi, M.; Shamloo, A. A Comparison of Different Geometrical Elements to Model Fluid Wicking in Paper-Based Microfluidic Devices. *AIChE J.* **2020**, *66* (1), e16756.
4. Mohammad, A. A.; Alkhaldi, K. H. A. E.; AlTuwaim, M. S.; Al-Jimaz, A. S. Viscosity and Surface Tension of Binary Systems of N,N-Dimethylformamide with Alkan-1-Ols at Different Temperatures. *J. Chem. Thermodyn.* **2013**, *56*, 106–113.
5. Kim, S.; Thiessen, P. A.; Bolton, E. E.; Chen, J.; Fu, G.; Gindulyte, A.; Han, L.; He, J.; He, S.; Shoemaker, B. A.; Wang, J.; Yu, B.; Zhang, J.; Bryant, S. H. PubChem Substance and Compound Databases. *Nucleic Acids Res.* **2016**, *44* (Database issue), D1202–D1213.
6. Berthier, J.; Brakke, K. A.; Gosselin, D.; Bourdat, A. -g; Nonglaton, G.; Villard, N.; Laffite, G.; Boizot, F.; Costa, G.; Delapierre, G. Suspended Microflows between Vertical Parallel Walls. *Microfluid. Nanofluidics* **2015**, *18* (5–6), 919–929.
7. Lee, J. J.; Berthier, J.; Brakke, K. A.; Dostie, A. M.; Theberge, A. B.; Berthier, E. Droplet Behavior in Open Biphasic Microfluidics. *Langmuir* **2018**, *34* (18), 5358–5366.
8. Berthier, J.; Brakke, K. A.; Berthier, E. *Open Microfluidics*; Scrivener-Wiley Publishing, 2016.
9. Bosanquet, C. H. LV. On the Flow of Liquids into Capillary Tubes. *Lond. Edinb. Dubl. Phil. Mag.* **1923**, *45* (267), 525–531.
10. Quéré, D. Inertial Capillarity. *EPL* **1997**, *39* (5), 533.
11. Berthier, J.; Brakke, K. A.; Berthier, E. A General Condition for Spontaneous Capillary Flow in Uniform Cross-Section Microchannels. *Microfluid. Nanofluidics* **2014**, *16* (4), 779–785.
12. Mehrabian, H.; Gao, P.; Feng, J. J. Wicking Flow through Microchannels. *Phys. Fluids* **2011**, *23* (12), 122108.
13. Yang, D.; Krasowska, M.; Priest, C.; Popescu, M. N.; Ralston, J. Dynamics of Capillary-Driven Flow in Open Microchannels. *J. Phys. Chem. C* **2011**, *115* (38), 18761–18769.
14. Ouali, F. F.; McHale, G.; Javed, H.; Trabi, C.; Shirtcliffe, N. J.; Newton, M. I. Wetting Considerations in Capillary Rise and Imbibition in Closed Square Tubes and Open Rectangular Cross-Section Channels. *Microfluid. Nanofluid.* **2013**, *15* (3), 309–326.
15. Baret, J.-C.; Decré, M. M. J.; Herminghaus, S.; Seemann, R. Transport Dynamics in Open Microfluidic Grooves. *Langmuir* **2007**, *23* (9), 5200–5204.
16. Darcy, H. Les Fontaines Publiques de La Ville de Dijon. V. Dalmont, 1856.
17. Whitaker, S. Flow in Porous Media I: A Theoretical Derivation of Darcy's Law. *Transp. Porous Med.* **1986**, *1* (1), 3–25.
18. Amico, S. C.; Lekakou, C. Axial Impregnation of a Fiber Bundle. Part 1: Capillary Experiments. *Polym. Compos.* **2002**, *23* (2), 249–263.
19. Ashari, A.; Vahedi Tafreshi, H. General Capillary Pressure and Relative Permeability Expressions for Through-Plane Fluid Transport in Thin Fibrous Sheets. *Colloids Surf. A* **2009**, *346* (1), 114–122.
20. Dane, J. H.; Hofstee, C.; Corey, A. T. Simultaneous Measurement of Capillary Pressure, Saturation, and Effective Permeability of Immiscible Liquids in Porous Media. *Water Resour. Res.* **1998**, *34* (12), 3687–3692.
21. Babchin, A. J.; Bentsen, R.; Faybishenko, B.; Geilikman, M. B. On the Capillary Pressure Function in Porous Media Based on Relative Permeabilities of Two Immiscible Fluids: Application of Capillary Bundle Models and Validation Using Experimental Data. *Adv. Colloid Interface Sci.* **2016**, *233*, 176–185.

22. Zarandi, M. A. F.; Pillai, K. M.; Kimmel, A. S. Spontaneous Imbibition of Liquids in Glass-Fiber Wicks. Part I: Usefulness of a Sharp-Front Approach. *AIChE J.* **2018**, *64* (1), 294–305.

B. Appendix for Chapter 3

Reproduced in part from ***Tokihiro, J.C.;*** *McManamen, A.M.; Phan, D.N.; Thongpang, S.; Theberge, A.B.;*[#] *Berthier, J.*[#] *On the dynamic contact angle of capillary-driven microflows in open channels. Langmuir,* ***2024****, 40 (13), 7215-7224.*

[#]Co-corresponding authors

Section B1. Engineering drawings of open channels and experimental observation set-up

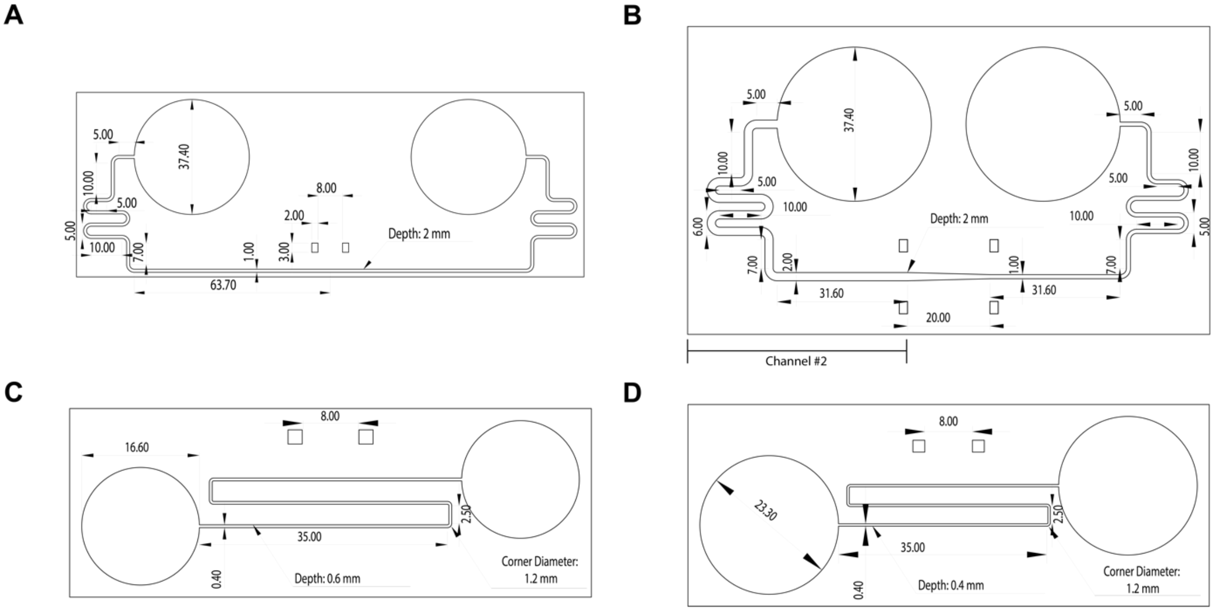

Figure B1. Engineering drawings for open microfluidic channels #1 (**A**), 2 (**B**), 3 (**C**), and 4 (**D**) with dimensions. Note: for the device shown in **B**, only the data resulting from the fluid flowing the left half of the device prior to the channel constriction were used in this manuscript.

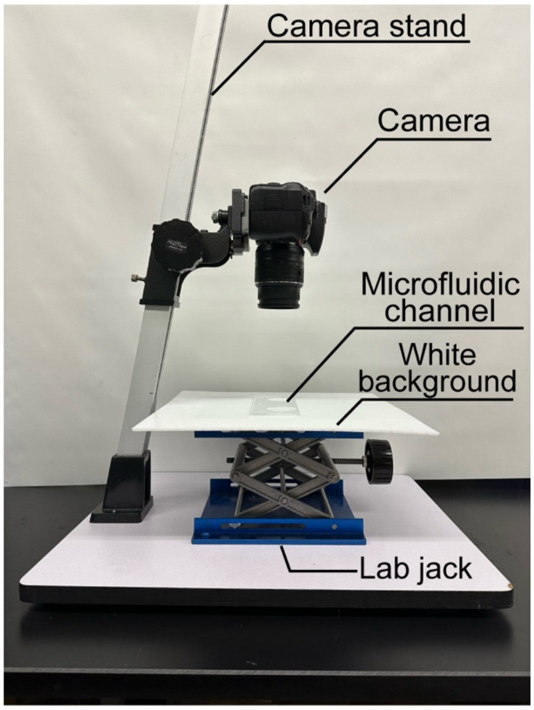

Figure B2. Set-up of DSLR camera and platform for experimental observation and data collection.

Section B1.2. Comparison between different models

In this section, we compare travel distances and velocities between four models (Lucas-Washburn-Rideal (LW), correlation of *Jiang et al.,* correlation of Bracke *et al.,* MKT approach) and experimental data.

A. Water in an open rectangular channel (w = 0.4 mm, h = 0.6 mm)

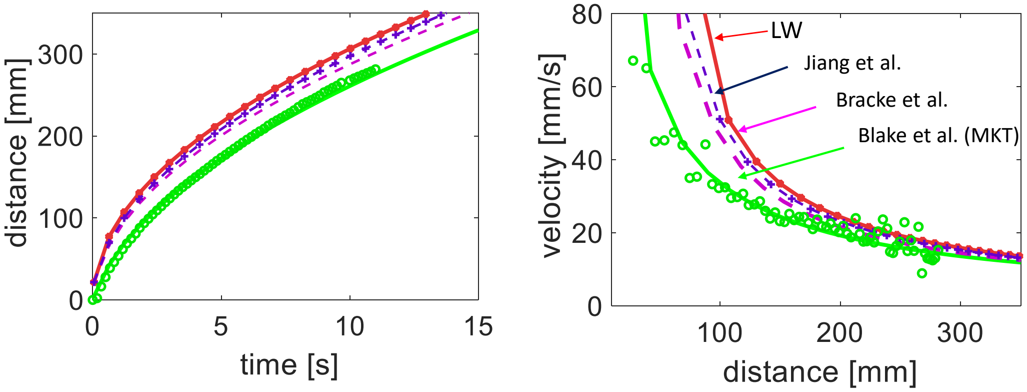

Figure B3. Left: travel distance vs. time; **right:** velocity vs. distance. Case of water. The dots correspond to the experiments. Note: The Lucas-Washburn-Rideal law is denoted as LW.

B. Chloroform in an open rectangular channel (w = 1 mm, h = 2 mm)

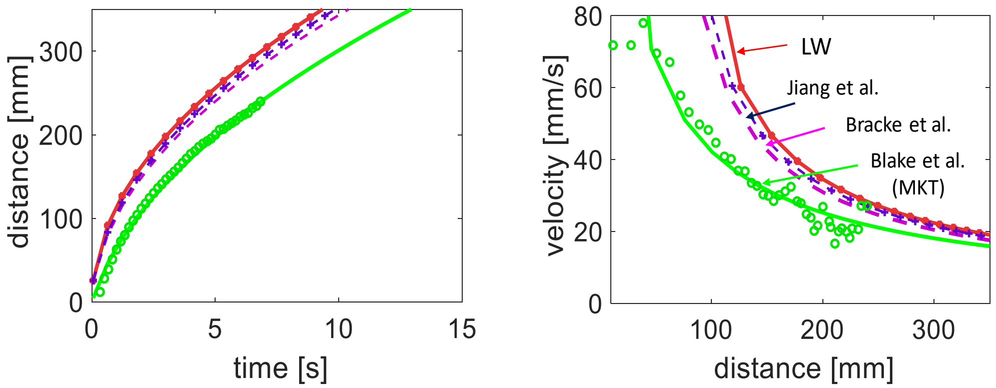

Figure B4. Left: travel distance vs. time; **right:** velocity vs. distance for the case of chloroform. Note: The Lucas-Washburn-Rideal law is denoted as LW.

C. 50% (v/v) isopropyl alcohol in an open rectangular channel (w = 1 mm, h = 2 mm)

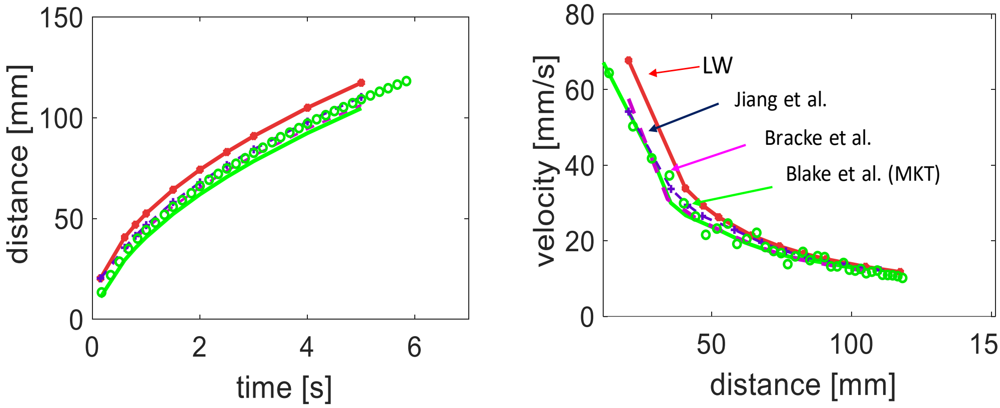

Figure B5. Left: travel distance vs. time; **right:** velocity vs. distance in the case of 50% (v/v) isopropyl alcohol. Note: The Lucas-Washburn-Rideal law is denoted as LW.

Section B2. Transition between inertial and viscous regimes in open channels

Let us first recall the Bosanquet equation for the capillary motion. In the case of an open capillary flow, the Bosanquet equation makes use of the generalized Cassie angle θ^*:

$$\rho\, S_C \frac{d\,(z\,\dot{z})}{dt} + \frac{\mu\, p\, z\, \dot{z}}{\bar{\lambda}} - p\,\gamma\, cos\theta^* = 0. \qquad \text{(SI.2.1)}$$

The cross-sectional area, S_c, is delimited by the wetted walls and the flat free surface (zero pressure). The term $\bar{\lambda}$ is average friction length. Let us note $a = \mu\, p / \bar{\lambda}\, \rho S_C$ (unit 1/s) and $b = p\gamma cos\theta^* / \rho S_C$ (unit m^2/s^2). The division of all the terms of (S1.2.1) by $\rho\, S_C$ yields:

$$\frac{d}{dt}\left(z\frac{dz}{dt}\right) = b - a\left(z\frac{dz}{dt}\right). \qquad \text{(SI.2.2)}$$

Assuming z = 0 at t = 0, time integration leads to the differential equation in z^2:

$$\frac{dz^2}{dt} + az^2 = 2bt. \qquad \text{(SI.2.3)}$$

A second integration yields the solution,

$$z^2 = \frac{2b}{a}\left[t - \frac{1}{a}(1 - e^{-at})\right]. \tag{SI.2.4}$$

The inertial regime occurs when the wall friction can be neglected at the beginning of the motion, so that (SI.2.3) becomes

$$\frac{dz^2}{dt} = 2bt. \tag{SI.2.5}$$

Time integration of (SI.2.5) yields

$$z = \sqrt{\frac{p\,\gamma\,cos\theta^*}{\rho\,S_C}}\;t = \sqrt{b}\,t. \tag{SI.2.6}$$

The inertial velocity $V_{in}$is then constant, leading to

$$V_{in} = \sqrt{\frac{p\,\gamma\,cos\theta^*}{\rho\,S_C}} = \sqrt{b}\,. \tag{SI.2.7}$$

The end of inertial regime occurs when the term $(1 - e^{-at})$ in (SI.4) becomes negligible, i.e. $t \sim\ 1/4a$. Then, the inertial-viscous transition time is

$$\tau_{inertial} \sim \frac{1}{4}\,\frac{\bar{\lambda}\,\rho\,S_C}{\mu\,p} = \frac{\bar{\lambda}\,\rho\,D_H}{16\,\mu}, \tag{SI.2.8}$$

where D_H is the hydraulic diameter defined by $D_H = 4\,\frac{S_c}{p}$. The travel distance at the end of inertial regime is then

$$z_{inertial} \simeq \sqrt{b}\,\tau_{inertial}\ . \tag{SI.2.9}$$

The inertial distance depends both on friction length and Cassie angle. The different values for the inertial times and inertial distances are listed in **Table B1**.

Table B1. Inertial times [ms] and distances [mm].

Liquids/channels	#1 t_{in} [ms]	#1 z_{in} [mm]	#2 t_{in} [ms]	#2 z_{in} [mm]	#3 t_{in} [ms]	#3 z_{in} [mm]	#4 t_{in} [ms]	#4 z_{in} [mm]
Pentanol	3.4	0.79	4.2	1.48	0.48	0.17	0.37	0.13
Nonanol	1.17	0.29	3.13	0.54	0.16	0.06	0.12	0.05
50% (v/v) Isopropyl Alcohol	0.49	0.35	1.33	0.66	0.70	0.08	0.52	0.06
FC-40	10.6	1.37	29.1	2.60	1.53	0.31	1.16	0.23
Chloroform	38.3	6.97	103.0	13.1	5.42	1.55	4.14	1.18
Dodecane	9.65	2.35	26.0	4.41	1.36	0.52	1.04	0.39
Toluene	22.7	5.42	61.2	10.19	3.21	1.20	2.45	0.91
Water	15.4	4.36	41.7	7.62	2.18	0.95	1.67	0.68

In **Figure B6**, we have indicated the values of the inertial distance in three open rectangular channels, and eight different liquids (including the six liquids that we use in this work). We remark that the dissociation of the Bosanquet equation for motion (SI.2.1) results in overestimated cutoff times. In reality, a progressive transition occurs between the two regimes.

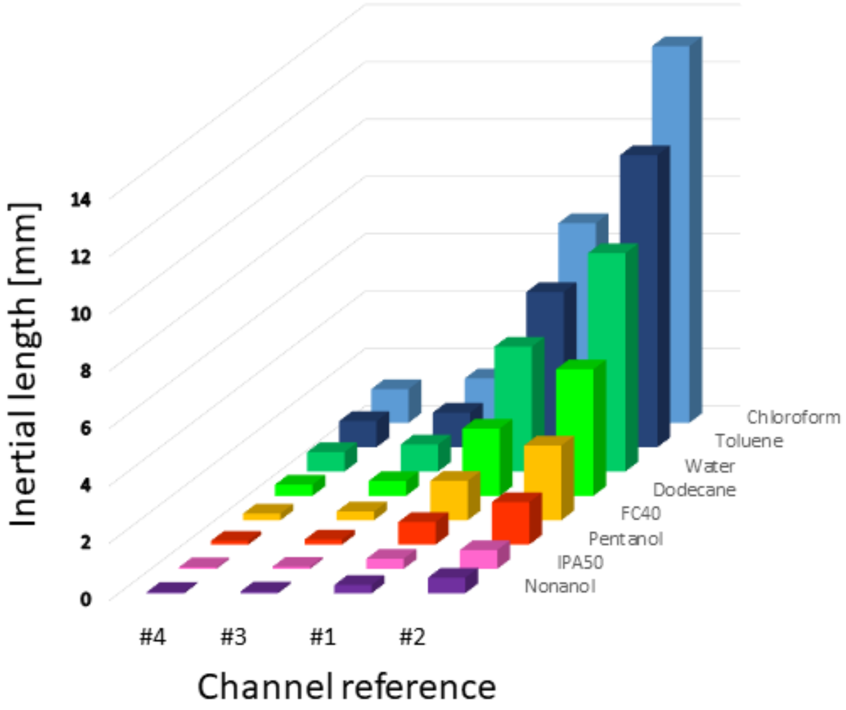

Figure B6. Different inertial distances for the four rectangular open-channels and eight liquids.

Section B3. Comparison with literature data for λ

The molecule volumes corresponding to the different molecules used in the study are obtained from tables of molar mass and listed in **Table B2**.

Table B2. Molecular volume of the different liquids

	Molar mass [g/mol]	Density [g/mL] @ 25°C	Molecular volume [nm^3]
Nonanol	144.3	0.830	0.29
Pentanol	88.2	0.815	0.18
50% (v/v) Isopropyl Alcohol	40.0	1.100	0.06
FC-40	650.0	1.850	0.59
Chloroform	119.0	1.483	0.13
Water	18.0	1.0	0.03

Inserting these molecular volumes, V_m, and the values of the coefficient, *z*, fitted on the experimental results in the MKT relation,

$$\frac{\zeta}{\mu} = \frac{V_m}{\lambda^3} \exp\left(\frac{W_a}{n\, k_B T}\right) \cong \frac{V_m}{\lambda^3} \exp\left(\frac{\lambda^2 W_a}{k_B T}\right), \tag{SI.3.1}$$

and we obtain the implicit relation linking λ, μ, and W_a:

$$ln\left(\frac{V_m}{\lambda^3}\right)\frac{\lambda^2 W_a}{k_B T} \cong ln\left(\frac{\zeta}{\mu}\right). \tag{SI.3.2}$$

The solution of (SI.3.2) is achieved by a numerical scheme. Equation (SI.3.2) can be written as:

$$\lambda^2 = \frac{k_B T}{W_a}\left\{ln\left(\frac{\zeta}{\mu}\right) - ln\left(\frac{V_m}{\lambda^3}\right)\right\} = \frac{k_B T}{W_a}\left\{ln\left(\frac{\zeta}{\mu}\right) - lnV_m + 3ln\lambda\right\}. \tag{SI.3.3}$$

Then, the iterative explicit approach is:

$$\lambda_{i+1}^2 = \frac{k_B T}{W_a}\left\{ln\left(\frac{\zeta}{\mu}\right) - ln\left(\frac{V_m}{\lambda^3}\right)\right\} = \frac{k_B T}{W_a}\left\{ln\left(\frac{\zeta}{\mu}\right) - lnV_m + 3ln\lambda_i\right\}, \tag{SI.3.4}$$

where *i* is the iteration index and produces the solution, λ. Convergence is rapidly obtained in less than 10 iterations. We obtain the values of λ listed in **Table B3**.

Table B3. Work of adhesion and average distances of molecule displacement

	Molecular volume [nm^3]	W_a [mN/m]	λ [nm]
Nonanol	0.29	57.1	0.30
Pentanol	0.18	54.6	0.45
50% (v/v) Isopropyl Alcohol	0.06	62.4	0.56
FC-40	0.59	31.3	0.61
Chloroform	0.13	53.1	0.52
Water #1	0.03	116.6	0.49
Water #2	0.03	113.7	0.50
Water #3	0.03	113.7	0.50
Water #4	0.03	110.7	0.51
Water #5	0.03	101.0	0.54

We can compare these values of λ with the data found in the literature and collated by Duvivier, Blake and De Coninck in reference 1. In **Figure B7**, we observe that the values of the average distance of each displacement λ are located precisely in the cloud of data collated in the literature.

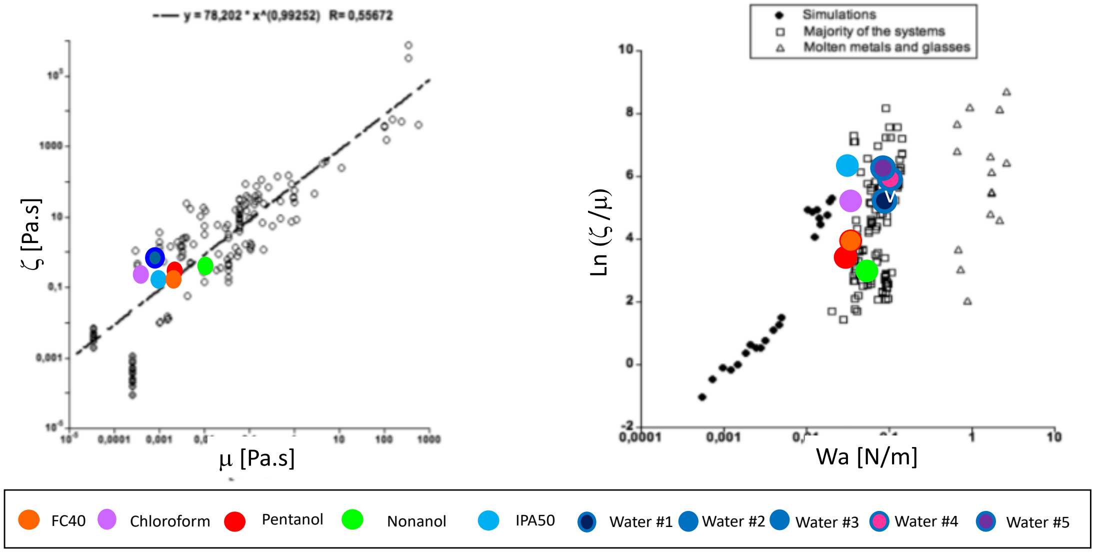

Figure B7. Left: coefficient of line friction vs. fluid viscosity; **right:** ln(ζ/η) vs. work of adhesion (Wa). The black symbols (circles, diamonds, triangles) correspond to literature data extracted from reference 1. Adapted with permission from D. Duvivier, T.D. Blake, J. De Coninck 2013 Toward a predictive theory of wetting dynamics, *Langmuir* **29**(32),10132-10140. Copyright 2023 American Chemical Society. Note: 50% (v/v) aqueous isopropyl alcohol is denoted as IPA50.

References

1. Duvivier, D.; Blake, T. D.; De Coninck, J. Toward a Predictive Theory of Wetting Dynamics. *Langmuir* **2013**, *29* (32), 10132–10140.
2. Li, H.; Sedev, R.; Ralston, J. Dynamic Wetting of a Fluoropolymer Surface by Ionic Liquids. *Phys. Chem. Chem. Phys.* **2011**, *13* (9), 3952–3959.
3. Blake, T.D., De Coninck, J. 2011 Dynamics of wetting and Kramers' theory. *Eur. Phys. J. Spec. Top.* 197, 249-264.
4. Blake, T. D.; De Coninck, J. Dynamics of Wetting and Kramers' Theory. *Eur. Phys. J. Spec. Top.* **2011**, *197* (1), 249.
5. Duvivier, D.; Seveno, D.; Rioboo, R.; Blake, T. D.; De Coninck, J. Experimental Evidence of the Role of Viscosity in the Molecular Kinetic Theory of Dynamic Wetting. *Langmuir* **2011**, *27* (21), 13015–13021.
6. Vega, M. J.; Gouttière, C.; Seveno, D.; Blake, T. D.; Voué, M.; De Coninck, J.; Clarke, A. Experimental Investigation of the Link between Static and Dynamic Wetting by Forced Wetting of Nylon Filament. *Langmuir* **2007**, *23* (21), 10628–10634.
7. Semal, S.; Bauthier, C.; Voué, M.; Vanden Eynde, J. J.; Gouttebaron, R.; De Coninck, J. Spontaneous Spreading of Liquid Droplets on Mixed Alkanethiol Monolayers: Dynamics of Wetting and Wetting Transition. *J. Phys. Chem. B* **2000**, *104* (26), 6225–6232.
8. Stalcup, E. J.; Seemann, R.; Herminghaus, S.; Law, B. M. Dissipation Mechanisms in Ionic Liquids. *J. Colloid Interface Sci.* **2009**, *338* (2), 523–528.
9. Vega, M.-J.; Seveno, D.; Lemaur, G.; Adão, M.-H.; De Coninck, J. Dynamics of the Rise around a Fiber: Experimental Evidence of the Existence of Several Time Scales. *Langmuir* **2005**, *21* (21), 9584–9590.

10. Saiz, E.; Tomsia, A. P.; Rauch, N.; Scheu, C.; Ruehle, M.; Benhassine, M.; Seveno, D.; De Coninck, J.; Lopez-Esteban, S. Nonreactive Spreading at High Temperature: Molten Metals and Oxides on Molybdenum. *Phys. Rev. E* **2007**, *76* (4), 041602.
11. Brooks, C. F.; Grillet, A. M.; Emerson, J. A. Experimental Investigation of the Spontaneous Wetting of Polymers and Polymer Blends. *Langmuir* **2006**, *22* (24), 9928–9941.
12. de Ruijter, M. J.; De Coninck, J.; Blake, T. D.; Clarke, A.; Rankin, A. Contact Angle Relaxation during the Spreading of Partially Wetting Drops. *Langmuir* **1997**, *13* (26), 7293–7298.
13. Goossens, S.; Seveno, D.; Rioboo, R.; Vaillant, A.; Conti, J.; De Coninck, J. Can We Predict the Spreading of a Two-Liquid System from the Spreading of the Corresponding Liquid–Air Systems? *Langmuir* **2011**, *27* (16), 9866–9872.
14. Inverarity, G. Dynamic Wetting of Glass Fibre and Polymer Fibre. *Br. Polym. J.* **1969**, *1* (6), 245–251.
15. Hoffman, R. L. A Study of the Advancing Interface. I. Interface Shape in Liquid—Gas Systems. *J. Colloid Interface Sci.* **1975**, *50* (2), 228–241.
16. Schwartz, A. M.; Tejada, S. B. Studies of Dynamic Contact Angles on Solids. *J. Colloid Interface Sci.* **1972**, *38* (2), 359–375.
17. Ström, G.; Fredriksson, M.; Stenius, P.; Radoev, B. Kinetics of Steady-State Wetting. *J. Colloid Interface Sci.* **1990**, *134* (1), 107–116.

C. Appendix for Chapter 4

Reproduced in part from ***Tokihiro, J.C.;*** *Robertson, I.H.; Gregucci, D.; Shin, A.; Michelini, E.; Nicholson, T.M.; Olanrewaju, A.; Theberge, A.B.;# Berthier, J.;# Berthier, E.# The dynamics of capillary flow in an open-system featuring trigger valves. Scientific Reports,* ***2024****, 14, 31732.*
#Co-corresponding authors

Section C1. Model for the dynamics of the flow in an open-channel with multi trigger valves

1. Geometry

A sketch of the device we are considering here is shown in **Figure C1**. The valves can be placed on the same side of the channel or on both sides. The type of arrangement does not change the dynamics of the flow (in the case of miscible liquids), but it changes the arrangement of the stream tubes. In this Appendix, we only analyze the dynamic of the flow.

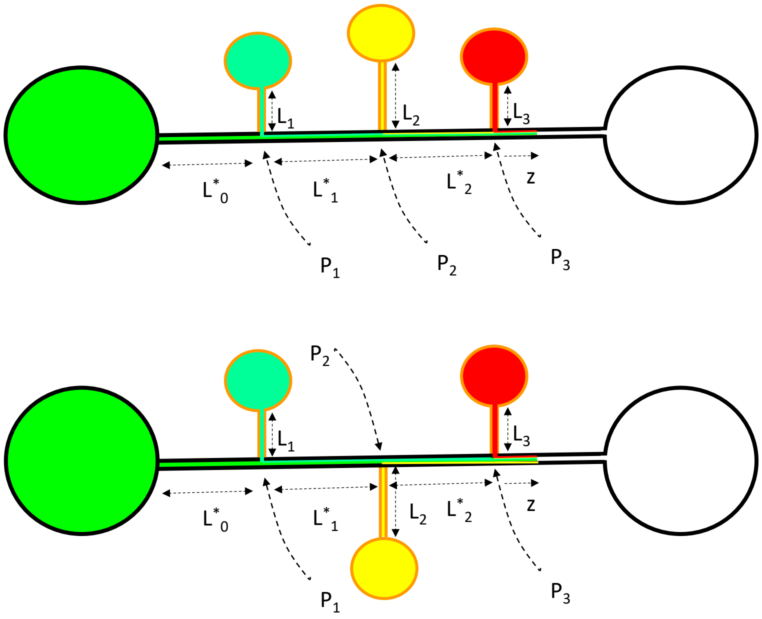

Figure C1. Sketch of the main channel with the trigger valves.

2. Notations

The notations used in this section are listed in **Table C1**.

Table C1. Notations.

Name	notation	unit	Remarks/References
Length	L_i	mm	Lengths of side channels
Length	L^*_i	mm	Lengths between two nodes in the main channel
Width	$w^*=w_0$	mm	Width of main channel (uniform)
Width	w_i	mm	Widths of side channels
Depth	$h^*=h_0$	mm	Depth of main channel (uniform)
Depth	h_i	mm	Depths of side channels
Cross-sectional area	$S^*=S_0$	mm^2	Main channel (uniform)
Cross-sectional area	S_i	mm^2	side channels
Average friction length	$\bar{\lambda}_\iota^*=l_0$	mm	Main channel (uniform)[1]
Average friction length	$\bar{\lambda}_\iota$	mm	Side channel[1]
Perimeter (total)	$p^*=p_i$	mm	Main channel (uniform)
Perimeter (total)	p_i	mm	Side channel, Includes free perimeter
Perimeter (wetted)	$p_w^*=p_{W,0}$	mm	Main channel, only wetted part
Perimeter (wetted)	$p_{W,i}$	mm	Side channel, only wetted part
Viscosity (dynamic)	μ	mPa.s	[for nonanol
Surface tension	γ	mN/m	for nonanol
Contact angle	θ	rad	Static contact angle
Generalized Cassie angle	θ^*_i	rad	Generalized Cassie angle for open channels
Contact angle	θ_d	rad	Dynamic contact angle
Pressure	P	mPa	Pressure at the nodes
Capillary pressure	P_{cap}	mPa	Laplace pressure of the meniscus
Velocity	V_i	mm/s	Averaged in a cross section (side channels)
Velocity	V_i^*	mm/s	Averaged in a cross section (main channel)
Travel distance	z	mm	Middle of advancing meniscus
Coefficient of TCL friction	z	Pa.s	MKT approach [2]
Geometrical coefficient	A_i	mm^3	Side channel
Geometrical coefficient	A^*	mm^3	Main channel
Auxiliary geometrical coefficient	B_i	mm^3	Node coefficients

3. *Inlet main channel*

The first part of the flow occurs in the inlet channel, before the first trigger valve. In the case of nonanol—which presents a relatively high viscosity—, the duration of the inertial regime is very short, less than 10 ms[3–5], and the length of the channel affected by the initial inertial regime is less than 1 to 2 mm. So, we consider here only the viscous regime, described by Lucas, Washburn and Rideal (LWR law) in the years 1928-1930[2, 6–8] and recently generalized to arbitrary channels[1, 9–11]

$$z_0(t) = \sqrt{\frac{\gamma}{\mu} 2\bar{\lambda}_0 \, cos \, \theta_0^* \; t}, \tag{SI1.1}$$

where t is the time (t=0, z=0), and θ_0^* is the so-called generalized Cassie angle[12] given by the relation

$$cos \, \theta_0^* = \frac{p_W}{p} \cos \theta_0 - \frac{p_F}{p}, \tag{SI1.2}$$

where p_W and p_F are respectively the wetted and free perimeter in a cross section. For a rectangular channel, $p_W=2h+w$ and $p_F=w$. A correction may be done to the preceding relation at the channel inlet where the fluid velocity is still high (even in the viscous regime). A dynamic contact angle (DCA) should be taken into account. It has been shown that in open channel geometry the molecular kinetic theory (MKT) provides an accurate value for the DCA.[5, 13–16]

The correction for the DCA is

$$cos \, \theta_{d,0} = \cos\theta_0 - \frac{\zeta}{\gamma} \, V \tag{SI1.3}$$

where ζ is the coefficient of triple contact line (TPL) friction. This expression modifies the generalized Cassie angle

$$cos \, \theta_{d,0}^* = \frac{p_W}{p} \cos \theta_{d,0} - \frac{p_F}{p} = \left(\frac{p_W}{p} cos \, \theta_0 - \frac{p_F}{p}\right) - \frac{p_W}{p} \frac{\zeta}{\gamma} \, V = cos \, \theta_0^* - \frac{p_W}{p} \frac{\zeta}{\gamma} \, V \tag{SI1.4}$$

The generalized LWR law is then[4]

$$z = -\bar{\lambda}_0 \frac{p_{w,0}}{p_0} \frac{\zeta}{\mu} + \sqrt{\left(\bar{\lambda}_0 \frac{p_{w,0}}{p_0} \frac{\zeta}{\mu}\right)^2 + z_0^2(t)} \, . \tag{SI1.5}$$

The front meniscus reaches the first TGV at the time t_0 determined by

$$t_0 = \frac{\left(L_0^* + \bar{\lambda}_0 \frac{p_{w,0}\,\zeta}{p_0\ \mu}\right)^2 - \left(\bar{\lambda}_0 \frac{p_{w,0}\,\zeta}{p_0\ \mu}\right)^2}{\frac{\gamma}{\mu} 2\bar{\lambda}_0 \cos\theta_{d,0}^*}\ . \tag{SI1.6}$$

4. *First trigger valve*

A sketch of the flow after the first trigger valve (and before the second TGV) is shown in Figure C2. It is assumed here that the first TGV is far enough from inlet reservoir to neglect the dynamic contact angle. There is a very short inertial burst when a TGV opens, but it is evanescent and we don't take it into account here.

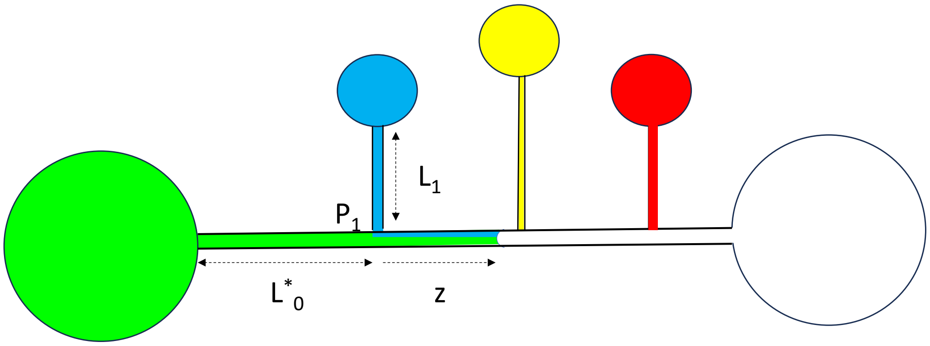

Figure C2. Sketch of the device with the advancing meniscus between the first and second TG. The "*" characterizes the main channel, while the side channels are noted *i*=1,…n.

The pressure P_1 may be expressed by the two relations [4]

$$P_1 = \frac{L_1\, p_1}{S_1}\ \mu \frac{V_1}{\bar{\lambda}_1} = \ \mu \frac{S_1 V_1}{A_1}, \tag{SI1.7}$$

considering the side channel #1, where $A_1 = \frac{\bar{\lambda}_1 S_1^2}{L_1\, p_1}$, and

$$P_1 = \frac{L_0^*\, p_0}{S_0}\ \mu \frac{V_0^*}{\bar{\lambda}_0} = \ \mu \frac{S_0 V_0^*}{A_0^*}, \tag{SI1.8}$$

considering the main channel (index 0), where $A_0^* = \frac{\bar{\lambda}_0 S_0^2}{L_0^* \, p_0}$. The mass conservation equation yields the relation

$$S_0 V_1^* = S_0 V_0^* + S_1 V_1. \qquad \text{(SI1.9)}$$

Multiplying (SI1.7) by *S₁* and (SI1.8) by *S₀*, adding the result and using (SI1.9) leads to

$$S_0 V_1^* = S_0 V_0^* + S_1 V_1 = \frac{P_1}{\mu} \, (A_0^* + A_1) \, . \qquad \text{(SI1.10)}$$

Let us denote $B_0 = A_0^* = \frac{\bar{\lambda}_0 S_0^2}{L_0^* \, p_0}$. The pressure *P₁* is then given by

$$P_1 = \mu \frac{S_0 V_1^*}{(B_0 + A_1)} = \mu \frac{Q_1^*}{(B_0 + A_1)} \ , \qquad \text{(SI1.11)}$$

where Q_1^* is the volumetric flow rate in the main channel after the first TGV. In the viscous regime, the equation for the fluid motion is given by the balance between capillary pressure and pressure drop. If *z* denotes the distance taken from the first node (first TGV), we have

$$P_{cap} = \frac{\gamma \, p_0 \cos \theta_0^*}{S_0} = \frac{z \, p_0}{S_0} \mu \, \frac{V_1^*}{\bar{\lambda}_0} + P_1 = \frac{z \, p_0}{S_0} \mu \, \frac{V_1^*}{\bar{\lambda}_0} + \mu \frac{S_0 V_1^*}{(B_0 + A_1)} = \mu \frac{z}{L_0^*} \, \frac{S_0 V_1^*}{A_0^*} + \mu \frac{S_0 V_1^*}{(B_0 + A_1)}. \qquad \text{(SI1.12)}$$

Inserting $V_1^* = dz/dt$ in (SI1.12) produces the differential equation

$$\frac{1}{2} \, \frac{1}{L_0^* A_0^*} \frac{dz^2}{dt} + \frac{1}{(B_0 + A_1)} \frac{dz}{dt} - \frac{\gamma}{\mu} \frac{p_0}{S_0^2} \cos \theta_0^* = 0 \ , \qquad \text{(SI1.13)}$$

or,

$$\frac{dz^2}{dt} + 2 \frac{L_0^* A_0^*}{(B_0 + A_1)} \frac{dz}{dt} - \frac{\gamma}{\mu} 2 \bar{\lambda}_0 \cos \theta_0^* = 0 \ . \qquad \text{(SI1.14)}$$

Remarking that the travel distance in the main channel without TGVs is $z_0 = \sqrt{\frac{\gamma}{\mu} 2\bar{\lambda}_0 \cos\theta_0^* \, \tau_1}$, where τ_1 is the time taken after the passage of the first TGV ($\tau_1 = t - t_0$), integration of (SI1.14) leads to the solution

$$z = -\frac{L_0^* A_0^*}{(B_0 + A_1)} + \sqrt{\left[\frac{L_0^* A_0^*}{(B_0 + A_1)}\right]^2 + z_0^2} \, . \tag{SI1.15}$$

At the time *t₁*, the front meniscus reaches the second TGV. This time is given by

$$t_1 = \frac{\left(L_1^* + \frac{L_0^* A_0^*}{(B_0 + A_1)}\right)^2 - \left(\frac{L_0^* A_0^*}{(B_0 + A_1)}\right)^2}{\frac{\gamma}{\mu} 2\bar{\lambda}_0 \cos\theta_0^*} + t_0 = \frac{L_1^{*2} + \frac{2 L_1^* L_0^* A_0^*}{(B_0 + A_1)}}{\frac{\gamma}{\mu} 2\bar{\lambda}_0 \cos\theta_0^*} + t_0 . \tag{SI1.16}$$

In the case of the main channel alone—without any TGV— the geometrical coefficient *A₁*=0, and relation (SI1.16) reduces to $t_1 = \frac{(L_1^* + L_0^*)^2}{\frac{\gamma}{\mu} 2\bar{\lambda}_0 \cos\theta_0^*}$, which is the generalized LWR expression.

5. *Second trigger valve*

Let us now express the pressure *P₂*. On one hand,

$$P_2 = \frac{L_2 \, p_2}{S_2} \, \mu \frac{V_2}{\bar{\lambda}_2} = \mu \frac{S_2 V_2}{A_2} = \mu \frac{Q_2}{A_2}, \tag{SI1.17}$$

considering the side channel #2. Considering the main channel

$$P_2 = P_1 + \frac{L_1^* p_0}{S_0} \, \mu \frac{V_1^*}{\bar{\lambda}_0} = P_1 + \mu \frac{S_0 V_1^*}{A_1^*} = P_1 + \mu \frac{Q_1^*}{A_1^*}, \tag{SI1.18}$$

where $A_1^* = \frac{\bar{\lambda}_0 S_0^2}{L_1^* p_0}$. Substituting (SI1.11) in (SI1.18) yields

$$P_2 = \mu \frac{S_0 V_1^*}{(B_0 + A_1)} + \mu \frac{S_0 V_1^*}{A_1^*} = \mu S_0 V_1^* \left[\frac{1}{(B_0 + A_1)} + \frac{1}{A_1^*}\right] = \mu \frac{S_0 V_1^*}{B_1} \, , \tag{SI1.19}$$

where $B_1 = \frac{1}{\left[\frac{1}{(B_0+A_1)}+\frac{1}{A_1^*}\right]}$. Remembering that the mass conservation equation at node 2 is

$$S_0 V_2^* = S_0 V_1^* + S_2 V_2 = S_0 V_0^* + S_1 V_1 + S_2 V_2 \ , \tag{SI1.20}$$

and adding (SI1.17) and (SI1.19)

$$S_0 V_2^* = S_0 V_1^* + S_2 V_2 = \frac{P_2}{\mu} B_1 + \frac{P_2}{\mu} A_2 = \frac{P_2}{\mu} (A_2 + B_1). \tag{SI1.21}$$

Again, the equation for the fluid motion is given by the balance between capillary pressure and pressure drop

$$P_{cap} = \frac{\gamma\, p_0 \cos\theta_0^*}{S_0} = \frac{z\, p_0}{S_0} \mu \frac{V_2^*}{\bar{\lambda}_0} + P_2 = \frac{z}{L_0^*} \mu \frac{S_0 V_2^*}{A_0^*} + \mu \frac{S_0 V_2^*}{(A_2+B_1)}. \tag{SI1. 22}$$

Remembering that $V_2^* = dz/dt$, we obtain the differential equation

$$\frac{1}{2\, L_0^* A_0^*} \frac{dz^2}{dt} + \frac{1}{(A_2+B_1)} \frac{dz}{dt} - \frac{\gamma}{\mu} \frac{p_0}{S_0^2} \cos\theta_0^* = 0 \ , \tag{SI1.23}$$

Still using the travel distance in the main channel without TGV; $z_0 = \sqrt{\frac{\gamma}{\mu} 2\bar{\lambda}_0 \cos\theta_0^* \tau_2}$, where τ_2 is the time taken after the passage of the second TGV ($\tau_2 = t - t_1$), integration of (SI1.23) leads to the solution

$$z = -\frac{L_0^* A_0^*}{(A_2+B_1)} + \sqrt{\left[\frac{L_0^* A_0^*}{(A_2+B_1)}\right]^2 + z_0^2} \ . \tag{SI1.24}$$

The same approach as precedingly produces the time t_2 when the meniscus reaches the third TGV

$$t_2 = \frac{\left(L_2^* + \frac{L_0^* A_0^*}{(A_2+B_1)}\right)^2 - \left(\frac{L_0^* A_0^*}{A_2+B_1}\right)^2}{\frac{\gamma}{\mu} 2\bar{\lambda}_0 \cos\theta_0^*} + t_1 = \frac{L_2^{*2} + \frac{2L_2^*\, L_0^* A_0^*}{(A_2+B_1)}}{\frac{\gamma}{\mu} 2\bar{\lambda}_0 \cos\theta_0^*} + t_1 \ . \tag{SI1.25}$$

6. *Third trigger valve*

The pressure *P_3* is obtained similarly

$$P_3 = \frac{L_3\, p_3}{S_3}\, \mu \frac{V_3}{\bar{\lambda}_3} = \mu \frac{S_3 V_3}{A_3} = \mu \frac{Q_3}{A_3}, \tag{SI1.26}$$

considering the side channel #3, and considering the main channel

$$P_3 = P_2 + \frac{L_2^*\, p_0}{S_0}\, \mu \frac{V_2^*}{\bar{\lambda}_0} = P_2 + \mu \frac{S_0 V_2^*}{A_2^*}\ , \tag{SI1.27}$$

where $A_2^* = \frac{\bar{\lambda}_0 S_0^2}{L_2^*\, p_0}$. Substituting (SI1.21) in (SI1.27) yields

$$P_3 = \mu \frac{S_0 V_2^*}{(A_2+B_1)} + \mu \frac{S_0 V_2^*}{A_2^*} = \mu\, S_0 V_2^* \left\{\frac{1}{(A_2+B_1)} + \frac{1}{A_2^*}\right\} = \frac{\mu\, S_0 V_2^*}{B_2}\ , \tag{SI1.28}$$

where $B_2 = \frac{1}{\left[\frac{1}{(B_1+A_2)}+\frac{1}{A_2^*}\right]}$. Remembering that the mass conservation equation at node 3 is

$$S_0 V_3^* = S_0 V_2^* + S_3 V_3 = S_0 V_0^* + \textstyle\sum_{i=1,3} S_i V_i\ , \tag{SI1.29}$$

and adding (SI1.26) and (SI1.28)

$$S_0 V_3^* = S_0 V_2^* + S_3 V_3 = \frac{P_3}{\mu}\, B_2 + \frac{P_3}{\mu} A_3 = \frac{P_3}{\mu}\, (A_3 + B_2), \tag{SI1.30}$$

Finally, considering the part of the main channel where the front meniscus is advancing, the capillary pressure balances the pressure drop

$$P_{cap} = \frac{\gamma\, p_0 \cos\theta_0^*}{S_0} = \frac{z\, p_0}{S_0} \mu\, \frac{V_3^*}{\bar{\lambda}_0} + P_3 = \mu \frac{z}{L_0^*}\, \frac{S_0 V_3^*}{A_0^*} + \mu \frac{S_0 V_3^*}{(A_3+B_2)}. \tag{SI1.31}$$

Substituting $V_3^* = dz/dt$ in (SI1.31) yields the differential equation

$$\frac{1}{2L_0^* A_0^*}\, \frac{dz^2}{dt} + \frac{1}{(A_3+B_2)} \frac{dz}{dt} - \frac{\gamma}{\mu} \frac{p_0}{S_0^2} \cos\theta_0^* = 0\ , \tag{SI1.32}$$

Still using the travel distance in the main channel without TGVs $z_0 = \sqrt{\frac{\gamma}{\mu} 2\bar{\lambda}_0 \cos\theta_0^* \tau_3}$, where τ_3 is the time taken after the passage of the third TG ($\tau_3 = t - t_2$), integration of (SI1.32) leads to the solution

$$z = -\frac{L_0^* A_0^*}{(A_3+B_2)} + \sqrt{\left[\frac{L_0^* A_0^*}{A_3+B_2}\right]^2 + z_0^2}\ . \tag{SI1.33}$$

7. Generalization

The travel distance of the front meniscus is given by the recurrence relation

$$z = -\frac{L_0^* A_0^*}{(A_n+B_{n-1})} + \sqrt{\left[\frac{L_0^* A_0^*}{A_n+B_{n-1}}\right]^2 + \frac{\gamma}{\mu} 2\bar{\lambda}_0 \cos\theta_0^* (t - t_{n-1})}\ , \tag{SI1.34}$$

where $A_n = \frac{\bar{\lambda}_n S_n^2}{L_n p_n}$ and $B_0 = A_0^* = \frac{\bar{\lambda}_0 S_0^2}{L_0^*\, p_0}$, $B_1 = \frac{1}{\left[\frac{1}{(B0+A_1)} + \frac{1}{A_1^*}\right]}$, and for all *n*: $B_n = \frac{1}{\left[\frac{1}{(B_{n-1}+A_n)} + \frac{1}{A_n^*}\right]}$. On the other hand,

the times when the meniscus reaches a TGV is

$$t_n = \frac{L_n^{*2} + \frac{2 L_n^* L_0^* A_0^*}{p_0 (A_n + B_{n-1})}}{\frac{\gamma}{\mu} 2\bar{\lambda}_0 \cos\theta_0^*} + t_{n-1}\ . \tag{SI1.35}$$

Finally, the general expression of the velocity of the front meniscus is

$$V = \frac{1}{2} \frac{\frac{\gamma}{\mu} 2\bar{\lambda}_0 \cos\theta_0^*}{\sqrt{\left[\frac{L_0^* A_0^*}{B_{n-1}+A_n}\right]^2 + \frac{\gamma}{\mu} 2\bar{\lambda}_0 \cos\theta_0^* (t - t_{n-1})}} = \tilde{V}_0 \frac{\tilde{z}_0}{z + \frac{L_0^* A_0^*}{(A_n+B_{n-1})}}, \tag{SI1.36}$$

where $\tilde{z}_0 = \sqrt{\frac{\gamma}{\mu} 2\bar{\lambda}_0\, cos\, \theta_0^*\ t}$ and $\tilde{V}_0 = \frac{\frac{\gamma}{\mu} 2\bar{\lambda}_0 \cos\theta_0^*}{\tilde{z}_0}$, corresponding to the main channel without TGVs.

Section C2. Influence of the length of the side channel

In this section, we investigate the effect of the side channel length on the flow after the TGV. The liquid is nonanol and the characteristic dimensions are listed in Table C2.

Table C2. Channel dimensions.

Inlet channel	Side channel #1	Side channel #2	Side channel #3
L_0= 80 mm	L_1 = 2 mm	L_1 = 8 mm	L_1 = 80 mm
w_0 = 1mm	w_1 = 0.4 mm	w_1 = 0.4 mm	w_1 = 0.4 mm
h_0=1mm	h_1 = 0.6 mm	h_1 = 0.6 mm	h_1 = 0.6 mm

The results obtained using the model are shown in Figure C3. A short side channel ($L_1 << L_0$) produces a jump of the velocity at the TGV, as shown by the green line in Figure C3. This jump decreases when the length of the side channel increases. When the two upstream lengths are equal ($L_1 = L_0$), the jump disappears, as shown by the purple line in Figure C3.

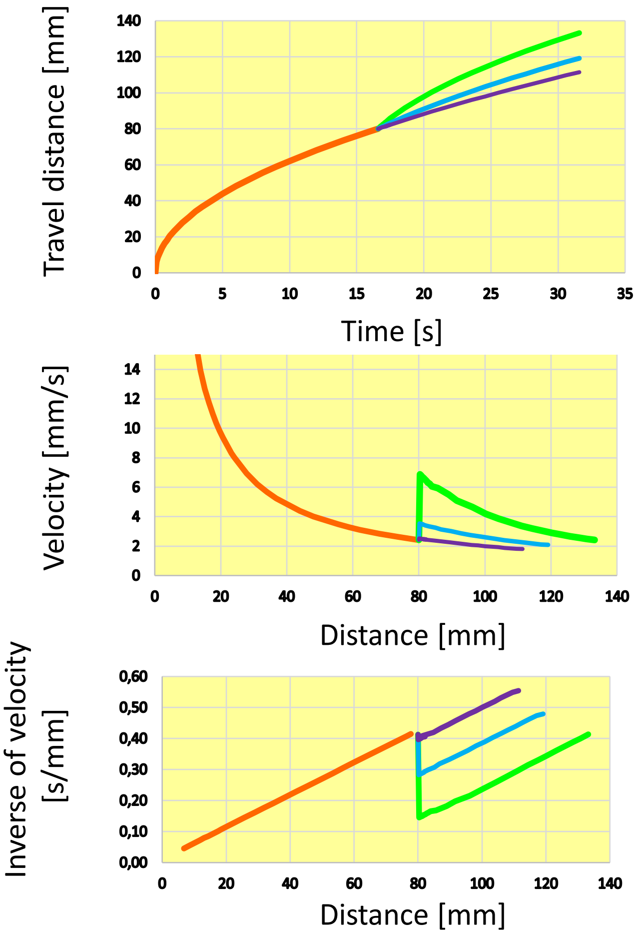

Figure C3. Top, travel distance vs time; middle, velocity vs distance in channel; bottom, inverse of velocity vs distance in channel. The orange line corresponds to the inlet channel, the green line to the side channel #1, the blue line to side channel #2, the purple line to side channel #3.

Section C3. Side channels located opposite and facing each other

In this section, we write the model for the dynamics (travel distance vs. time) of the flow in the case of oppositely facing side channels (Figure C4).

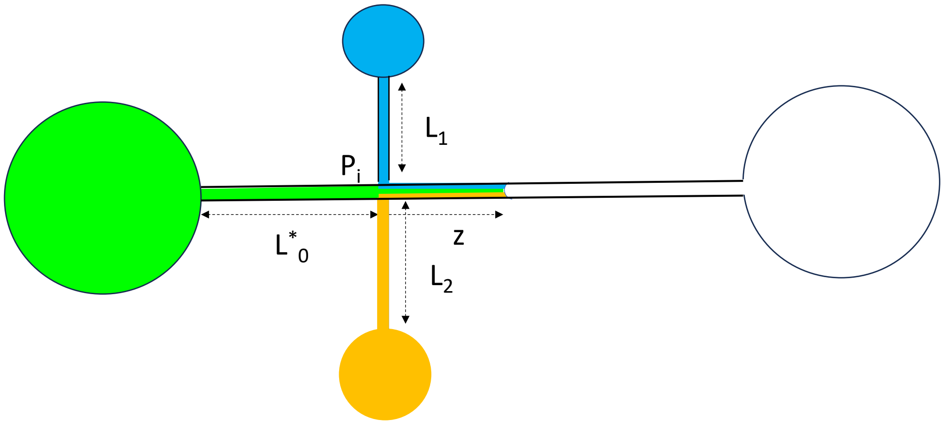

Figure C4. Sketch of the trigger-valve channel with opposite TGVs.

1. Model

The pressure at the intersection of the three channels is denoted *P_i*, which is the pressure of the node at the intersection of the three channels. Let us first write the pressure drop in the three channels ending at the intersection

$$P_i = \frac{p_0 L_0^*}{S_0}\,\mu\frac{V_0}{\lambda_0}\ , \tag{SI.3.1}$$

for the main channel (index *0*), and

$$P_i = \frac{p_1\, L_1}{S_1}\,\mu\frac{V_1}{\lambda_1}\ , \tag{SI.3.2}$$

for the first side channel (index *1*), and

$$P_i = \frac{p_2\, L_2}{S_2}\,\mu\frac{V_2}{\lambda_2}\ , \tag{SI.3.3}$$

for the second side channel (index 2). The mass conservation equation yields

$$S_0 V = S_0 V_0 + S_1 V_1 + S_2 V_2\ \ . \tag{SI.3.4}$$

In the viscous regime, the balance between capillary force and wall friction is [6,17]

$$\frac{p_0\, \gamma\, cos\theta_0^*}{S_0} = \frac{p_0\, z}{S_0}\ \mu \frac{V}{\overline{\lambda}_0} + P_i \quad , \tag{SI.3.5}$$

where $cos\theta_0^*$ is the cosine of the generalized Cassie angle. Finally, we consider the additional relation

$$V = \frac{dz}{dt}. \tag{SI.3.6}$$

Hence, we have 6 equations (SI.3.1 to SI.3.6) for the 6 unknowns $\{V, V_0, V_1, V_{2,} z, P_i\}$. Multiplying (SI.3.1) by S_0, (SI.3.2) by S_1, (SI.3.3) by S_2, and substituting the result in (SI.3.4) yields

$$S_0 V = \frac{P_i}{\mu}\left(\frac{\overline{\lambda}_0 S_0}{p_0\, L_0} + \frac{\overline{\lambda}_1 S_1}{p_1\, L_1} + \frac{\overline{\lambda}_2 S_2}{p_2\, L_2}\right) = \frac{P_i}{\mu}(A_0 + A_1 + A_2). \tag{SI.3.7}$$

Substituting (SI.3.6) and (SI.3.7) in SI.3.5) yields

$$\frac{p_0\, \gamma\, cos\theta_0^*}{S_0} = \frac{p_0}{2S_0}\ \mu \frac{1}{\overline{\lambda}_0} \frac{dz^2}{dt} + \mu \frac{S_0}{(A_0 + A_1 + A_2)} \frac{dz}{dt} \quad . \tag{SI.3.8}$$

Time integration of (SI.3.8) leads to a quadratic expression for *z*

$$z^2 + \left(\frac{2\overline{\lambda}_0 S_0^2}{p_0\, \sum_{i=0,2} A_i}\right) z - \frac{\gamma\, 2\overline{\lambda}_0\, cos\theta_0^*}{\mu} \tau = 0, \tag{SI.3.9}$$

where *t* is the time counted from the passage of the meniscus at the intersection. The expression for the travel distance *z* vs. time *t* is then

$$z = -\left(\frac{\overline{\lambda}_0 S_0^2}{p_0\, \sum_{i=0,2} A_i}\right) + \sqrt{\left(\frac{\overline{\lambda}_0 S_0^2}{p_0\, \sum_{i=0,2} A_i}\right)^2 + \frac{\gamma\, 2\overline{\lambda}_0\, cos\theta_0^*}{\mu} \tau}\ . \tag{SI.3.10}$$

In consequence, the velocity of the meniscus is

$$V = \frac{\frac{\gamma\,\bar{\lambda}_0\,cos\theta_0^*}{\mu}}{\sqrt{\left(\frac{\bar{\lambda}_0 S_0^2}{p_0\,\sum_{i=0,2} A_i}\right)^2 + \frac{\gamma\,2\bar{\lambda}_0\,cos\theta_0^*}{\mu}\tau}} = \frac{\frac{\gamma\,\bar{\lambda}_0\,cos\theta_0^*}{\mu}}{z+\left(\frac{\bar{\lambda}_0 S_0^2}{p_0\,\sum_{i=0,2} A_i}\right)}. \qquad \text{(SI.3.11)}$$

Remark that, if we note *z₀* the travel distance in the main channel without side channels ($z_0 = \sqrt{\frac{\gamma\,2\bar{\lambda}_0\,cos\theta_0^*}{\mu}\tau}$), and $\tilde{V}_0 = \frac{dz_0}{dt} = \frac{\gamma\,\bar{\lambda}_0\,cos\theta_0^*}{\mu}\frac{1}{z_0}$) we can rewrite (SI.3.11) as

$$\frac{V}{\tilde{V}_0} = \frac{z_0}{z+\left(\frac{\bar{\lambda}_0 S_0^2}{p_0\,\sum_{i=0,2} A_i}\right)}. \qquad \text{(SI.3.12)}$$

2. *Example*

Let us consider the same liquid (nonanol) and the dimensions listed in Table C3.

Table C3. Channel dimensions.

Inlet channel (index 0)	Side channel #1	Side channel #2
L_0= 80 mm	L_1 = 2 mm	L_1 = 2 mm
w_0 = 1mm	w_1 = 0.4 mm	w_1 = 0.4 mm
h_0=1mm	h_1 = 0.6 mm	h_1 = 0.6 mm

The results obtained using the model (relations SI.3.10 and SI.3.11) are shown in Figure C5.

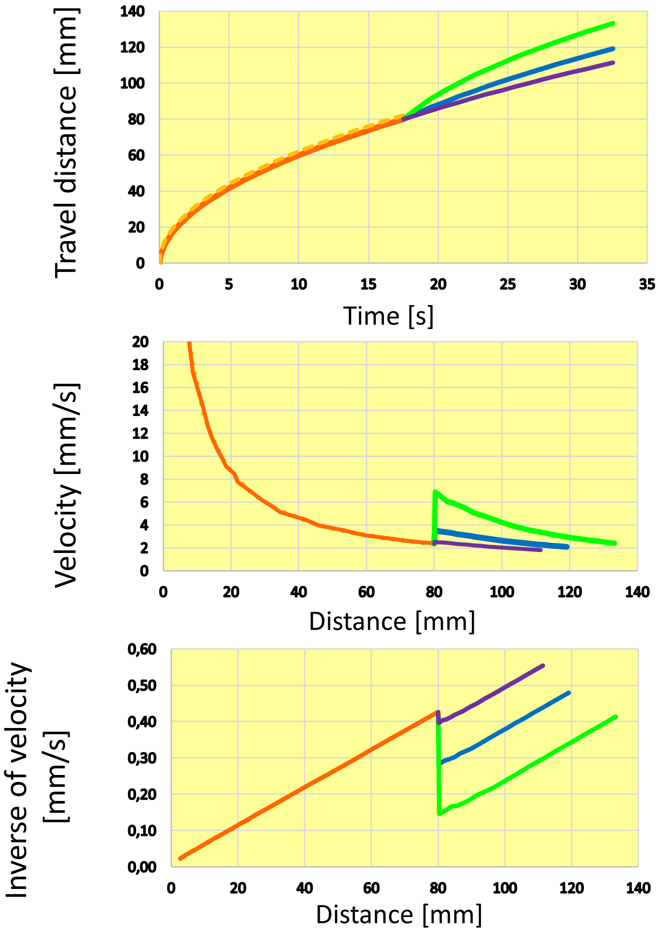

Figure C5. Top, travel distance vs time; middle, velocity vs distance in channel; bottom, inverse of velocity vs distance in channel. The orange line corresponds to the inlet channel, the green line to side channels of length 2 mm, the blue line to side channel of length 8 mm, and the purple line to side channels of length 80 mm.

Section C4. Engineering drawings of trigger valve devices

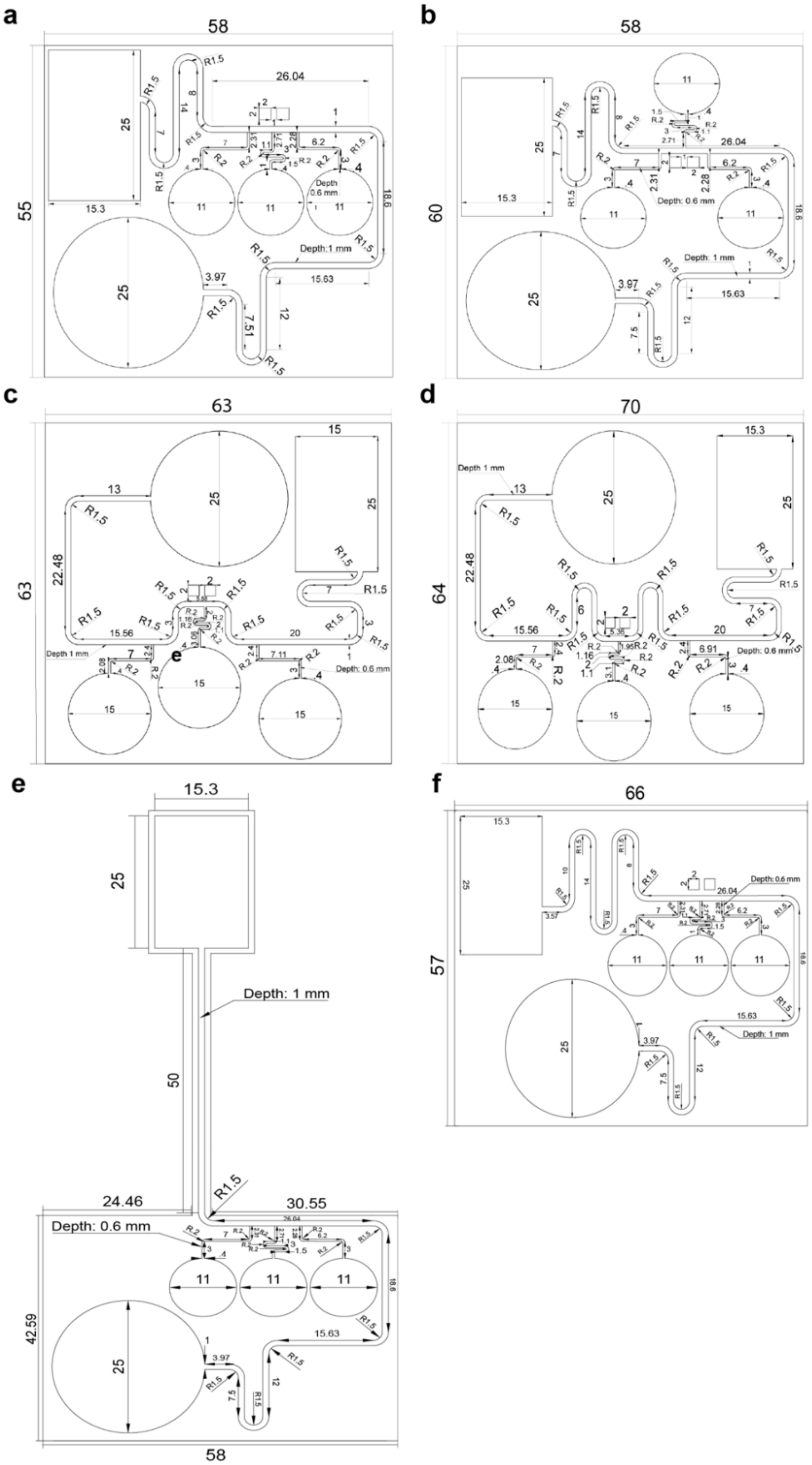

Figure C6. Engineering drawings of devices with channels on the same (a) and opposite sides (b) of the main channel, devices with 15 mm (c) and 30 mm (d) between trigger valves, side-view imaging device (f), and device with extended length between last trigger valve and paper pad (f). Units in mm.

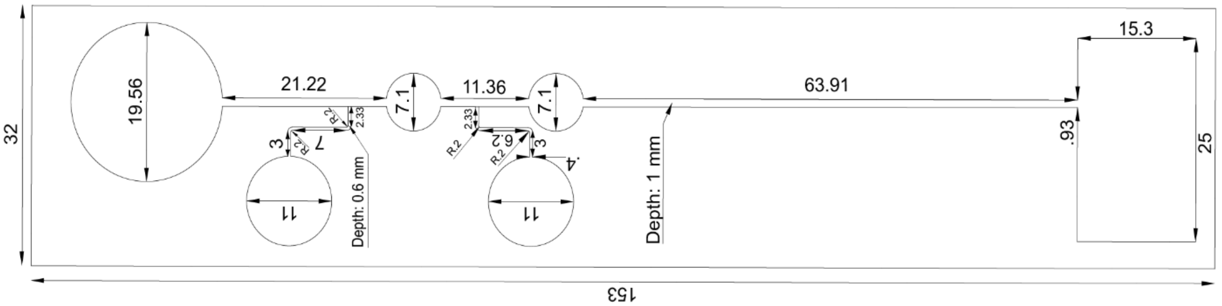

Figure C7. Engineering drawing of nitrite testing device. Units in mm.

Section C5. Additional experimental data

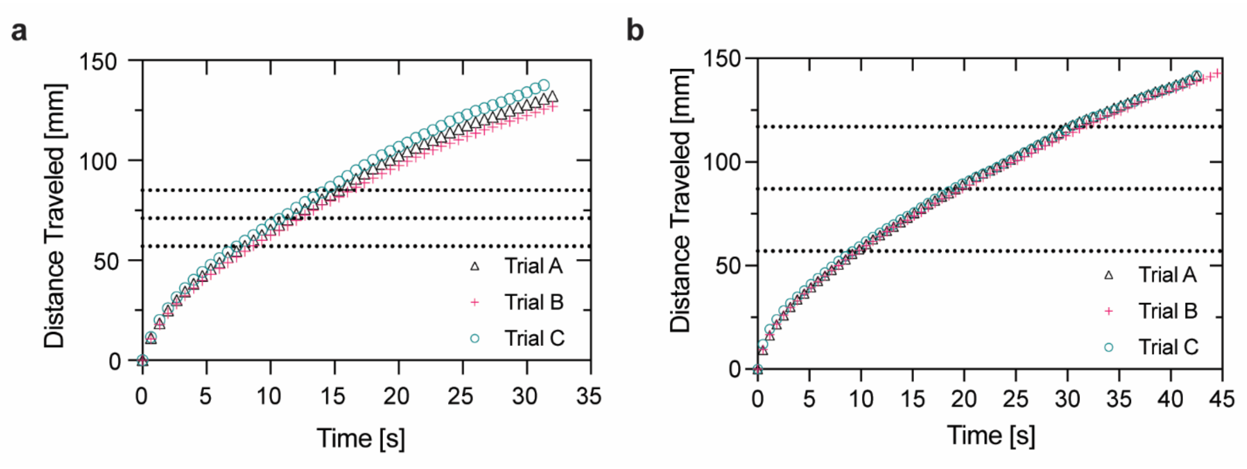

Figure C8. Travel distance data for all trials for programmed TGV release with valves separated by approximately 15 mm (a) and 30 mm (b). Every third data point is plotted for three trials (n=3).

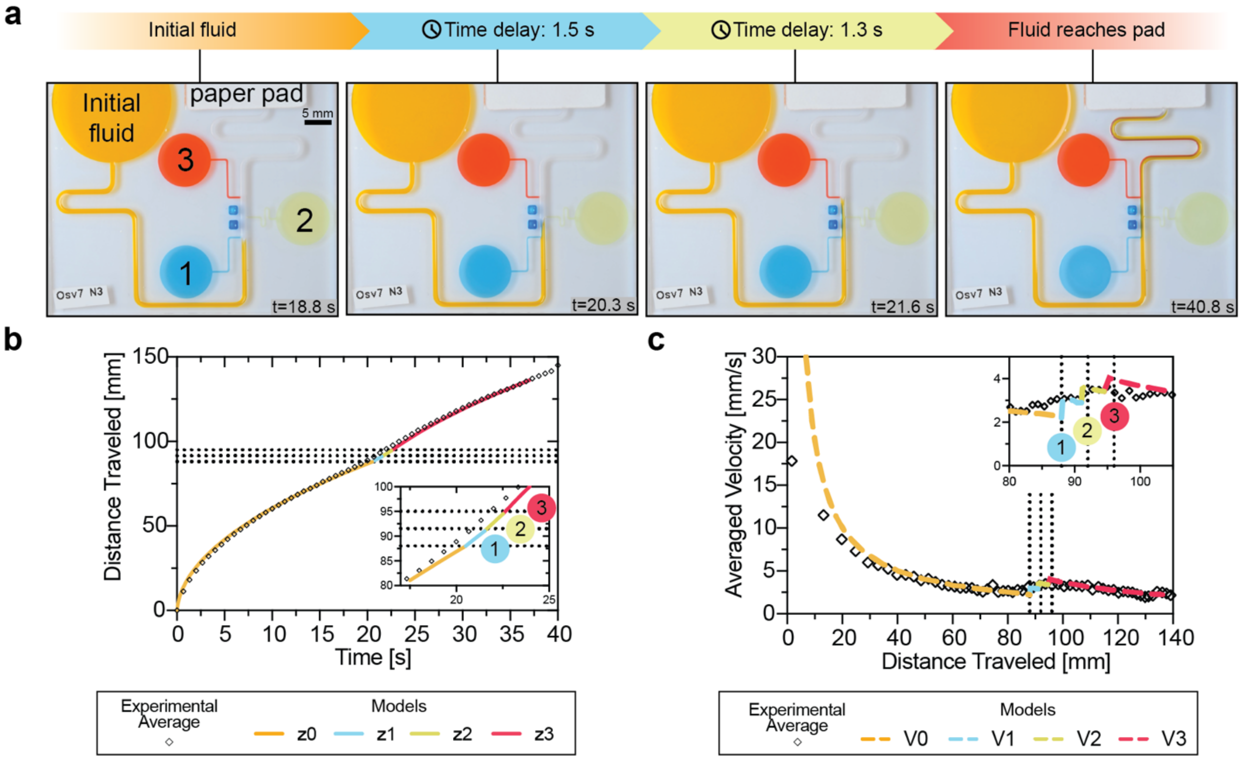

Figure C9. *Open trigger valves can be placed on opposite sides of main channel and maintain stair-like velocity trend.* Progression of fluid flow through device with shorter distances between oppositely-facing trigger valves (a). Comparison of the theoretical model (solid line) with experimental fluid front travel distance at the meniscus (black dots) for devices with three side channels on both sides of the main channel. Experimental data was averaged for three trials (n=3). Model is presented in segments corresponding to the calculated travel distances prior to the trigger valve release (orange, z0), between the first and second trigger valve (blue, z1), between the second the third valves (yellow, z2) and between the third valve and the paper pad (red, z3). Fluid velocities were calculated from the travel distance and the experimental data (diamonds) was compared against the calculated model (dashed line) velocities using a dynamic contact angle model (orange, V0) for the inlet. Model is shown at the first (blue, V1), second (yellow, V2), and third (red, V3) valves due to the increase in velocity upon trigger valve release.

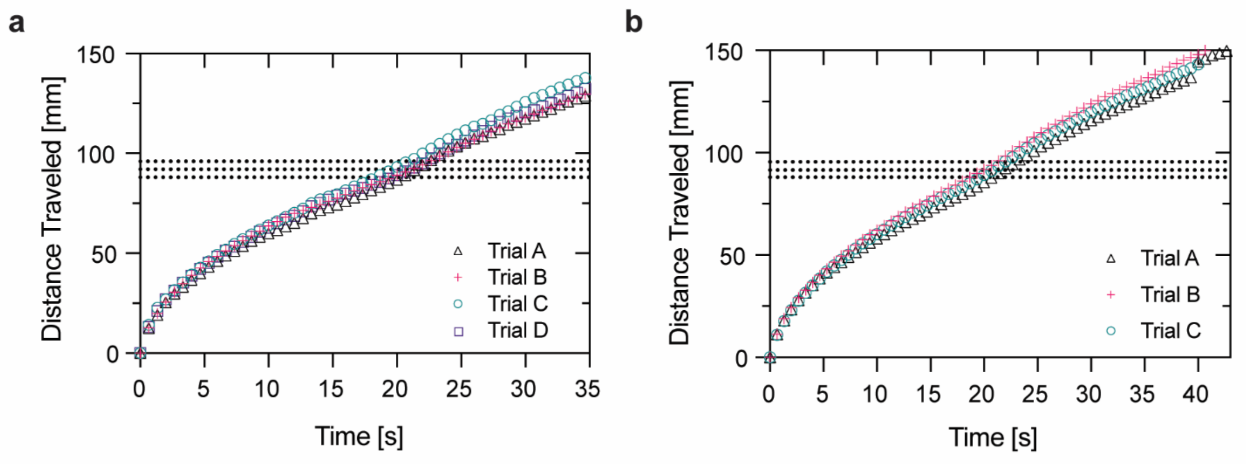

Figure C10. Travel distance data for all trials for TGV with shortened distances between valves on the same (a) and opposite sides (b) of the main channel. Every third data point is plotted for four (n=4) and three (n=3) trials for the TGVs on the same and opposite sides of the main channel, respectively.

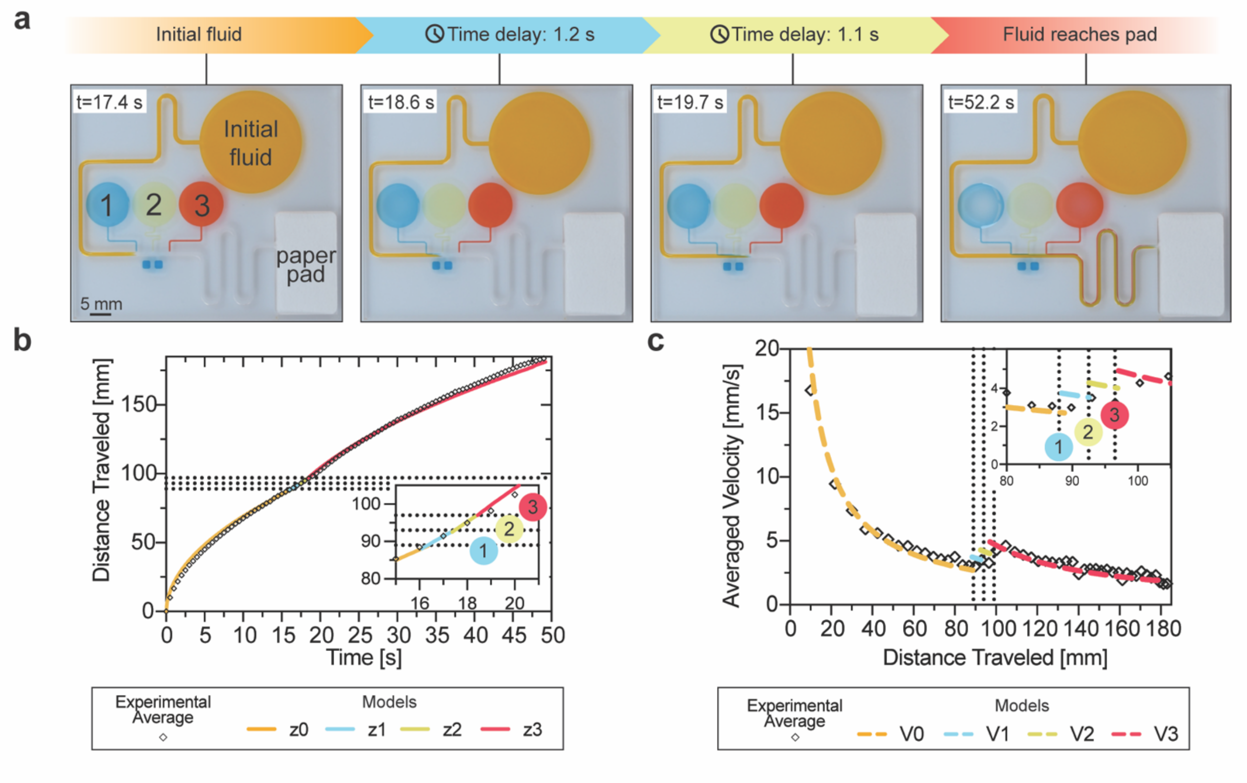

Figure C11. *Model predicts fluid velocity at approximately 80 mm after the last trigger valve.* Progression of fluid flow through device with a longer distance after the third trigger valve (a). Comparison of the theoretical model (solid line) with experimental fluid front travel distance at the meniscus (black dots) for devices with three side channels on the same side of the main channel with an extended channel length after the third valve. Experimental data was averaged for three trials (n=3). Model is presented in segments corresponding to the calculated travel distances prior to the trigger valve release (orange, z0), between the first and second trigger valve (blue, z1), between the second the third valves (yellow, z2) and between the third valve and the paper pad (red, z3). Fluid velocities were calculated from the travel distance and the experimental data (diamonds) was compared against the calculated model (dashed line) velocities using a dynamic contact angle model (orange, V0) for the inlet. Model is shown at the first (blue, V1), second (yellow, V2), and third (red, V3) valves due to the increase in velocity upon trigger valve release. Raw data can be found in Figure SI.5.5.

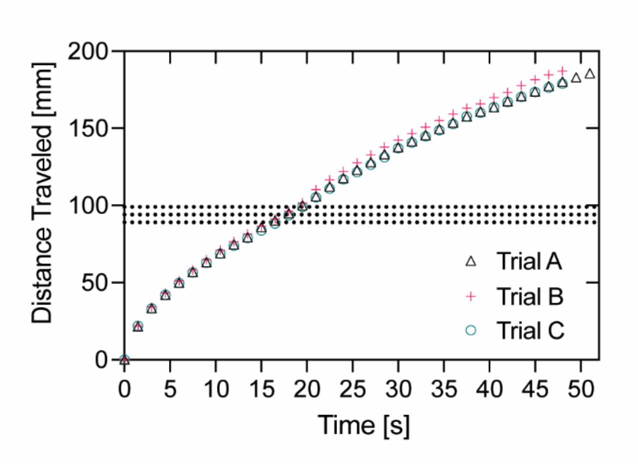

Figure C12. Travel distance data for TGV device with extended distance between last TGV and paper pad. Every third data point is plotted for three (n=3) trials.

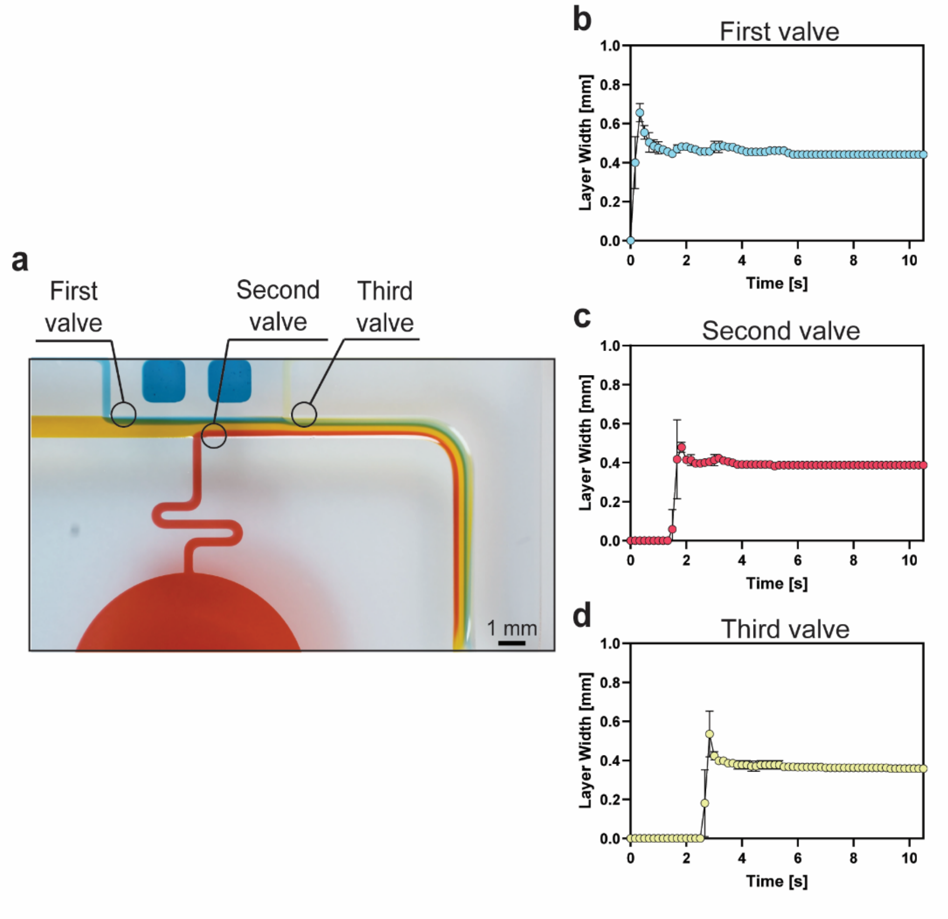

Figure C13. *Layers of trigger valves in oppositely facing configuration stabilize over time.* Image of the fluid layers in oppositely facing configuration (a). Circles indicate region where layer thickness measurements were taken for each layer. Plots of the measured layer widths over time for the parallel channel configuration after the first (c), second (d), and third (e) valves. Data is shown as an average of three replicates (n = 3) with error bars indicating standard deviation.

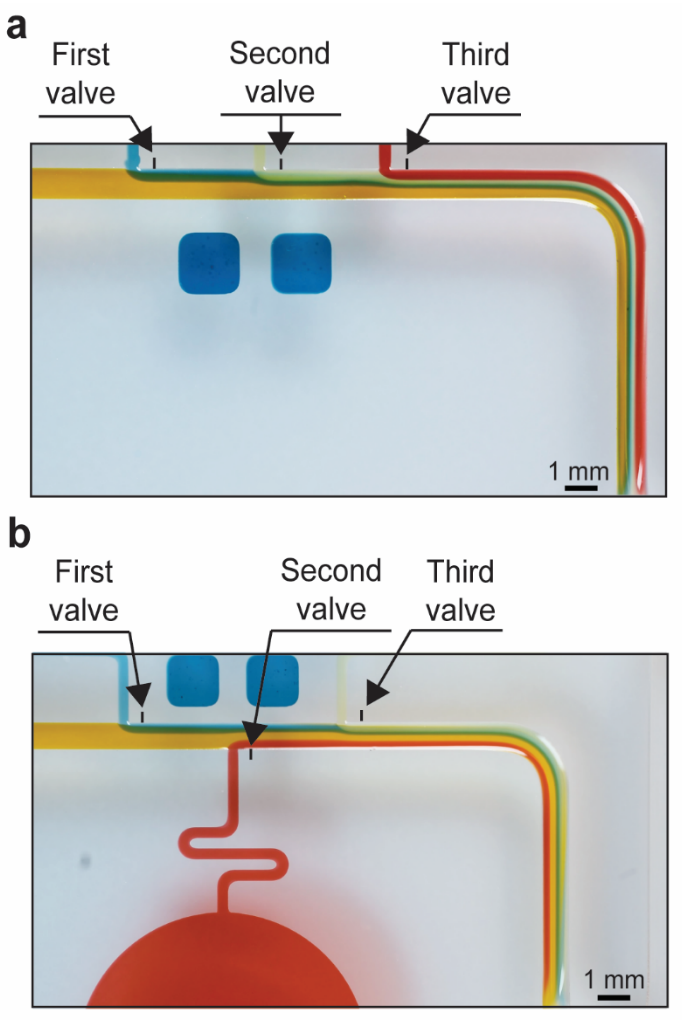

Figure C14. *Geographical location of layer width measurements for each TGV on the same and opposing sides of the main channel.* Layer width measurements were taken 0.5 mm from each TGV channel wall (black lines) for each of the corresponding TGV's colored fluid layer.

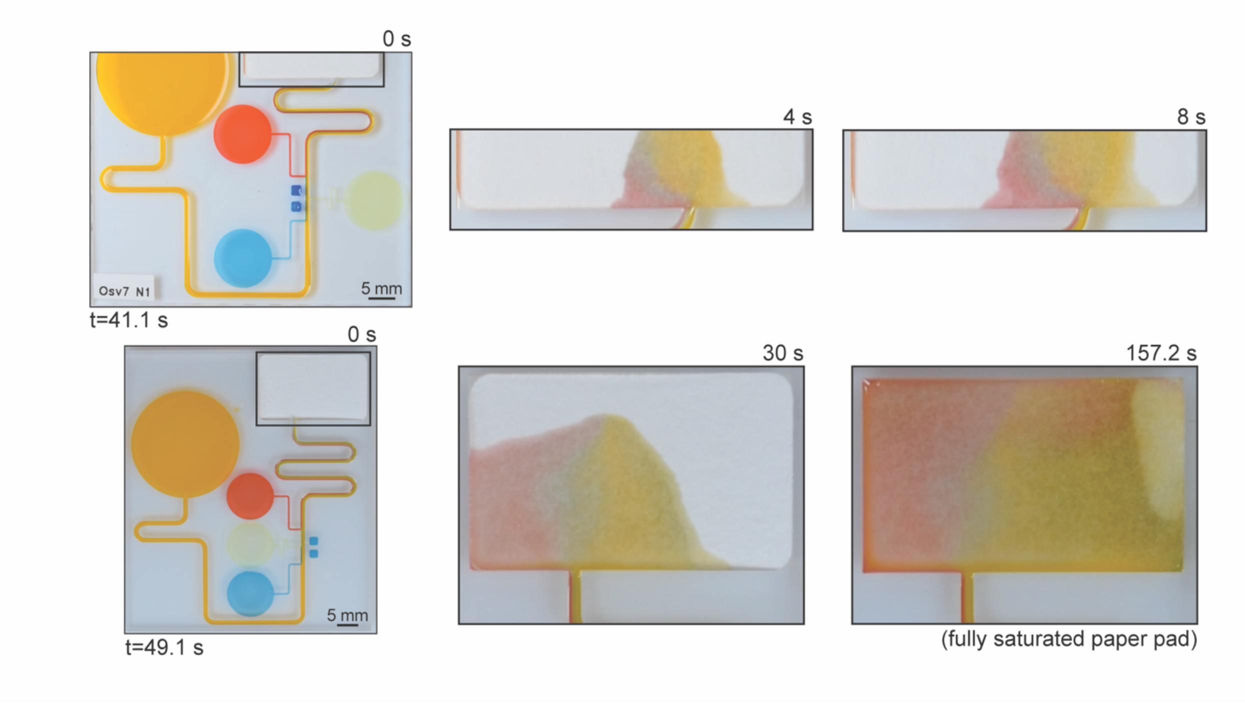

Figure C15. Fluid layers remain partially unmixed after reaching the paper pads. Images of the flow profiles of the paper pads for devices used in Figure SI.5.2 (top) and Figure SI.5.4 (bottom).

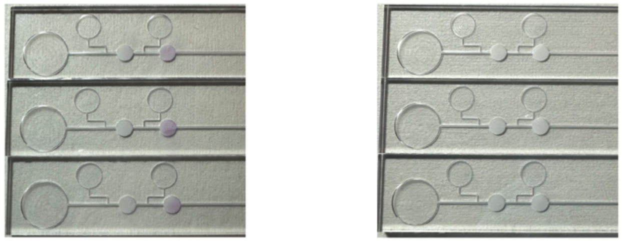

a 5 mg/L nitrite ion standard (positive control)

b deionized/distilled water (negative control)

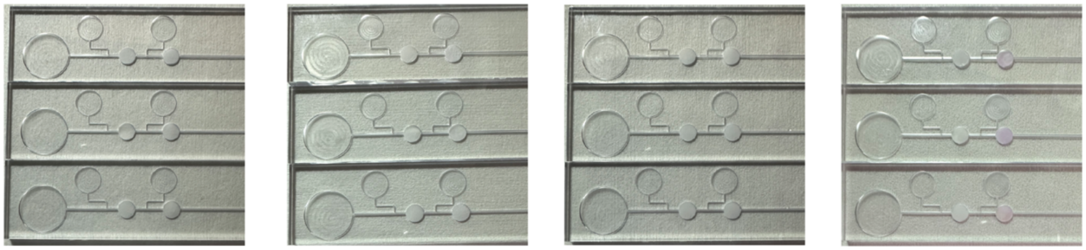

c Rain runoff sample

d Lake union water sample

e Tap water sample

f Bacon sample

Figure C16. Images of all Griess reaction trials for a 5 mg/L nitrate ion standard (a), deionized/distilled water (b), Lake Union sample (c), rain runoff (d), tap water (e), and a bacon sample (f).

Table C4. Detected nitrite concentrations in environmental and meat samples.

Sample	Mean concentration (± standard deviation) (mg/L)
Seattle tap water	ND*
Lake Union	0.1535 (0.3)
Rain runoff	ND*
Bacon meat	10.7272 (± 0.5)**

*Reported as not detected (ND) as the value is below the lowest detectable standard solution.
**Value was obtained by multiplying the diluted bacon sample by 4 (bacon meat sample was diluted at a ratio of 1:4) and is reflected in the table.

References

1. Berthier, J.; Gosselin, D.; Berthier, E. A generalization of the Lucas–Washburn–Rideal law to composite microchannels of arbitrary cross section. *Microfluid. Nanofluid.* **2015**, *19*, 497-507.
2. Tokihiro, J.C.; McManamen, A.M.; Phan, D.N.; Thongpang, S.; Blake, T.D.; Theberge, A.B.; Berthier, J. On the Dynamic Contact Angle of Capillary-Driven Microflows in Open Channels. *Langmuir,* **2024**, *40*(13), 7215–7224.
3. Bico, J.; Marzolin, C.; Quéré, D. Pearl drops. *Europhys. Lett.* **1999**, *47*(2), 220-226.
4. Berthier, J.; Brakke, K. A. *The Physics of Microdroplets*; Scrivener-Wiley Publishing, 2014.
5. Quéré, D. Inertial Capillarity. *Europhys. Lett.* **1997**, *39*(5), 533−538.
6. Berthier, J.; Theberge, A. B.; Berthier, E. *Open-Channel Microfluidics*, *Second Edition*; IOP Publishing, 2024.
7. Lucas, R. Ueber Das Zeitgesetz Des Kapillaren Aufstiegs von Flüssigkeiten. *Colloid Polym. Sci.* **1918**, *23* (1), 15–22.
8. Washburn, E. W. The Dynamics of Capillary Flow. *Phys. Rev.* **1921**, *17* (3), 273.
9. Rideal, E. K. On the Flow of Liquids under Capillary Pressure. *Philos. Mag. Ser. 6* **1922**, *44* (264), 1152–1159.
10. Bosanquet, C.H. On the flow of liquids into capillary tubes. *Philos. Mag. Ser*. **1923**, *6*(45), 525−531.
11. Yang, D.; Krasowska, M.; Priest, C.; Popescu, M.N.; Ralston, J. Dynamics of Capillary-Driven Flow in Open Microchannels *J. Phys.Chem*. C. **2011**, *115*, 18761−18769.
12. Ouali, F. F.; McHale, G.; Javed, H.; Trabi, C.; Shirtcliffe, N. J.; Newton, M. I. Wetting Considerations in Capillary Rise and Imbibition in Closed Square Tubes and Open Rectangular Cross-Section Channels. *Microfluid. Nanofluid.* **2013**, *15* (3), 309–326.
13. Kolliopoulos, P.; Jochem, K. S.; Johnson, D.; Suszynski, W. J.; Francis, L. F.; Kumar, S. Capillary-Flow Dynamics in Open Rectangular Microchannels. *J Fluid Mech.* **2021**, *911*, A32.
14. Berthier, J.; Brakke, K. A.; Berthier, E. A General Condition for Spontaneous Capillary Flow in Uniform Cross-Section Microchannels. *Microfluid. Nanofluid.* **2014**, *16* (4), 779–785.
15. Blake, T. D.; Haynes, J. M. Kinetics of Liquid-Liquid Displacement. *J. Colloid Interface Sci.* **1969**, *30* (3), 421–423.
16. Blake, T. D. The Physics of Moving Wetting Lines. *J. Colloid Interface Sci.* **2006**, *299* (1), 1–13.
17. Tokihiro, J.C.; Tu, W-c.; Berthier, J.; Lee, J.J.; Dostie, A.M.; Khor, J.W.; Eakman, M.; Theberge, A.B.; Berthier, E. Enhanced capillary pumping using open-channel capillary trees with integrated paper pads *Phys. Fluid.* **2023**, *35*(8), 082120-082120.

D. Appendix for Chapter 5

Reproduced in part from Nicholson, T.M.;,# **Tokihiro, J.C.;*** *Tu, W.C.; Khor, J.W.; Lee, U.N.; Berthier, E.; Amory, J.K.; Walsh, T.J.; Muller, C.H.; Theberge, A.B.*# *Open-channel droplet microfluidic platform for passive generation of human sperm microdroplets. ACS Biomaterials Science and Engineering,* ***2025****, 11(3), 1373–1378.*

**Equal Contribution*

#*Co-corresponding authors*

Section D1. Experimental

a. Device design and fabrication

The open-platform generator used in this study was developed from Khor *et al.* [ref]. The device with a 0.2 mm wide constriction region was chosen as the target device since the expected droplet volumes were less than or equal to 1 microliter.

Edits to the open droplet generator and the design of the droplet holder were done in a computer-aided design program (SolidWorks 2023, Waltham, MA). The device design was converted to a computer-aided machining (CAM) “G” code file (.simpl) and post-processed using Autodesk Fusion360 (San Francisco, California). The device and droplet holders were micromilled using a Datron Neo computer-numerical control (CNC) mill. The open droplet generators were milled from 3/16” PTFE sheets (#9266K15, McMaster-Carr, Elmhurst, Illinois). The droplet holders were milled from 4 mm thick polystyrene sheets (#ST31-SH-000200, Goodfellow, Pittsburgh, PA).

Prior to use, the milled devices and droplet holders were cleaned of debris using a soft brush. The parts were then cleaned of any residues by ultrasonication in 70% (v/v) aqueous ethanol for 30 minutes and then sprayed with fresh 70% (v/v) aqueous ethanol. Following the ethanol cleaning steps, the parts were rinsed with deionized (DI) water. Parts were then left to dry in a bioassay dish in the fume hood overnight. Prior to device operation, devices and droplet holders were cleaned of any lint and debris by spraying compressed air for thirty seconds. Devices were then set at a 3-degree incline inside of a bioassay dish using a plastic wedge.

To sterilize the carrier fluid, the solution was syringe filtered using a 0.22 um cellulose acetate syringe filter tip (Whatman, Cytiva, Marlborough, Massachusetts) and a plastic luer-lock syringe (#302995, Becton, Dickson and Company, Franklin Lakes, New Jersey).

b. Experimental Observation and analysis of droplet size

Videos of droplet generation were recorded using a Nikon D5300 digital single-lens reflex (DSLR) camera positioned to obtain a top-down view of the device. Videos were recorded at 60 frames per second (FPS).

c. Sperm sample preparation and sperm microdroplet generation

Under an approved Institutional Review Board protocol, healthy subjects provided informed consent and semen samples. After 2-5 days of abstinence, samples were obtained by masturbation into a sterile, labeled polypropylene specimen container. All semen samples were incubated at 37°C for 30 minutes prior to analysis. A portion of the semen sample was analyzed for standard semen quality parameters (including concentration and motility) according to World Health Organization protocols (cite WHO Manual of Sperm). All sperm motility assessments were performed using the Hamilton Thorne Research (Beverly, MA) Integrated Visual Optical System (IVOS). A direct swim out procedure was performed by layering 0.5 mL of neat semen underneath 3 mL of Human Tubal Fluid with Human Serum Albumin media (HTF-HSA), and incubation of this preparation for at least 60 minutes at a 30-degree angle at 37°C. The medium containing motile sperm was carefully aspirated and centrifuged at 250 RCF for 7 minutes twice in 3 mL sperm wash media. The final pellet was resuspended in 1-2 mL sperm wash medium and sperm motility was assessed with the IVOS. Experiments with sperm were conducted in the biosafety hood with microchannel placed inside of bioassay dish which was closed when not in use to minimize evaporation. A 1:500 dilution of red food coloring (McCormick) and purified sperm was created and 180 µL of purified motile sperm preparation with 1:500 red food coloring was pipetted into the inlet chamber of the microfluidic channel. 1-2 mL of carrier fluid was pipetted into the inlet and droplet formation was observed. After passage through the microchannel, sperm microdroplets were aspirated and combined into a 7 µL volume for motility analysis with the IVOS. IVOS was also used to assess motility of prepared sperm that were not exposed to red food coloring or the microchannel and red food coloring exposed sperm that were not exposed to the microchannel.

Section D2. Sperm in microdroplet under microscope

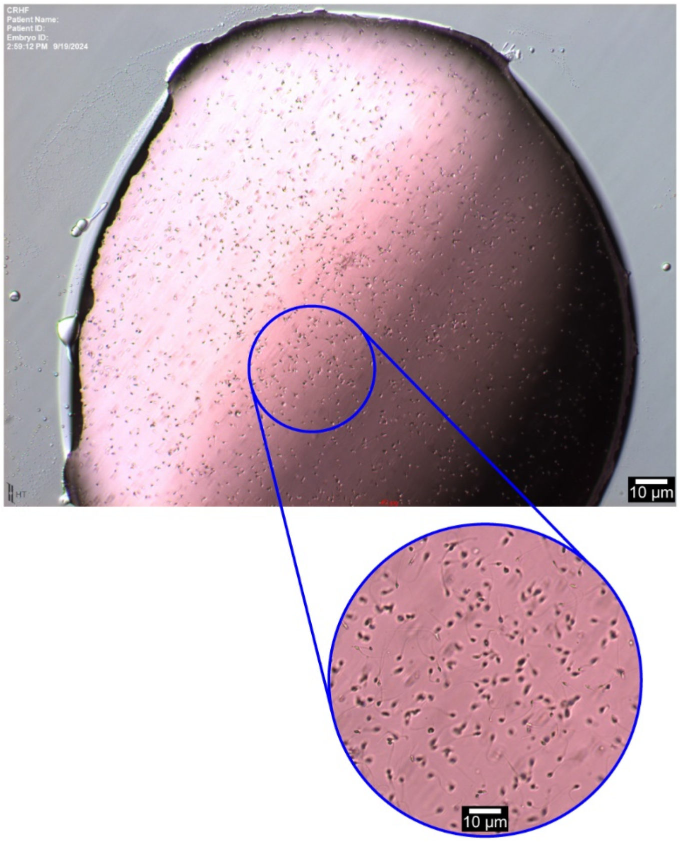

Figure D1. Image of microdroplet containing sperm after droplet generation in the open-channel device taken with a Olympus IX71 inverted phase-contrast microscope (Tokyo, Japan). Microdroplet is dyed red at the same 1:500 concentration (red FC to sperm media) used in the manuscript for visualization and contains approximately 6000 sperm per droplet based on purified sperm sample and median droplet size.

Section D3. Image for droplet volume calculation

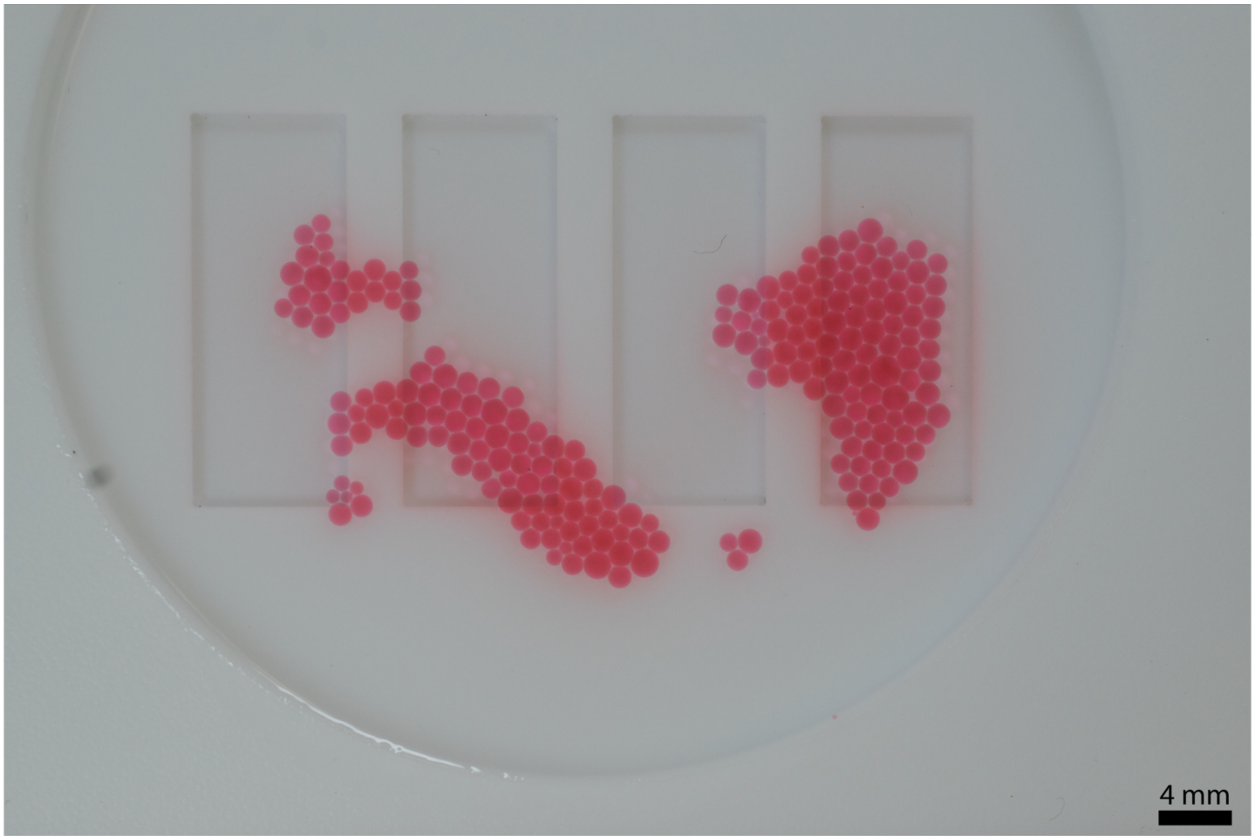

Figure D2. *Droplet volume was calculated using the diameters of the droplets and the equation $V = (1/6)(\pi)(d^3)$.* Droplet diameter was measured using the line tool in ImageJ with three measurements taken per droplet and an average diameter was used for the volume measurement. Volume for each droplet was calculated and averaged to obtain an average volume (± standard deviation) of 0.874 µL (± 0.3 µL). All the droplets generated from one device were used to calculate the average volume.

Section D4. Droplet stability images

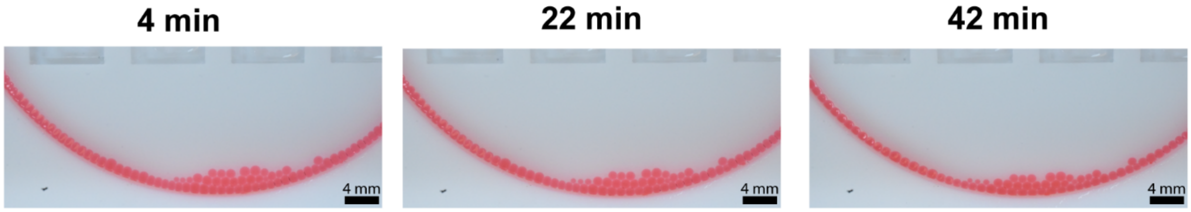

Figure D3. *Droplets are stable for 42 minutes after droplet generation.* Images of dyed sperm media droplets generated at 4 minutes (a), 22 minutes (b), and 42 minutes (c) after the generation of the last droplet. No merging or fusion of droplets was observed during the experiment.

Section D5. Participant 1 and 2 sperm kinematic data

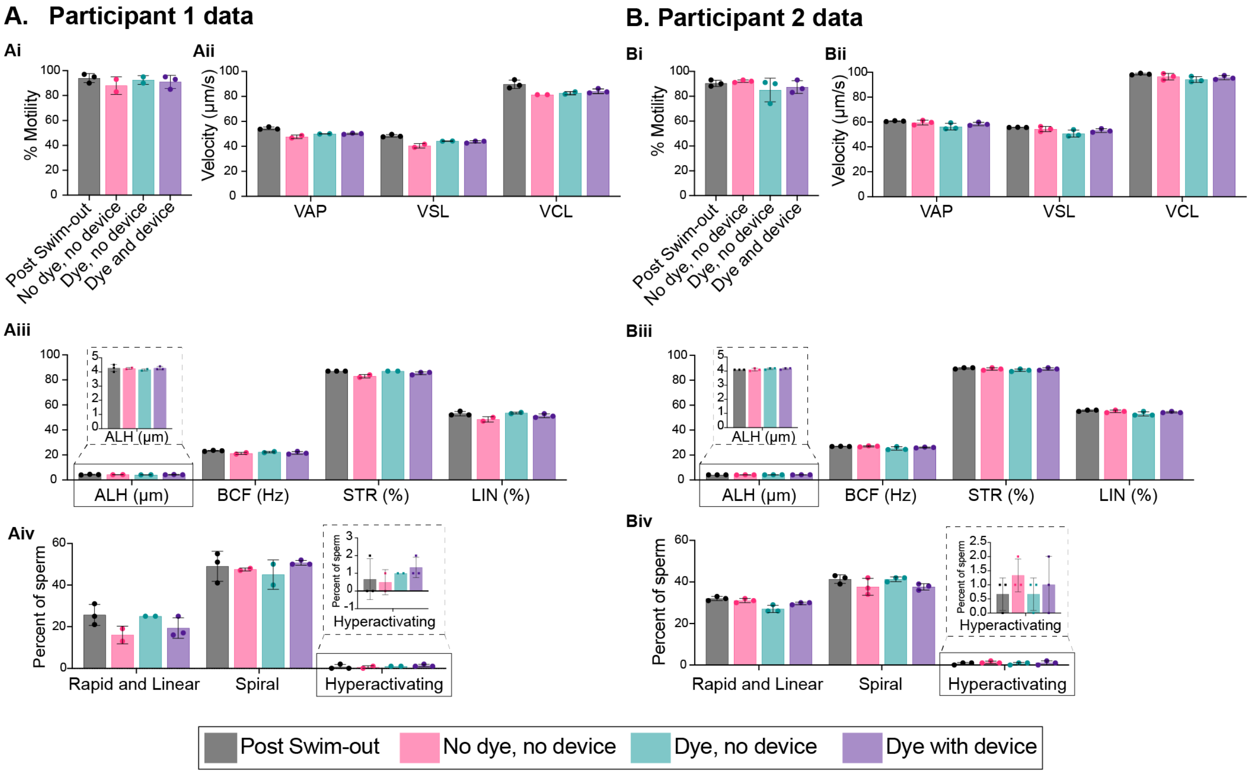

A. Participant 1 data

B. Participant 2 data

Figure D4. Extended sperm %motility, velocities, and kinematic data were collected with the IVOS. Amplitude lateral height (ALH), beat/cross frequency (BCF), straightness (STR) and linearity (LIN) measurements, and number of rapid and linear, spiral, and hyperactivating sperm were collected for participant 1 (A) and 2 (B). The X axis denotes the measurement with the respective Y-axis units shown in parentheses. Two individual experiments were conducted with the same devices, and the semen samples were from two different participants. Data form a third participant are shown in Figure 4. Each data point represents an individual device; the bar graph represents the mean ± SD of n = 2 or 3 devices.

VITA

Jodie C. Tokihiro was born and raised on the Big Island in Hilo, Hawaii. She received her Bachelor’s of Science in Chemistry with a focus in biosciences at the University of Hawaii at Hilo in 2020. At the University of Hawaii at Hilo, Jodie was an undergraduate researcher and subsequently a laboratory assistant in the laboratory of Dr. Matthew S. Platz where she did organic chemical synthesis and photochemistry. After discovering her love for research, Jodie became a doctoral student at the University of Washington in the Department of Chemistry in 2021 where she joined the Bioanalytical Chemistry for Medicine and the Environment (BCME) laboratory under the guidance of Professor Ashleigh B. Theberge. In the BCME lab, Jodie studied the fundamental properties and physics of open-channel microfluidics and its applications in urology and environmental research.